ESTIMATION OF HIGH-FREQUENCY ATTENUATION PARAMETER (KAPPA) FOR HARD ROCK STATIONS OF TURKISH STRONG MOTION NETWORK

A THESIS SUBMITTED TO
THE GRADUATE SCHOOL OF NATURAL AND APPLIED SCIENCES
OF
MIDDLE EAST TECHNICAL UNIVERSITY

BY

ATINÇ ÖZGÜN AKGÜN

IN PARTIAL FULFILLMENT OF THE REQUIREMENTS
FOR
THE DEGREE OF MASTER OF SCIENCE
IN
CIVIL ENGINEERING

FEBRUARY 2021

Approval of the thesis:

ESTIMATION OF HIGH-FREQUENCY ATTENUATION PARAMETER (KAPPA) FOR HARD ROCK STATIONS OF TURKISH STRONG MOTION NETWORK

submitted by **ATINÇ ÖZGÜN AKGÜN** in partial fulfillment of the requirements for the degree of **Master of Science** in **Civil Engineering, Middle East Technical University** by,

Prof. Dr. Halil Kalıpçılar
Dean, Graduate School of **Natural and Applied Sciences** ________________

Prof. Dr. Ahmet Türer
Head of the Department, **Civil Engineering** ________________

Prof. Dr. Zeynep Gülerce
Supervisor, **Civil Engineering, METU** ________________

Asst.Prof.Dr Atilla Arda Özacar
Co-Supervisor, **Geological Engineering, METU** ________________

Examining Committee Members:

Prof. Dr. Kemal Önder Çetin
Civil Engineering, METU ________________

Prof. Dr. Zeynep Gülerce
Civil Engineering, METU ________________

Prof. Dr. Ayşegül Askan Gündoğan
Civil Engineering, METU ________________

Asst. Prof. Dr. Atilla Arda Özacar
Geological Engineering, METU ________________

Assoc. Prof. Dr. Özkan Kale
Civil Engineering, TEDU ________________

Date: 12.02.2020

I hereby declare that all information in this document has been obtained and presented in accordance with academic rules and ethical conduct. I also declare that, as required by these rules and conduct, I have fully cited and referenced all material and results that are not original to this work.

Name Last name : Atınç Özgün Akgün

Signature :

ABSTRACT

ESTIMATION OF HIGH-FREQUENCY ATTENUATION PARAMETER (KAPPA) FOR HARD ROCK STATIONS OF TURKISH STRONG MOTION NETWORK

Akgün, Atınç Özgün
Master of Science, Civil Engineering
Supervisor : Prof. Dr. Zeynep Gülerce
Co-Supervisor: Asst. Prof. Dr. Atilla Arda Özacar

February 2021, 96 pages

Site-specific decay in the Fourier Amplitude Spectrum (FAS) at high frequencies, a.k.a. the zero-distance kappa (κ_0), is frequently used in seismic analysis of critical infrastructure; especially for the host-to-target adjustment of the design spectrum and the site response analysis. The zero-distance kappa value for hard rock sites is more crucial but harder to constrain because the amount of strong-motion stations on hard-rock sites is limited in the global datasets. The objective of this study is to calculate the zero-distance kappa value for the hard rock strong-motion stations operated by the Disaster and Emergency Presidency of Turkey (AFAD). For this purpose, 6463 recordings from 22 strong-motion stations with measured average shear wave velocities at the first 30 meters (V_{S30}) higher than 740m/s and having at least 100 records have been analyzed. The slope of the decay in the S-wave portion of the FAS (kappa) at high frequencies is determined for a carefully selected and record-specific frequency range. Variation of the kappa with epicentral distance is evaluated to determine the median zero-distance kappa and its uncertainty for each recording station. Estimated median zero-distance kappa values vary between 0.01s to 0.06s and are consistent with the limited amount of previously published data. Only a weak correlation in median zero-distance kappa is observed with increasing V_{S30}, and a rather large scatter in kappa for the same V_{S30} values is observed. More robust results

might be attained by isolating the site amplification effects of weak surficial layers and subcategorization based on available geological and geographical information.

Keywords: High-frequency attenuation, Hard rock sites, Strong ground motion, Zero distance kappa

ÖZ

YÜKSEK FREKANSLI YER HAREKETİ İÇİN SÖNÜMLENME PARAMETRESİNİN (KAPPA) TÜRK KUVVETLİ YER HAREKETİ AĞI SERT KAYA İSTASYONLARI İÇİN BELİRLENMESİ

Akgün, Atınç Özgün
Yüksek Lisans, İnşaat Mühendisliği
Tez Yöneticisi: Prof. Dr. Zeynep Gülerce
Ortak Tez Yöneticisi: Dr. Atilla Arda Özacar

Şubat 2021, 96 sayfa

Sahaya özel Fourier genlik spektrumunun (FAS'nun) yüksek frekans sönümlenme parametresi, diğer adıyla sıfır-mesafedeki kappa (κ_0), kritik yapıların sismik analizinde, özellikle tasarım spektrumunun kaynak-hedef düzeltmesinde ve zemin tepki analizlerinde sıklıkla kullanılmaktadır. Sert kaya sahalar için sıfır-mesafedeki kappa değerinin belirlenmesi daha kritiktir ancak küresel kuvvetli yer hareketi veri setlerindeki sert kaya istasyonların sayısı sınırlı olduğu için bu değerin tuttarlı bir biçimde belirlenmesi daha zordur. Bu çalışmanın amacı Türkiye Afet ve Acil Durum Yönetimi Başkanlığı (AFAD) tarafından işletilen kuvvetli yer hareketi ağına dahil sert kaya istasyonları için sıfır-mesafedeki kappa değerlerinin hesaplanmasıdır. Bu amaçla ilk 30 metredeki kayma dalgası hızı ortalaması (V_{S30}) değerleri 740m/s'den daha yüksek olup en az 100 kayıt bulunduran 22 istasyondan 6463 kayıtın yatay bileşenleri analiz edilmiştir. Kayıtların S-dalgası kısımlarından elde edilen FAS'nun yüksek frekanslardaki sönümlenmesinin eğimi, frekans aralıkları her kayda özel olacak şekilde ve dikkatle seçilerek belirlenmiştir. Her istasyon için, kappa parametresinin merkez üssü uzaklıkları ile dağılımı incelenerek ortalama sıfır-mesafedeki kappa değeri ve bu değerdeki belirsizlik hesaplanmıştır. 22 istasyon için hesaplanan sıfır-mesafedeki kappa değerleri 0.01s ve 0.06s arası değişmekte ve literatürdeki sert kaya istasyonları için belirlenmiş değerler ile uyum göstermektedir. Analizler sonucunda, yükselen V_{S30} ile medyan sıfır-mesafedeki kappa değerinde

zayıf bir trend ve aynı V_{S30} değerine sahip istasyonlardan hesaplanan kappa değerleri arasında yüksek bir saçılım olduğu gözlemlenmiştir. Anakaya üzerindeki zayıf ve yüzeysel zemin katmanların zemin büyütme etkilerinin elimine edilmesi ve hesaplanan sıfır-mesafedeki kappa değerlerinin jeolojik ve coğrafi altkategorilere ayrılması daha sağlıklı sonuçların elde edilmesinde yardımcı olabilir.

Anahtar Kelimeler: Yüksek frekans sönümlenme parametresi, Sert kaya istasyonları, Kuvvetli yer hareketleri, Sıfır-mesafe kappa

Dedicated to my beloved family…

ACKNOWLEDGEMENTS

First, I want to express my deepest gratitude to my supervisor Prof. Dr. Zeynep Gülerce, and co-supervisor Assoc. Prof. Dr. Atilla Arda Özacar for their guidance, advice, criticism, encouragement, and insight throughout the research.

I’m deeply grateful to Davor Stanko and Metin Kahraman for providing essential scripts and tools for this study.

I would like to thank my close friend Gökhan Uğur Atıl for his continuous support and motivation through the years.

I would like to thank my dear partner Merve Ayaz for her irreplaceable support and motivation when I need it the most.

Finally, I would like to thank my dear family. I am grateful for every sacrifice that they've made for me. This accomplishment would not have been possible without their invaluable support.

TABLE OF CONTENTS

LIST OF TABLES

TABLES

LIST OF FIGURES

FIGURES

LIST OF ABBREVIATIONS

ABBREVIATIONS

m – Meters

Km – Kilometers

s – Seconds

Hz – Hertz

FAS – Fourier Amplitude Spectrum

MASW – Multi-spectral Acceleration of Surface Waves

SNR – Signal to Noise Ratio

GMPE – Ground Motion Prediction Equation

PSHA – Probabilistic Seismic Hazard Assessment

ReMi – Refraction Microtremor Method

NEHRP – National Earthquake Hazards Reduction Program

LIST OF SYMBOLS

SYMBOLS

f_{max}, f_1 – Frequency before crashing syndrome

f_c – Corner frequency

f_{c10Bar} – Theoretical corner frequency calculated for 10 bar stress drop

$f_{c100Bar}$ – Theoretical corner frequency calculated for 100 bar stress drop

f_2 – Frequency where crashing syndrome ends

κ – High-frequency attenuation parameter, kappa

β – Crustal shear wave velocity

κ_0 – Kappa with eliminated distance effect

κ_{as} – Kappa calculated using Anderson and Hough (1984) method

κ_R – Slope of the linear function

R_{epi} – Epicentral Distance

$V_{s.}$ – Shear wave velocity

V_{s30} – Shear wave velocity for first 30 meters depth

M_L – Local magnitude

M_W – Moment magnitude

m_b – Short period body-wave magnitude

CHAPTER 1

INTRODUCTION

Kappa is one of the parameters that describe the attenuation of the shear wave amplitudes of ground motions at high frequencies. Its discovery dates back to 1982 when Hanks (1982) observed that after a specific frequency, which is later named as f_{max}, the acceleration spectrum decays rapidly and falls under the noise spectrum, disagreeing with the widely accepted omega-squared source model. Anderson and Hough (1984) articulated this decay with the parameter κ (kappa), which is defined as the slope of the attenuation of the high-frequency part of the acceleration Fourier amplitude spectrum (FAS) of a record.

Since its discovery, κ has played an important role in various engineering seismology applications such as the host-to-target adjustment of the ground-motion prediction equations (GMPEs) at high frequencies or used as a low-pass filter to constrain the high frequencies in the generation of synthetic ground motions in point-source or finite-fault stochastic or hybrid simulation approaches while eliminating the attenuation as a correction on anelastic attenuation (Ktenidou et al., 2014).

Site-specific high-frequency attenuation parameter for hard-rock sites has been calculated and included in estimating the ground motions for important projects such as nuclear power plants (e.g., PEGASOS Refinement and Sigma Projects) and other structures (e.g., concrete dams) that are sensitive to high-frequency ground motions (Muto and Duron, 2015). Biro and Renault (2012) noted that when the zero-distance kappa (also known as the intercept of kappa vs. epicentral distance plot for a site) is obtained for the target (hard-rock) sites and κ_0 is used in the host (soft rock)-to-target adjustment, it may lead up to a factor of three difference in the results of probabilistic seismic hazard assessment (PSHA) results. Owing to this large impact on the PSHA results, the latest studies have focused on estimating κ_0 for strong motion stations that are located on hard-rock sites. This is particularly challenging because even if the amount of available ground motion data on hard-rock sites has greatly expanded worldwide during the last years (https://www.sigma-2.net/pages/technical-programme/wp3-ground-motion/), the majority of the strong-motion stations in Europe and United States are located on soft/alluvial sites, and the site characterization studies for the limited number stations located at hard-rocks sites are missing.

1.1 Research Statement

Kappa has been calculated, examined, and used extensively in the Western United States (Campbell et al. 2014), Europe (e.g., Drouet et al. 2010 and Douglas et al. 2010 for France; Edwards et al. 2011 for Switzerland; Gentili and Franceschina 2011 in the southeastern Alps and northern Dinarides, Stanko et al. 2018 for Croatia), India (e.g., Kumar et al. 2018, Kumar et al. 2019 and Mittal et al. 2020), Japan (Tsurugi et al. 2020) and Taiwan (Lai et al. 2016 and Chang et al. 2019). Previous attempts to estimate the kappa based on strong motions recorded in Turkey were mostly limited to a single region and depended on a relatively small database. Even though Askan et al. (2014), Kurtulmuş et al. (2015), and Tanırcan et al. (2018) estimated the high-frequency attenuation parameter for different sites in Western Turkey, the focus of these attempts were not specifically the hard-rock stations and the datasets used for these studies were only limited to a mainshock and aftershocks of a critical event. Recently, Biro et al. (2020) provided initial estimates of κ_0 for a set of hard-rock stations operated by Disaster and Emergency Presidency of Turkey (AFAD) using a limited number of recordings, underlining the large scatter in these preliminary estimates. Nevertheless, an overarching and in-depth evaluation of the high-frequency attenuation characteristics of the hard-rock recording stations in Turkey is not available.

The main objective of this study to obtain the high-frequency attenuation parameters of hard-rock sites, using a database of strong ground motions from stations located at hard-rock sites with complete site characterization in Turkey. A well-defined and repeatable procedure for estimating the record-specific kappa values from the slope of the decay in the FAS of the S-wave window of the recordings for a carefully selected and record-specific frequency band is utilized. The zero-distance kappa values for 21 stations are estimated from the distribution of record-specific kappa values with epicentral distance, considering that the stations located in the same geographical locating will share similar path contributions on the FAS. Possible correlation between the record-specific kappa with magnitude and the relation between zero distance kappa and the stiffness of the site are evaluated. This comprehensive study attempts to fill the need for the hard-rock site kappa values for a future V_{S30} (Average shear wave velocity for first 30 meters depth)-Kappa relationship specifically for Turkey is a necessity to aid host-to-target adjustment of hard-rock conditions.

1.2 Organization of Thesis

Chapter 2 presents kappa's definition, historical development, methods to obtain this parameter, its field of application, and previous literature on kappa (worldwide and in Turkey) for hard-rock sites.

Following that, the database used for this study and the characteristics of the recording stations is discussed in detail in Chapter 3. Chapter 3 also describes the methodology and the steps used to estimate the record-specific kappa values.

The results obtained from this study (e.g., zero-distance kappa values) and their correlations with other variables (magnitude, site stiffness, anelastic attenuation, etc.) are evaluated and presented in Chapter 4.

Chapter 5 provides the final comments on the results together with suggestions for future studies and compares the findings with previous local and global attempts for estimating kappa for hard rock stations.

CHAPTER 2

BACKGROUND ON HIGH-FREQUENCY ATTENUATION

The Fourier Amplitude Spectrum (FAS) obtained from an accelerogram is one of the most common methods used by seismologists to describe the frequency content of ground motions. FAS is utilized in the assessment of the earthquake source characteristics, where the amplitudes and parameters obtained from FAS can be used to estimate the slip and size of the fault and stress drop on the fault surface (Trifunac, 1994). In the earthquake engineering practice, FAS is employed for several different purposes varying from the analysis of local site amplification to dynamic soil-structure interaction analysis. For calculating the FAS, the Finite Fourier transform (F(f)) of an accelerogram (a(t)) is obtained by:

$$F(f) = \int_0^T a(t)e^{-ift}dt \qquad (2.1)$$

where T is the duration of the accelerogram, and f is the frequency. Following Eq. 2.1, FAS is defined as the square root of the sum of the squares of all parts of F(f), so the Fourier transform, FS(f), is formulated as:

$$FS(f) = \sqrt{\{[\int_0^T a(t)sinftdt]^2 + [\int_0^T a(t)cosftdt]^2\}} \qquad (2.2)$$

The FS(f) from the accelerograms of the ground motion measured on the ground surface can be described as:

$$FS(f)= C \; x \; M_0 \; x \; S(f) \; x \; G(R_{epi}) \; x \; D(R_{epi},f) \; x \; Am(f) \; x \; P(f,f_{max}) \qquad (2.3)$$

where R_{epi} is the epicentral distance, S(f) is the source spectrum, $G(R_{epi})$ is the geometric attenuation of the seismic wave (a.k.a. geometrical spreading), $D(R_{epi},f)$ is the anelastic attenuation of seismic wave, Am(f) is the amplification factor due to the difference of properties between source and receiver site, $P(f,f_{max})$ is the high-cut filter or near-site attenuation, and f_{max} is the high cut-off frequency, respectively. The omega-squared stochastic model proposed by Brune (1970) is a generally accepted model for defining source effects (S(f)) given in Eq. 2.3. In the omega-squared model, the source effect is expressed by:

$$S(f) = \frac{(2\pi\ )^2}{1+(\frac{f}{f_c})^2} \tag{2.4}$$

where f_c is the corner frequency. As described in Equation 2.4 (Brune, 1970), the shape of the source spectrum is well defined for low frequencies with an increase till the corner frequency, and the model results in a flat line for frequencies higher than f_c, as shown in Figure 2.1(a).

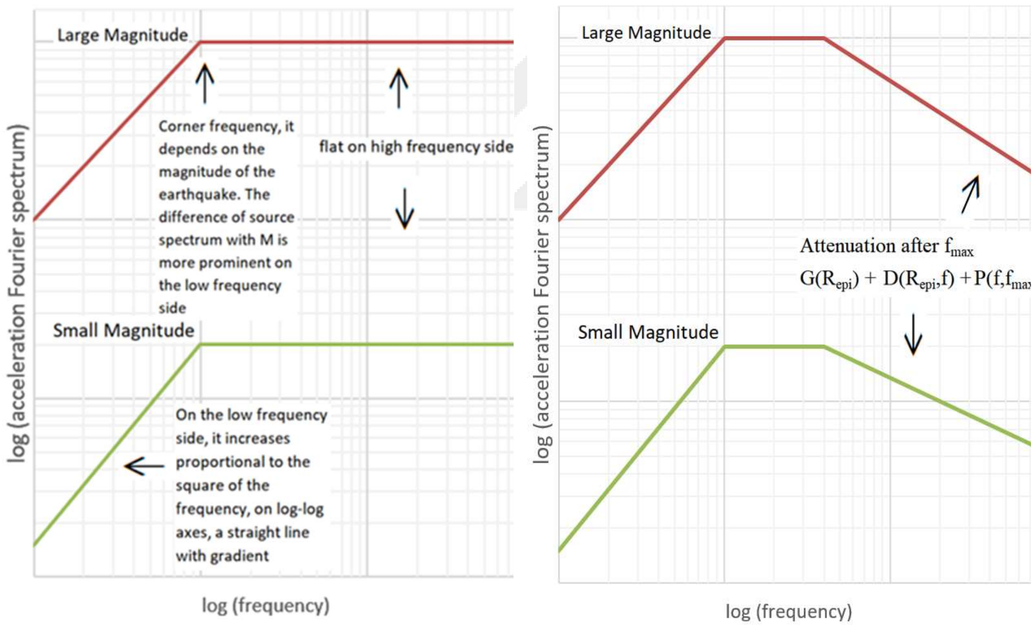

(a) (b)

Figure 2.1. Simplified sketches of (a) acceleration source spectra as defined by the omega-squared model of Brune (1970), (b) actual behavior of acceleration source spectra.

The corner frequency is given by:

$$f_c = 4.9 \, x \, 10^6 \, x \, \beta \, (\frac{\Delta\sigma}{M_0})^{1/3} \tag{2.5}$$

where β is the shear wave velocity at focal depth, Δσ is the stress drop, and M_0 is the seismic moment. Seismic moment defines the size of the earthquake and can be explained by the following Equation:

$$M_0 = \mu A D_0 \tag{2.6}$$

where μ is the shear modulus of the rock in the source region, A is the source fault area, and D_0 is the average value of the final slip on the fault surface. As shown in Eq. 2.5, f_c is inversely proportional to M_0 to the power of 1/3. Therefore, FAS is implicitly related to the seismic moment at low frequencies according to the omega-squared model. In Brune's omega-squared model, the corner frequency also depends on the stress drop, as shown in Eq. 2.5. Therefore, the spectral amplitudes above the corner frequency are proportional to $\Delta\sigma^{2/3}$. Hanks (1977) proposed that the stress drop is independent of the seismic moment, and it was generally in the range of 1 to 100 bars for moderate and large earthquakes. Later, Johnston (1994) calculated the mean stress drop as 85 bars from 83 stable continental region earthquakes. However, stress drop changes from region to region and even varies within the same region.

2.1 Geometric and Anelastic Attenuation, Attenuation at High Frequencies

Although the energy from the earthquake source at a short distance is dominated by shear waves, Lg waves carry most of the energy at large distances. Hermman and Kijko (1983) claimed that the L_g waves start dominating the ground motion about 70-100km range. With the knowledge of earth being inhomogeneous and the seismic waves recorded are the results of different wave arrivals even at short distances, FAS is controlled first by up-going S-waves, then by diving direct S-waves, then by reflections from the mid-crustal layer or Moho discontinuities as distance increases (Pezeshk, 1996). This transition results in the frequency-independent geometric attenuation, $G(R_{epi})$.

The anelastic attenuation term describes factors that cause ground motion amplitude to decay other than geometrical spreading. Parameters like crustal structure and its properties affect anelastic attenuation, so it is a regional term. The anelastic attenuation term in Eq. 2.3 is described as:

$$D(R_{epi}, f) = \exp\left[-\frac{\pi f R_{epi}}{Q_{eff}\beta}\right] \quad (2.7)$$

where Q_{eff} is the effective seismic quality factor of the S-wave. It is impossible to obtain a consistent Q_{eff} for a region because of the complexity of the crustal properties and the variety of ways that it affects anelastic attenuation (Pezeshk, 1996).

Contrary to Brune's (1970) simplified omega-squared model, earthquakes are quite variable with stress drop, rupture velocity, and slip. In Brune's model and other theoretical source spectral models used in predicting the ground motion spectra, spectra of the acceleration are constant at high frequencies (Figure 2.1(a)). However, the observed FAS from accelerograms usually fall off rapidly beyond some frequency, as demonstrated in Figure 2.1(b). Hanks (1982) noted that the acceleration spectrum follows a flat line up to a limiting frequency, which he referred to as f_{max}, then shows what is called "the crashing spectrum syndrome," a significant decay at high frequencies (Figure 2.2). Papageorgiou and Aki (1983) claimed the decay was influenced by the seismic source.

Anderson and Hough (1984) had used recordings from California to claim that the spectral fall-off mentioned earlier is caused by the subsurface geological structure.

The high cut filter in Eq. 2.3 can be formulated as:

$$P(f, f_{max}) = [1 + (f/f_{max})^{2n}]^{-1/2}\, exp(-\pi\kappa\, f) \qquad (2.8)$$

Where f_{max} is the frequency limit in the ground motion as defined by Hanks (1982), n is the order of the Butterworth filter (usually n=4) and is the slope of the crash syndrome.

After Boore (1983) introduced the first term in Equation (2.8), Anderson and Hough (1984) proposed the second term in Equation (2.8) to examine this attenuation, where it was measured directly from the high-frequency part of the FAS showing different characteristics than Brune's omega-squared model In application, researchers mostly use the second term in Equation (2.8) as:

$$A(f) = A_0 \exp(-\pi\kappa\, f)\,, f > f_{max} \qquad (2.9)$$

where f_{max} (also referred to as f_1) is the frequency above which the decay is nearly linear on the plot of log Fourier amplitude vs. linear frequency and continues up to f_2 where noise governs the FAS except where high resonance peaks are present (Figure 2.3). The slope of the linear approximation of the crash syndrome is defined as $-\pi\kappa$. Anderson and Hough (1984) also noted that since Q_{eff} is not dependent on frequency while the effect of high-frequency attenuation on source displacement spectrum is proportional to f^{-2} results in the spectral shape given in Figure 2.2.

Introduced by Anderson and Hough (1984), kappa describes the deviation at high frequencies between observed Fourier amplitude spectra of shear waves from seismograms and the omega-squared model. Tsai and Chen (2000) have suggested that the cause of this deviation from the omega-squared model is a combination of source, distance, and site while noting that the distance has the least effect on it.

Hough et al. (1988) and Hough and Anderson (1988) studied the kappa values from Southern California using small earthquakes and latter proposed the following model for kappa,

$$\kappa(\mathrm{r}) = \int_{pat} Q_i(z)^{-1} V_S\,(z)^{-1} dr \qquad (2.10)$$

where V_S is the shear wave velocity of the recorder site.

According to Sato et al. (2002), Equation (2.10) can be reformulated as:

$$\kappa(r, f) = \kappa_0 \exp\,(-\pi \mathrm{fr}/\mathrm{Q}_{eff}\ V_S) \qquad (2.11)$$

where V_S is the shear wave velocity of the medium.

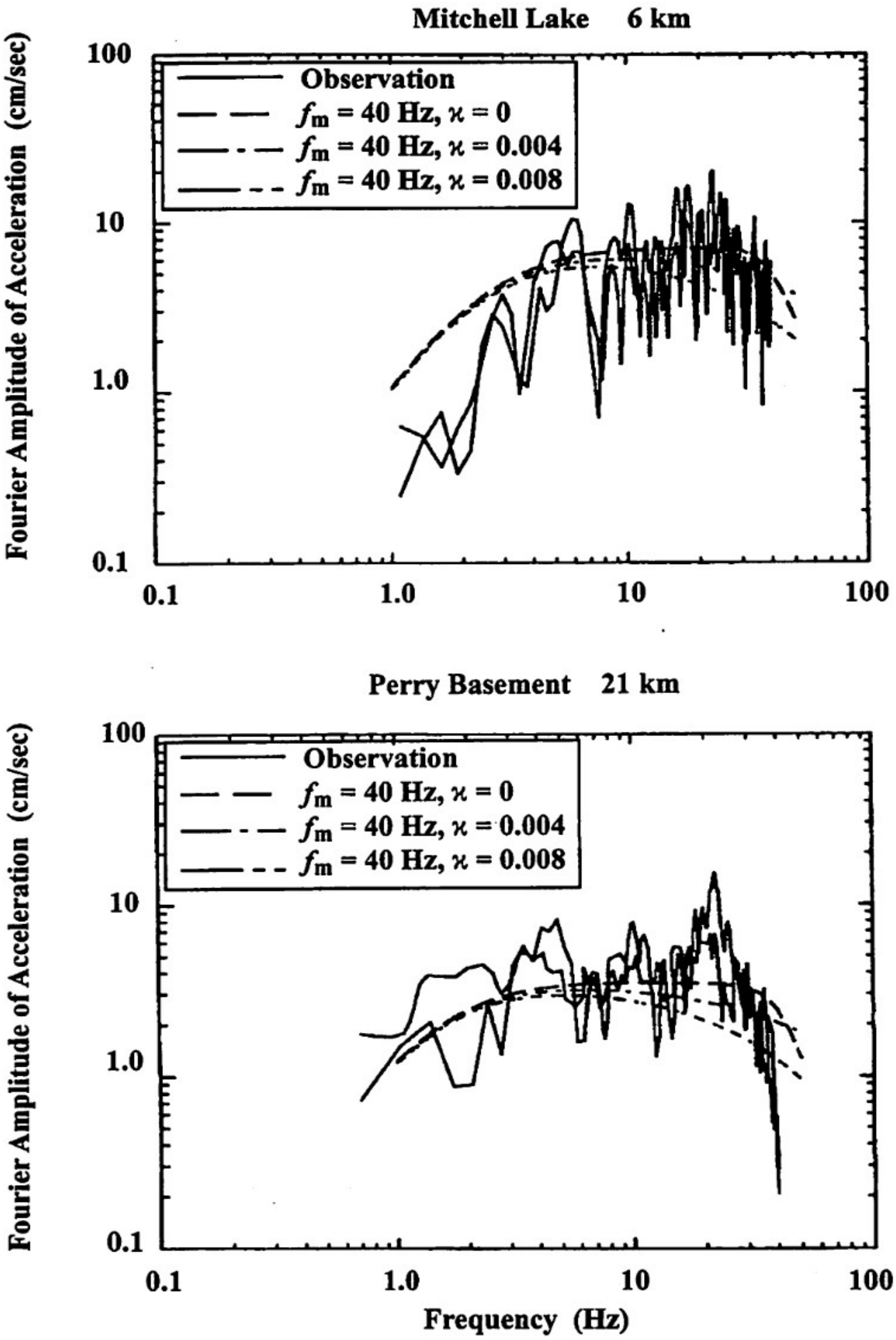

Figure 2.2. Comparison of observed and Brune's FAS using different high-cut filters (taken from McGuire et al. 1988)

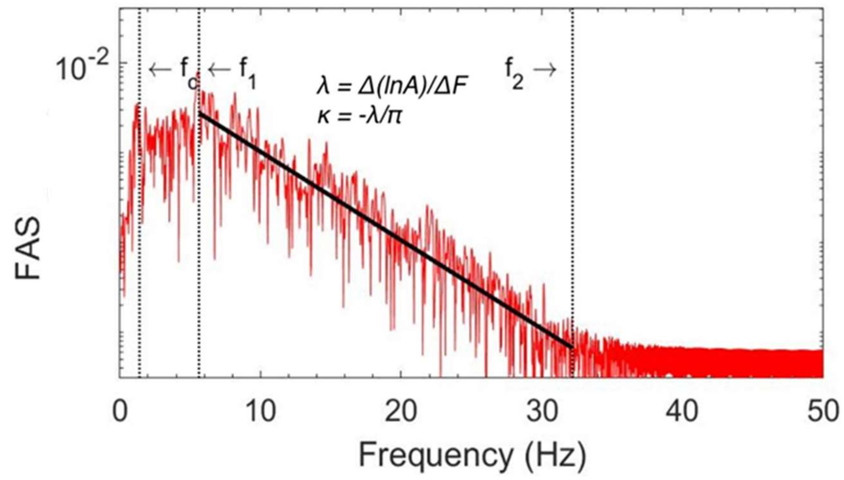

Figure 2.3. The slope of the high-frequency attenuation (between f_1-f_2)

Anderson and Hough (1984) also noted that the κ at individual stations tends to increase with distance, and both the local geology a few kilometers beneath the station and the regional structure affects the value of κ. Theoretically, kappa is a site and distance-dependent parameter that defines the attenuation of seismic waves from the source to the receiver but taking out these dependencies is possible. Path contributions can be removed by correcting FAS by deconvolving Q models for the region if any exists. By employing this method, FAS would yield κ_0 values rather than distance-dependent κ_r values. However, this process would introduce uncertainties from Q models, especially because Q models are generally determined at low frequencies where κ estimation takes place in high frequencies (Ktenidou et al., 2016). The site component zero-distance κ (referred to as κ_0) could be computed by the linear extrapolation of the κ_r (individual observations of κ) to R_{epi}=0 as shown in Figure 2.4 to correct for the regional effects of anelastic attenuation as:

$$\kappa_r = \kappa_0 + \kappa^{\sim}(R_{epi}) \quad (2.12)$$

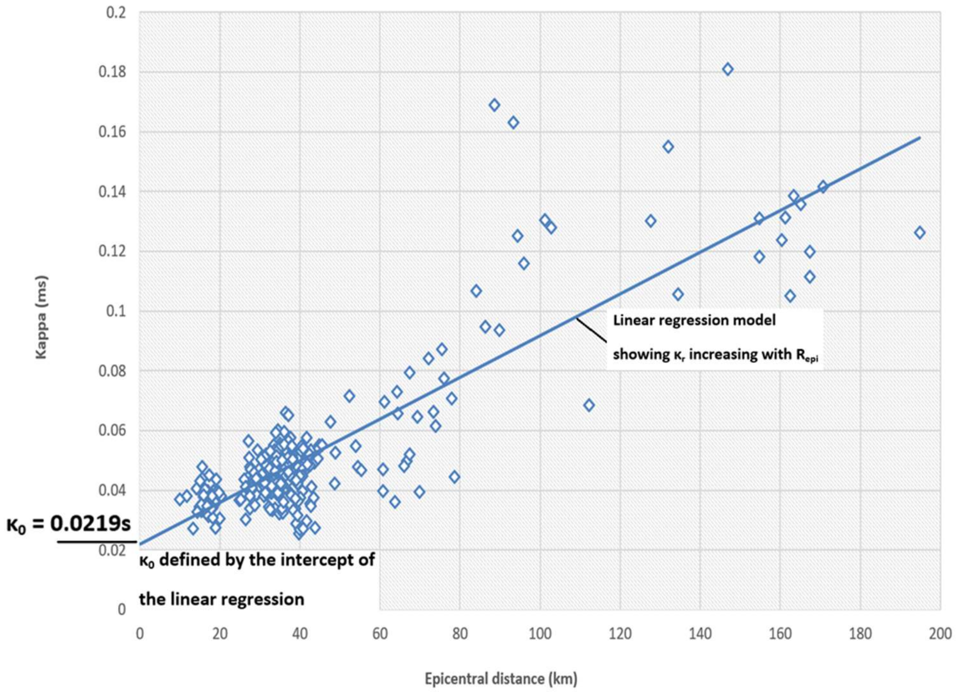

Figure 2.4. Epicentral Distance vs. Kappa Scatter explaining κ_r and κ_0

2.2 Methods to Estimate Kappa and Its Field of Application in Engineering Practice

Since the first introduction of κ, several methods other than the method offered by Anderson and Hough (1984) have been offered to estimate this parameter. A short summary of these methods is provided below:

- Suggested in 1991 by Anderson and Humphrey and later improved by Anderson (1992), Silva et al. (1997), and Edwards et al. (2011), broadband inversion of the entire spectrum for source, path, and site terms have been used to estimate kappa from broadband recordings. This method does not remove Q effects and yields to a distance-dependent kappa.
- Silva and Darragh (1995) and Silva et al. (1998) offered to fit the stochastically simulated response spectra coupled with site amplification

effects to the observed response spectra over the entire frequency band to estimate kappa. This method effectively removes Q effects and yields to a distance-independent, site-specific kappa to be used in the host-to-target adjustment of ground motion prediction equations.

- Frankel et al. (1999) and Drouet et al. (2010) used direct measurement on the site amplification transfer function to estimate kappa. This method also effectively removes the Q effects and yields to a distance-independent, site-specific kappa for stochastic simulations.
- In 2001, Biasi and Smith came up with a method to obtain kappa for small-magnitude earthquakes by implementing the direct measurement on the low-frequency part of the Fourier displacement spectrum considerably below f_c. This method does not remove the Q effects and results in a distance-dependent kappa.
- Margaris and Boore (1998) and Oth et al. (2011) measured kappa directly from the source spectrum after removing the path and site effects and averaging across all spectra recorded at the same site. The method yields a distance-independent kappa.
- Al Atik et al. (2014) offered a new method to obtain a distance-independent kappa by measuring it directly on the Fourier spectrum derived from IRVT as compatible with the GMPE response spectrum.

Kteniodu et al. (2014) proposed the nomenclature to distinguish the estimated kappa values from each method given above. The nomenclature used for these methods is κ_{r_AS} for the acceleration spectrum approach (a.k.a. the Anderson and Hough (1984) method), κ_{r_DS} for the displacement spectrum approach, κ_{BB} for the broadband approach, and κ_{0_RESP} for the response spectral shape approach, κ_{0_TF} for the transfer function approach, κ_{r_SS} for source spectrum approach, and κ_{r_IRVT} for measurement on IRVT-derivated FAS. In this study, the classical Anderson and Hough (1984) approach (κ_{r_AS}) is used because it is the most suitable method for strong-motion recordings from M>4 earthquakes.

The high-frequency attenuation (kappa) parameter has been used in various ways with different objectives. In source modeling studies, eliminating the attenuation effect is vital to obtain self-similarity of the spectrum and can be done by using inverted theoretical Q using EGFs (Green's functions) or multiple EGFs to remove path and site effects (Ktenidou et al., 2014). κ_0 has also been used as a low pass filter to constrain high frequencies in studies of synthetic ground motion with finite fault stochastic, point-source, or hybrid applications. (Boore, 1986; Beresnev and Atkinson, 1997; Boore, 2003; Graves and Pitarka, 2010). Campbell (2003; 2004) had used the hybrid empirical method to adjust ground motion prediction equations (GMPEs) from host region for a soft-rock site to a less seismologically active target region for a hard-rock site using V_{S30} and κ_0 corrections accounting both for site amplification, which dominates lower frequencies and site attenuation which dominates high frequencies. For projects of critical facilities such as nuclear power plants, during probabilistic seismic hazard assessment (PSHA), adjusting GMPEs even within the same region is required. The Probabilistic Seismic Hazard Analysis for Swiss Nuclear Power Plant Sites (PEGASOS) Refinement Project (Biro and Renault, 2012) showed that the κ_0 corrections on GMPEs could lead up to a factor of 3 for seismic hazards. Figure 2.5 shows correction factors for κ_0 on GMPEs calculated by Biro and Renault (2012).

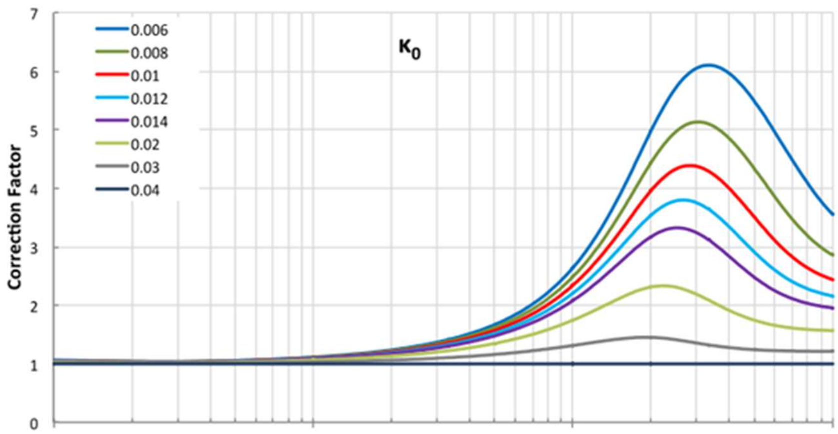

Figure 2.5. The κ_0 correction functions evaluated for Abrahamson and Silva GMPE, Fixed Host Kappa=0.04, Varying Targets (2008) (After Biro and Renault, 2012)

2.3 Previous Studies on Regional Kappa Estimation for Hard Rock Sites

Drouet (2010) has estimated regional kappa from acceleration FAS for France using strong-motion accelerograms from the French Accelometric Network (RAP, Pequegnat, et al. 2008) for the regions of French Pyrenees, French Alps, and Rhine Graben. One hundred sixty-one earthquakes occurred between 1996-2006 with magnitudes ranging between 3.0 and 5.0, mostly at 5-6km depths; recorded at 76 accelerometric stations have been utilized. Two horizontal components with the minimum signal to noise ratio (SNR) of 3 have been geometrically combined. The FAS has been smoothed between 0.1Hz and 30Hz using the Konno-Ohmachi procedure (Konno & Ohmachi 1998). Recordings, which have been grouped according to regions given above, concentrate on the epicentral distances of 0-30km on the Alps, 30-50km in the Rhine, 20-40km in the Pyrenees, while all recordings are crustal and from soft, intermediate and hard rock stations. Estimated zero-distance kappa values from this study are given with blue crystals in Figure 2.6.

Van Houtte (2011) estimated κ_0 for all KIK-net (Japan) and some NGA stations (mostly California and Taiwan) with measured V_{S30} values higher than 500 m/s using the recordings between the years 1998 and 2006, including the borehole recordings from KIK-net. Recordings have been grouped into two categories according to the event depth being larger or smaller than 25km. The recordings, which resulted in a more than 25% difference between kappa values of the two orthogonal components, were eliminated. The resulting kappa values from this study are represented with red squares in Figure 2.6.

Ktenidou (2012) estimated κ_0 values for six hard-rock broadband stations with V_{S30} values ranging between 1000 and 3000 m/s from Switzerland. The data set contains 1158 two-component records with magnitudes ranging from 2 to 5.5 with the maximum epicentral distances of 200km, half of the events being M_w <3.0. Results of this study can be seen in Figure 2.6, marked with purple crosses.

Van Houtte and Ktenidou (2013) estimated κ_0 values for hard-rock stations in Christchurch, New Zealand. The study contained the recordings from 7 Geo-Net, free-field, surface stations, and 6 of them were located on the rock and stiff-soil sites. All of the stations except one were strong-motion stations while one has a broadband recorder; however, almost half of the data used in this study is from this single broadband station. All events used for this study have their focal depths less than 15km, with a total of 2163 recordings. The maximum epicentral distance is around 90km, and 70% of the dataset has epicentral distances lower than 30km. They did not set a minimum moment magnitude cut-off for their study as most of their data lies below magnitude 3.0 for the broadband station, while nearly all of the data obtained from strong-motion stations were above 3.5. In this study, a set of criteria has been used to determine f_2 rather than handpicking it. Smallest of the frequencies where SNR<3, or where the high-frequency slope flattens or the maximum usable frequency of the instrument of the recording has been chosen as f_2. Estimated kappa values from this study are represented with red crosses in Figure 2.6.

Ktenidou et al. (2016) estimated κ_0 for the Arizona region using the local strong-motion database. The dataset was composed of 202 three-component records from 26 events and 14 stations. The magnitude for these events ranged from 1.2 to 7.2, with the epicentral distances varying between 9-650km. Measured V_{S30} values of the stations had a wide range between 398m/s and 1312 m/s. Visual elimination of noisy and faulty recordings had been carried out. P-wave arrival times have also been visually selected, and the S-wave arrival times were calculated from the formula,

$$t'_s = t_p + \Delta t_{s-p} \approx t_p + R_h/8 \qquad (2.13)$$

where R_h is the hypocentral distance, t_p is the P-wave arrival time, $\Delta t_{(s-p)}$ is the time difference between P and S-wave arrival time, and t'_s is the S-wave arrival time. To calculate $\Delta t_{(s-p)}$, the P and S-wave velocities were taken as 6.0 and 3.5km/s, respectively. Determining the S-wave window ending time was also automated using a function of magnitude and hypocentral distance. Equation 2.5 was utilized to determine the theoretical corner frequency to reduce bias in manual corner frequency selection. Ktenidou et al. (2016) assumed that β is equal to 3.2 km/s while assuming a stress drop of 100 bars, a claimed average value for the large earthquakes in California from the literature. Since the study focused on κ_R rather than κ_0, no results from the report have been included in Figure 2.6.

Neighbords et al. (2015) estimated κ_0 values using the ground motions recorded in the 2010 Chile earthquake (M_w=8.8) aftershocks. The authors used a strong motion dataset from 229 events with local magnitudes ranging from 4.0 to 6.7 and epicentral distances ranging from 9 to 176 km. These recordings were obtained from 50Hz voluntary-based universal serial bus recorders both on sediments and soft/hard rock sites. In this study, the automated f_{max} and f_2 picking method (Gentili & Franceschina, 2011) have been used in which resulted in f_{max} values ranging from 1-13Hz and f_2 values ranging between 11-23Hz. The study found a 22.5% difference in κ_0 values of two-components with a median value of 14.4%. This study lacks V_{S30} profiles for the recording stations; therefore, findings are not included in Figure 2.6.

Following that, Castro (2015) had worked on kappa estimates for the Gulf of California, Mexico. The database included 13 shallow earthquakes with focal depths less than 20km, magnitudes varying between 5.1 and 6.6, and epicentral distances ranging from 43 to 500km from 11 seismic broadband stations (20Hz). As the stations used in this study did not have available V_{S30} estimates, results are not included in Figure 2.6.

Pavel and Vacareanu (2015) estimated κ_0 values from 247 two horizontal component recordings of 9 intermediate-depth (60-180km) earthquakes in Vranchea-Romania with M_w>5.2 that occurred between 1986 and 2013. This strong ground motion dataset had been collected from 57 seismic stations, which are laid on A, B, and C class sites according to EN 1998-1. The study found that f_{max} values lie between 3-4Hz and f_2 values lie between 15-40Hz. As this study did not state any clear V_{S30} estimates other than soil classes for stations, results are not included in Figure 2.6.

Lai (2016) has used the data collected by borehole and surface seismic arrays to obtain κ_0 values for Taiwan from a large dataset of strong-motion records. The dataset consisted of 133 earthquakes recorded by 30 borehole seismic arrays with a sampling rate of 200Hz from 120-400m depth. Recordings have local magnitudes larger than 4.0 with focal depths less than 35km and recorded from the start of 2012 till the end of 2013. The author set a 5-second S-wave window from the arrival time of S-waves; while visually determining P and S-wave arrivals. The study only used the waveforms that have SNR >100. Recordings that have Δf (frequency range to calculate the slope in decay) less than 10Hz are disregarded. Results show the range of f_{max} between 2-15 Hz, where f_2 ranges from 11 to 50Hz. This study did not focus on the κ_0-V_{S30} relation, and it is not included in figure 2.6.

Stanko et al. (2017) estimated κ_0 values for the Central and Southern Dalmatia region of Croatia. The study used a database that contained recordings with local magnitudes larger than 3.0, focal depths less than 30km, and epicentral distance less than 150km. 4 seismological stations used in this study have their V_{S30} values ranging from 1050m/s to 1390m/s. The 3rd component kappa, or $\kappa_{vertical}$, values have also been estimated and found to be systematically lower than the κ values for the horizontal components. The findings of this study are shown by green circles in Figure 2.6.

Perron et al. (2017) estimated κ_0 values from strong-motion records for the Provence region of France. The dataset contained almost 500 crustal (depth<30km) small-magnitude earthquakes, and the magnitude values are mostly smaller than 3. Ground motions, with epicentral distances less than 180km, are recorded with Güralp CMG-6TD (100Hz), which is the same recorder for most of the stations in Turkey. Recorders were located on sites with V_{S30} values ranging from 440 to 2100 m/s. They eliminated recordings with SNR < 3. The kappa values obtained from this study are represented with purple crystals in Figure 2.6.

Kumar (2018) has estimated the κ_0 values for Western India. A total of 159 accelerograms of 34 earthquakes with M_w=3.3-4.9 from GSNET stations of having

V_{S30} between 480m/s to 2800m/s have been used in this study. This study followed the method of Anderson and Hough (1984) to estimate kappa like the previous studies mentioned. P-S arrival times, f_{max}, f_2 values had been handpicked. Dominant ranges found for f_{max} is 3-8Hz, while for f_2 is 42-50Hz. Results obtained from this study are represented with blue crosses in Figure 2.6.

Fu et al. (2019) had utilized 5700 three-component broadband seismic recordings from 233 earthquakes with magnitudes ranging from 3.5 to 5.0 that occurred between 2009 and 2013 to estimate κ_0 of the Longmen Shan region, eastern Tibetan Plateau, Southwest China. Dataset consisted of the earthquakes with the largest focal depth of 30km and largest epicentral distance of 300km. This study followed the broadband approach (κ_{BB}) to obtain κ_0 values. Results obtained from this study are represented with orange triangles in Figure 2.6.

Chang et al. (2019) have used 26,277 strong-motion seismograms from 679 stations located in Taiwan. The database consists of events with magnitudes ranging from 4.0 to 7.1 with focal depths less than 30km recorded during 1993-2014. With the help of a large database, the authors managed to obtain a κ_0 – V_{S30} relation for this region. Their study also confirmed an inverse relationship between magnitude and f_c. Results obtained from this study are represented with blue squares in Figure 2.6.

Alibazi (2019) estimated κ_0 values of Western Iran using a database of strong-motion recordings. The database contains ten earthquakes from 76 accelerograms recorded between 1973 and 2018. Epicentral distances of the recordings range from 8 km to 161km, with magnitudes ranging from 5.1 to 7.3. The study did not present the V_{S30} values for the stations; therefore, the findings cannot be added to Figure 2.6.

Another kappa study for the Southern Rocky Mountains of Central Colorado has been conducted by Darragh et al. (2019). This study had used a database of 24 earthquakes with magnitudes ranging from 1.5 to 3.3 from 84 seismic stations with NEHRP site categories of A, B, C, and D. κ_0 values have been calculated with the broadband inversion methodology (κ_{BB}).

Mittal et al. (2020) studied the κ_0 values of the Himalayan Region of India using a limited dataset that includes 81 recordings from 50 stations. The database consisted of strong-motion records from earthquakes from generally shallow depths (<20km) with a minimum magnitude of 3.0. The study did not present the V_{S30} values for the stations; therefore, the findings cannot be added to Figure 2.6.

Palmer et al. (2020) estimated κ_0 values of Canada using a database consists of 20 earthquakes recorded on nine stations in eastern Canada and 404 earthquakes recorded on eight stations in western Canada. The database included evenly distributed data over the 0-150km epicentral distance range from mostly soft rock sites. The study used both a modified version of the classical S-wave acceleration method as well as a new stacking method that is consistent with the use of kappa in ground-motion modeling. It is found that the classical method resulted in a lower scatter than the new stacking method. This study did not focus on the κ_0-V_{S30} relation, and it is not included in Figure 2.6.

Kumar et al. (2020) studied the κ_0 values of the Northwest and Northeast Himalaya region using 294 triaxial strong motion records from 60 sites in NW Himalaya and 26 sites in NE India with V_{S30} values ranging from 220m/s to 900m/s. Most of the stations located in NE Himalaya were not hard-rock stations. The authors found a large scatter from combined data on NE and NW Himalayas, not showing an obvious trend as claimed. The results obtained from this study are represented with purple crosses in Figure 2.6.

A closer look at Figure 2.6 shows that the scatter in zero-distance kappa for the same site conditions is significant. Unexpectedly, no clear trend is visible for the change in zero-distance kappa with increasing V_{S30} value, and it is hard to understand if the data has any regional trends.

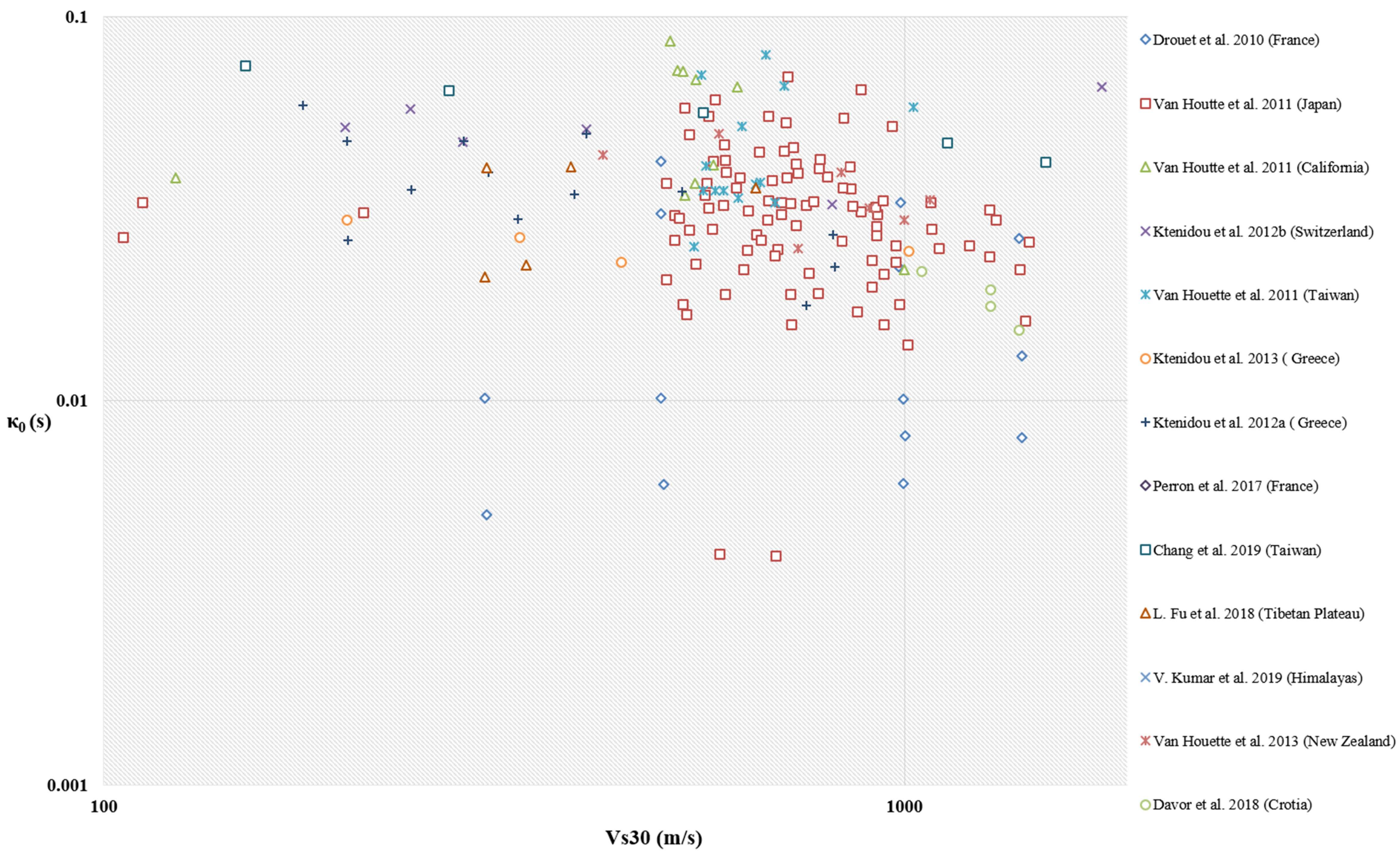

Figure 2.6. Previous Studies on Kappa (using Anderson and Hough method))

2.4 Previous Studies on Kappa Estimation in Turkey

Previous studies on high-frequency attenuation parameters (kappa) for Turkey are quite limited and mostly concentrated on Western Turkey. A summary of the earlier efforts is listed below:

- Askan et al. (2014) used 142 strong ground motions recorded at 15 stations with V_{S30} values between 228-701 m/s in Northwestern Turkey to generate a regional κ model and used Gölkaya (M_w=5.2) and Düzce (M_w=7.1) earthquakes to validate their study. The maximum epicentral distance for the recordings used in this study was 200km. Their study found f_{max} values ranging between 1-11Hz and f_2 values ranging between 20-45Hz. Blue diamonds in Figure 2.7 show the findings of Askan et al. (214).
- Kurtulmuş et al. (2015) used a database consisted of 1764 records from 322 events from Western Anatolia with magnitudes ranging from 2.0 M_L to 5.6 M_L and a 3.5-205km epicentral distance range. The generalized inversion technique was used in their study. They compared those to the horizontal-to-vertical spectral ratio (HVSR) and stated that the HVSR might underestimate the results. The study ignored the Q, regional attenuation effect while averaging kappa values from 27 stations to find κ_0=0.031 for the Western Turkey region.
- Tanırcan et al. (2018) have studied horizontal κ_0 values for three downhole arrays and two engineering bedrock sites with V_{S30} values ranging from 200m/s to 800m/s located at the western side of Bosporus. The database included recordings with a magnitude range of $3.0<M_L<4.8$ up to 200km epicentral distance. A constant regional attenuation was used as the study covers a small region. The f_1 values ranged between 4-20Hz and f_2 values ranging between 15-48Hz while maintaining a minimum of 10Hz rule for $f_2 - f_1$. Since the two sites do not have a measured V_{S30}, results are not included in figure 2.7.

- Biro et al. (2020) estimated the κ_0 values for hard-rock stations using Turkey's strong ground motion database. The study used 711 events recorded from 14 hard-rock sites with V_{S30} values higher than 720 m/s. The database's magnitude range was between $3.5<M_L<6.2$, while the maximum epicentral distance is set to be 100km. Results, where two-component kappa differences exceeded 25%, were disregarded.

Scatter for global results versus Turkey's results shows similarities on the graph, but the kappa obtained for Turkey lacks data for low V_{S30} values while for high V_{S30} values, κ_0 results show no clear pattern. This is also caused by a lack of sufficient data over the V_{S30} range. One should note that results obtained by Askan et al. (2014) fit global data but lacks hard-rock site results.

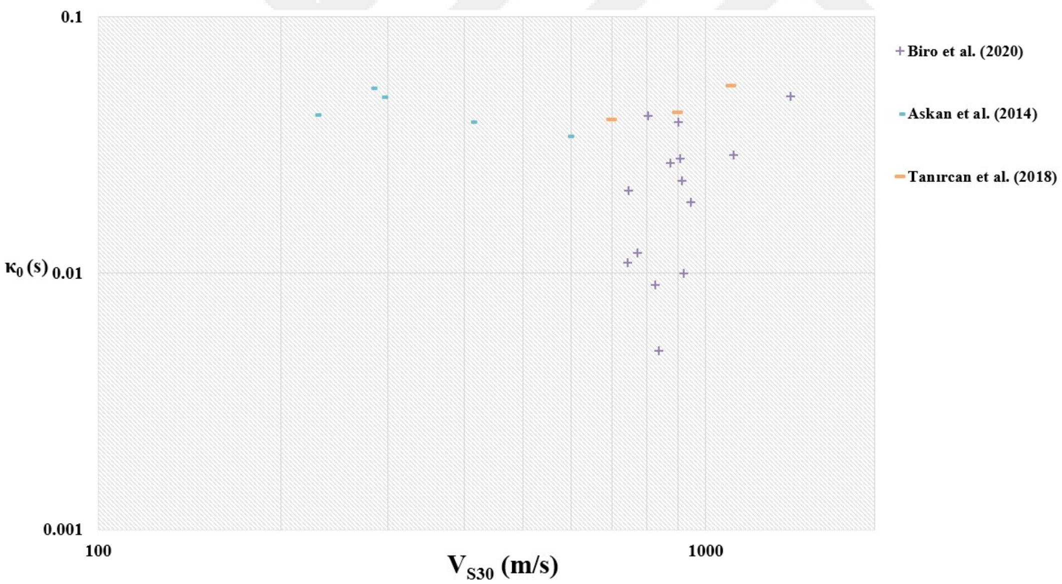

Figure 2.7. Previous Studies on Kappa from Turkey (using Anderson and Hough method))

CHAPTER 3

DATA COMPILATION AND METHODOLOGY FOR ESTIMATION OF HIGH-FREQUENCY ATTENUATION PARAMETER

3.1 Selection Criteria for the Strong Motion Recording Stations and Compilation of the Dataset

There are 764 strong ground motion stations in Turkey that are operated by the Disaster and Emergency Presidency of Turkey (AFAD), Department of Earthquake. Station information, including the coordinates, elevation, topography, results of the geotechnical and geophysical measurements at the station location, is disseminated through AFAD's website (https://tadas.afad.gov.tr/). However, available information on each strong-motion station is not uniform; for example, the site characterization for the stations that were located before 2007 was performed and documented by Middle East Technical University (METU); while the stations that were located between 2007 and 2016 were characterized by Kocaeli University in coordination with AFAD. For these two groups of stations, the geophysical methods that were used to measure the shear wave velocity (Vs) profile and the documentation of test results are different. The site characterization for the stations located after 2017 was not performed as of this date; therefore, the average shear wave velocity at the first 30 meters (V_{S30}) is unknown for these stations.

To be able to represent the hard rock site conditions for kappa estimations, 54 stations with V_{S30}>740 m/s have been selected, as shown in Table 3.1. Approximately 60% of these stations have a limited number of recordings (less than 100) from magnitude three or larger earthquakes; therefore, these stations are excluded from the dataset. Twenty-two stations with V_{S30}>740 m/s that have more than 100 recordings from M>3 earthquakes were picked for this study (Table 3.2). Once the recordings with epicentral distances (R_{epi}) higher than 200 km were eliminated, the number of recordings in one of the stations (Station ID#0901) is dropped below 100; however, this station is not excluded from the dataset. At this point, there are 6463 recordings with M>3 and R_{epi}<200 km from 22 recording stations in the compiled dataset. All the selected stations, except for ST#4802, have the same type of recorders (GURALP CMG-5T, 100Hz), as shown in Table 3.1.

Table 3.1 Station codes, station names, recorder types, V_{S30} values, and the number of available recordings for the stations operated by AFAD that represent the hard-rock site conditions (sorted by the number of recordings).

Code	**Province**	**District**	V_{S30}	**Number of Recordings**	**Recorder Type**
3520	İzmir	Konak	875	584	GURALP CMG-5T
3511	İzmir	Bornova	827	525	GURALP CMG-5T
4808	Muğla	Menteşe	1323	405	GEOSIG GMS+ AC-73
3514	İzmir	Bayraklı	836	404	GURALP CMG-5T
4404	Malatya	Pütürge	1380	397	GURALP CMG-5T
0919	Aydın	Karpuzlu	986	375	GEOSIG GMS+ AC-73
4809	Muğla	Bodrum	747	371	GURALP CMG-5T
3536	İzmir	Seferihisar	1141	367	GEOSIG GMS+ AC-73
1708	Çanakkale	Merkez	1005	354	GURALP CMG-5T
4817	Muğla	Milas	948	352	GEOSIG GMS+ AC-73
2302	Elazığ	Maden	907	348	GURALP CMG-5T
0920	Aydın	Söke	894	347	GEOSIG GMS+ AC-73
4406	Malatya	Akçadağ	815	279	GURALP CMG-5T
2305	Elazığ	Palu	907	264	GURALP CMG-5T
4818	Muğla	Kavaklıdere	1080	263	GEOSIG GMS+ AC-73
3506	İzmir	Konak	771	233	GURALP CMG-5T
2309	Elazığ	Keban	860	221	GURALP CMG-5T
2409	Erzincan	Kemaliye	875	158	GURALP CMG-5T
0705	Antalya	Kaş	1113	125	GURALP CMG-5T
0707	Antalya	Kaş	1822	112	GURALP CMG-5T
4802	Muğla	Bodrum	747	100	GURALP CMG-5T
1101	Bilecik	Merkez	901	79	GURALP CMG-5T
0206	Adıyaman	Besni	863	72	GURALP CMG-5T
0716	Antalya	Kaş	813	72	GEOSIG GMS+ AC-73
2703	Gaziantep	Şahinbey	758	67	GURALP CMG-5T
1806	Çankırı	Merkez	885	59	GEOSIG GMS+ AC-73
3417	İstanbul	Sultanbeyli	1747	56	GEOSIG GMS+ AC-73
3405	İstanbul	Kartal	1862	55	GURALP CMG-5T

Table 3.2 (cont.) Station codes, station names, recorder types, V_{S30} values, and the number of recordings for the stations operated by AFAD that represent the hard-rock site conditions (sorted by the number of recordings).

Code	**Province**	**District**	V_{S30}	**Number of Recordings**	**Recorder Type**
3116	Hatay	İskenderun	870	54	GURALP CMG-5T
1807	Çankırı	Kurşunlu	1076	51	GEOSIG GMS+ AC-73
2412	Erzincan	Merkez	955	50	SARA ACEBOX SA10
5814	Sivas	Gölova	804	46	SARA ACEBOX SA10
8105	Düzce	Merkez	914	35	GURALP CMG-5T
129	Adana	Tufanbeyli	965	34	SARA ACEBOX SA10
3307	Mersin	Anamur	855	28	GEOSIG GMS+ AC-73
118	Adana	Çukurova	946	26	GURALP CMG-5T
508	Amasya	Merkez	942	26	GURALP CMG-5T
6303	Şanlıurfa	Siverek	986	24	GURALP CMG-5T
2016	Denizli	Honaz	805	24	GURALP CMG-5T
6302	Şanlıurfa	Viranşehir	936	23	GURALP CMG-5T
3418	İstanbul	Tuzla	1182	20	GURALP CMG-5T
4813	Muğla	Kayabaşı	1040	18	GURALP CMG-5T
5506	Samsun	Kavak	1510	16	SARA ACEBOX SA10
3302	Mersin	Gülnar	1007	16	GURALP CMG-5T
4119	Kocaeli	Dilovası	884	14	GURALP CMG-5T
4124	Kocaeli	Körfez	906	13	GURALP CMG-5T
5202	Ordu	Akkuş	1024	12	SARA ACEBOX SA10
4102	Kocaeli	İzmir	1000	12	GURALP CMG-5T
6601	Yozgat	Merkez	906	12	GURALP CMG-5T
4125	Kocaeli	İzmit	826	11	GURALP CMG-5T
5813	Sivas	Doğanşar	978	8	SARA ACEBOX SA10
701	Antalya	Muratpaşa	920	8	GURALP CMG-5T
3122	Hatay	İskenderun	1011	3	GURALP CMG-5T
5805	Sivas	Altınyayla	1072	1	GURALP CMG-5T

Figure 3.1 shows the spatial distribution of the selected strong ground motion stations. According to this figure, the majority of the selected stations are in Western Turkey; there are five stations in both İzmir and Muğla, two stations are located in Aydın, and two stations are located around Bilecik and Çanakkale. Assuming that the attenuation characteristics of the closely located stations are similar, selected stations are grouped by their locations, as shown in Table 3.2. There are six stations in Eastern Turkey that are located in Elazig, Malatya, and Erzincan, which are grouped into a single category as the Elazig-Malatya group. It is notable that the number of recordings in each group is quite uniform; however, the M-R_{epi} distributions of stations might be different.

Table 3.3 Stations selected for this study (grouped according to geographical locations)

Code	Province	District	V_{S30} (m/s)	Number of Data (M_w>3.0 R_{epi}<200km)	Geological Group	Geotechnical Report
3506	İzmir	Konak	771	224	İzmir Group	Obtained
3511	İzmir	Bornova	827	509		Obtained
3514	İzmir	Bayraklı	836	394		Obtained
3520	İzmir	Konak	875	564		Obtained
3536	İzmir	Seferihisar	1141	360		Obtained
0919	Aydın	Karpuzlu	986	362		Obtained
0920	Aydın	Söke	894	333		Obtained
2302	Elazığ	Maden	907	348	Elazığ-Malatya Group	Not Obtained
2305	Elazığ	Palu	907	263		Obtained
2309	Elazığ	Keban	860	221		Obtained
2409	Erzincan	Kemaliye	875	157		Obtained
4404	Malatya	Pütürge	1380	394		Not Obtained
4406	Malatya	Akçadağ	815	272		Obtained
4802	Muğla	Bodrum	747	80	Bodrum Muğla Group	Obtained
4808	Muğla	Menteşe	1323	382		Obtained
4809	Muğla	Bodrum	747	364		Obtained
4817	Muğla	Milas	948	342		Obtained
4818	Muğla	Kavaklıdere	1080	250		Obtained
0705	Antalya	Kaş	1113	125	Antalya Group	Not Obtained
0707	Antalya	Kaş	1822	101		Not Obtained
1101	Bilecik	Merkez	901	71	Biga Group	Not Obtained
1708	Çanakkale	Merkez	1005	347		Obtained

Figure 3.1. Map showing the distribution of selected strong-motion stations.

Available recordings in each station are downloaded from https://tadas.afad.gov.tr/. It is noted that the magnitude scales given on AFAD's website for these recordings is not uniform. The magnitudes of approximately 40% of the recordings (with magnitudes varying between 3.0 and 4.0) are reported in local magnitude scale (M_L), and around 5% of the recordings either have duration magnitude (M_D) or body-wave magnitude (m_b) values. The moment magnitude (M_w) estimates of the remaining recordings (almost all recordings with M>4.5) are provided by AFAD. Magnitude conversion formulas proposed by Kadiroğlu and Kartal (2015), given in Eq. 3.1-3.3, are utilized to convert other magnitude scales to M_w for consistency with the reported M_w values by AFAD.

$$M_w = M_L \times 0.8095 + 1.3003 \quad (3.1)$$

$$M_w = M_D \times 0.8949 + 1.342 \quad (3.2)$$

$$M_w = M_b \times 1.0319 + 0.0223 \quad (3.3)$$

Figure 3.2 shows the magnitude-epicentral distance distribution of the recordings in the initial dataset. The number of recordings in the first 10km is very limited, and the majority of data with R_{epi}<10 km are recorded by Kaş (ID#0705), Palu (ID#2305), and Bodrum (ID# 4809) stations. Approximately 17% of the recordings are located in the "near-field" (R_{epi}<30 km), and almost all of these recordings are from small magnitude events (M_w<5). Approximately 50% of all recordings have R_{epi} values varying between 50km to 100km. The dominating magnitude range (consisting of 74.1% of the data) is M_w=3.5-4.5. Nearly all recordings are from shallow crustal events (depth<40km), while recordings from deeper earthquakes are available in stations from Muğla-Bodrum Group.

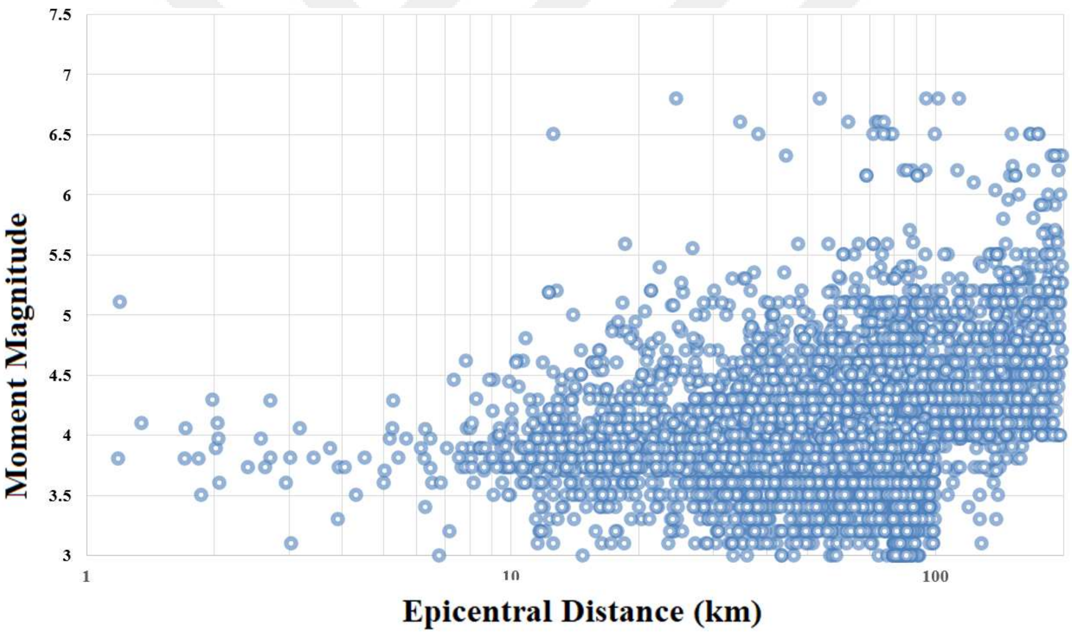

Figure 3.2. Magnitude-epicentral distance distribution of the recordings in the initial dataset.

Figure 3.3 presents the distribution of the recordings in V_{S30} bins, indicating that most of the recordings are recorded in stations with 800m/s>V_{S30}>1000m/s. There is only a limited number of data available for V_{S30}>1400m/s, and all of them are recorded by the same station (Kaş, ID#0707). Figure 3.4 shows that the distribution of data with magnitude is similar for each V_{S30} range; the bulk of the data is from small magnitude events (M_w<5), but recordings from large magnitude events are available.

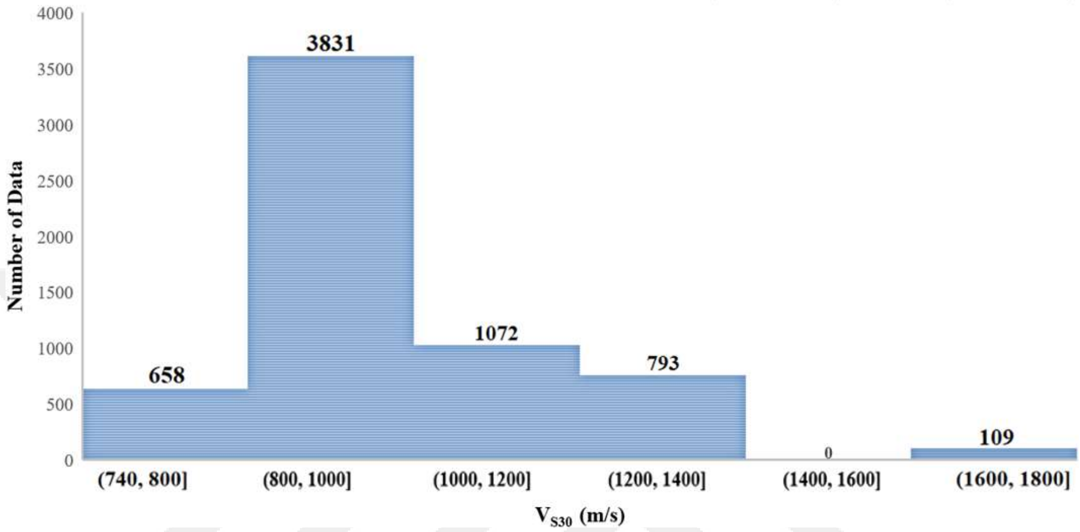

Figure 3.3. The number of recordings in the initial dataset in equally spaced V_{S30} bins.

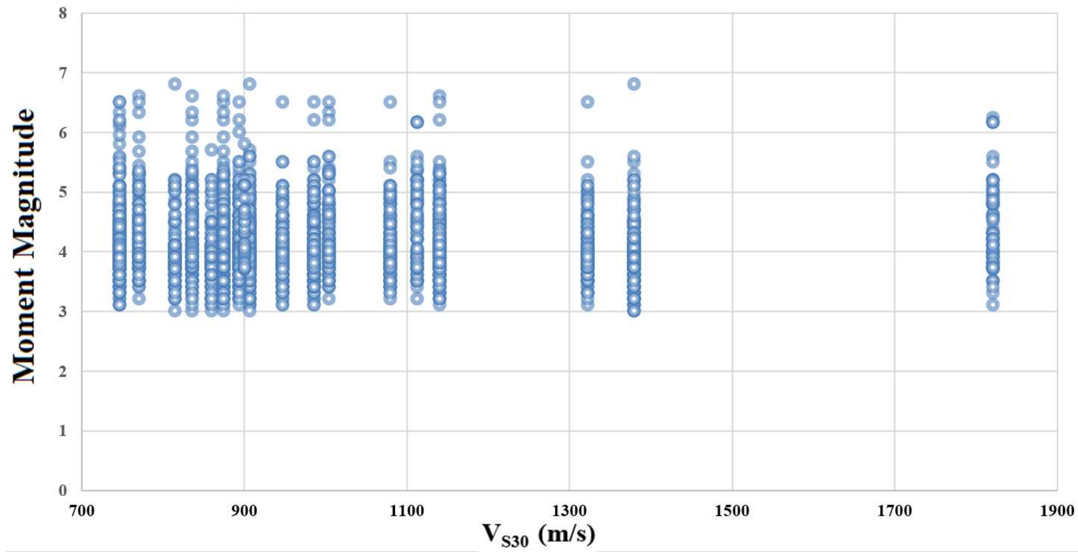

Figure 3.4. Magnitude- V_{S30} distribution of the recordings in the initial dataset

Figures 3.5 to 3.12 present the spatial distribution of the earthquakes on the left panel and the magnitude-distance distribution of the recordings on the right panel for each station. Azimuthal distribution of the earthquakes around each station is generally uniform, except for the Muğla and Elazig-Malatya groups. For the Elazığ-Malatya group, a clear azimuthal pattern showing the earthquakes occurring on East Anatolian Fault Zone is visible. The majority of the earthquakes recorded by the stations in the Bodrum-Muğla group is located on the south of the stations. Almost for each station, the number of recordings reduces significantly for R_{epi}>100 km at small magnitudes, indicating censoring issues. Censoring can occur when there are missing recordings (not triggered or not above the noise level) that would have shown lower ground motions than the recorded ground motions (Abrahamson and Gülerce, 2020), and it results in a possible bias towards larger ground motions at large distances. Some of the stations (e.g., Station ID# 0707, 0919, 0920, 2409, 3514, 4818) includes no data in the R_{epi}<30 km range; therefore, the uncertainty in the intercept of the κ-R_{epi} distribution would be significant for these stations.

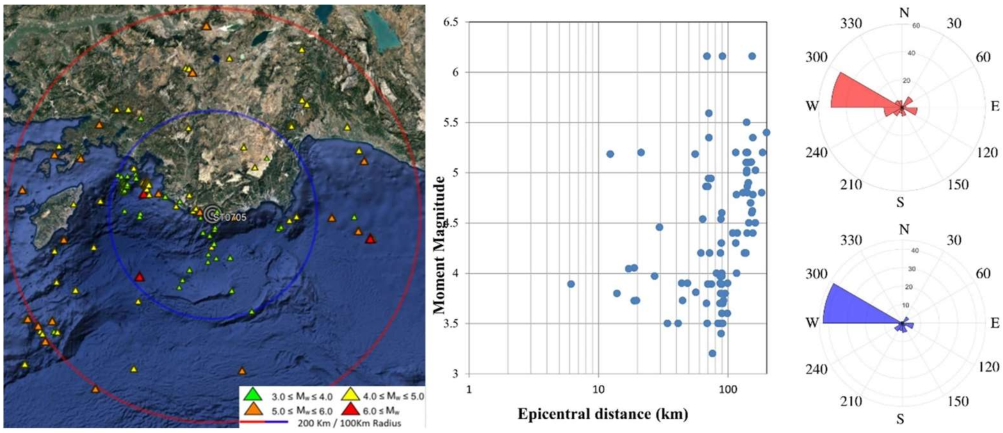

(a)

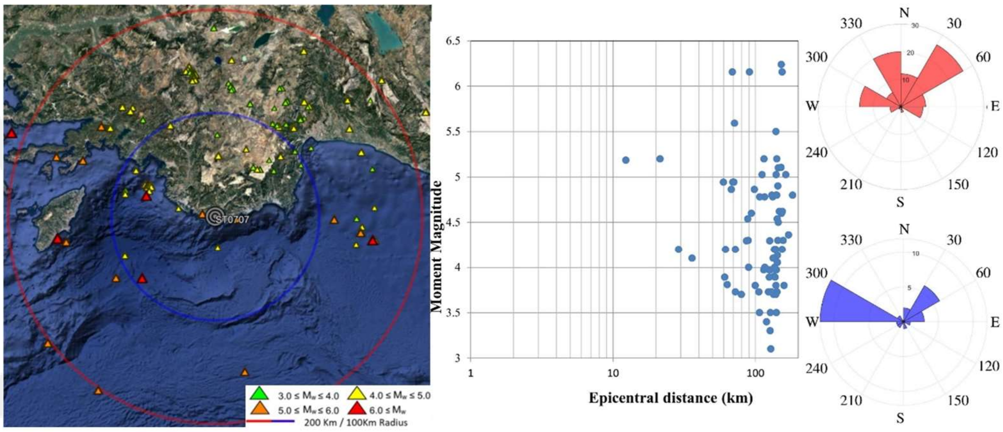

(b)

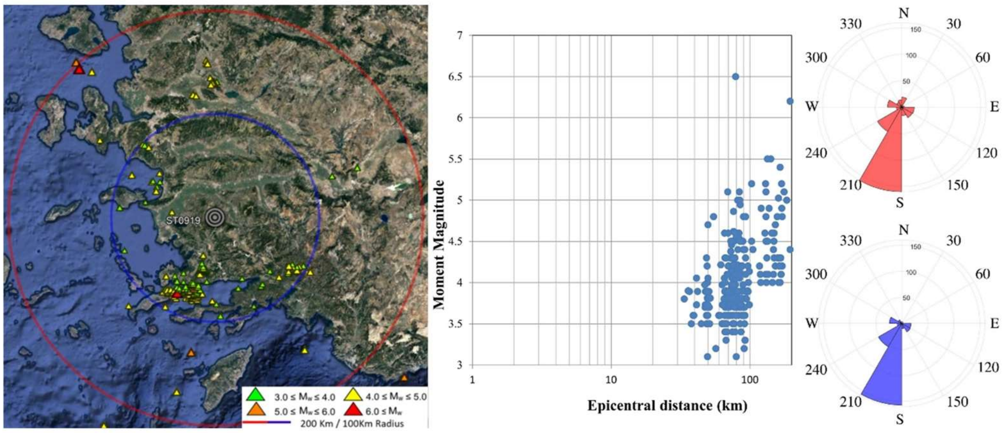

(c)

Figure 3.5. Spatial distribution of the recorded events in the right panel, M_w- R_{epi} distribution of the recordings on the middle panel, and the rose diagrams are representing azimuth for R_{epi}<200km on the top right and R_{epi}<100km on the bottom left for: (a) ST0705, (b) ST0707, (c) ST0919.

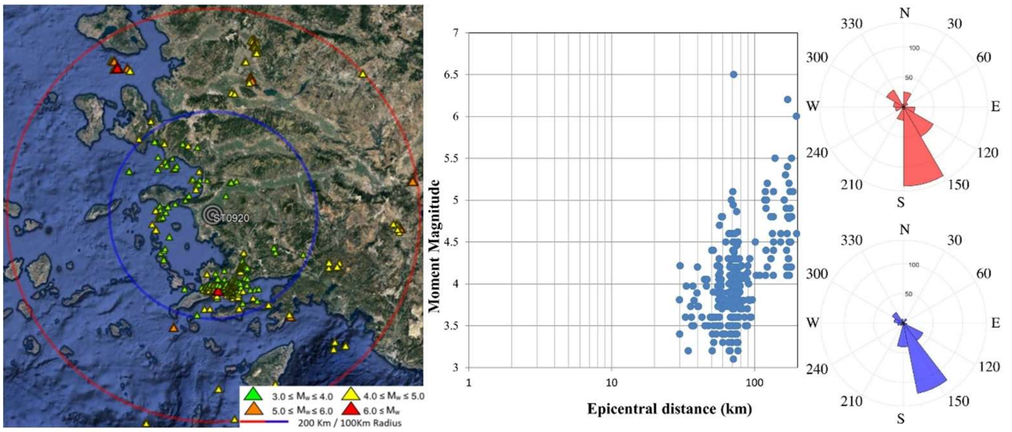

(a)

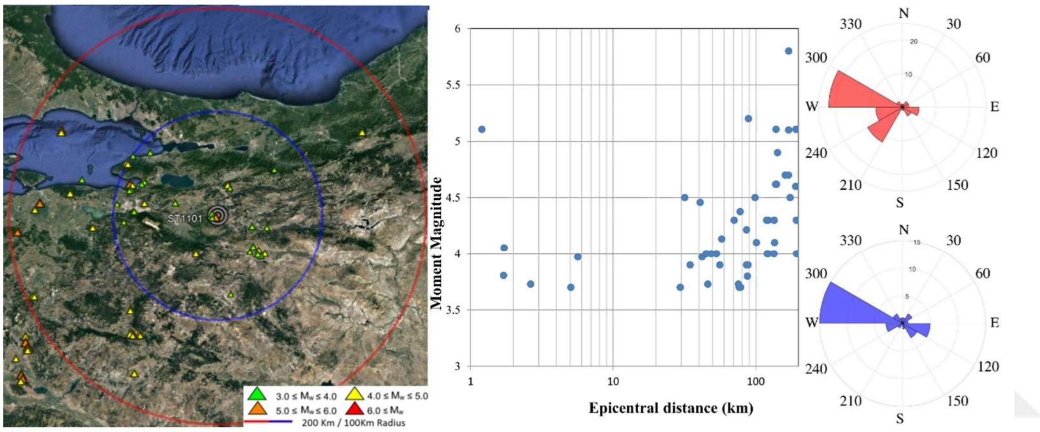

(b)

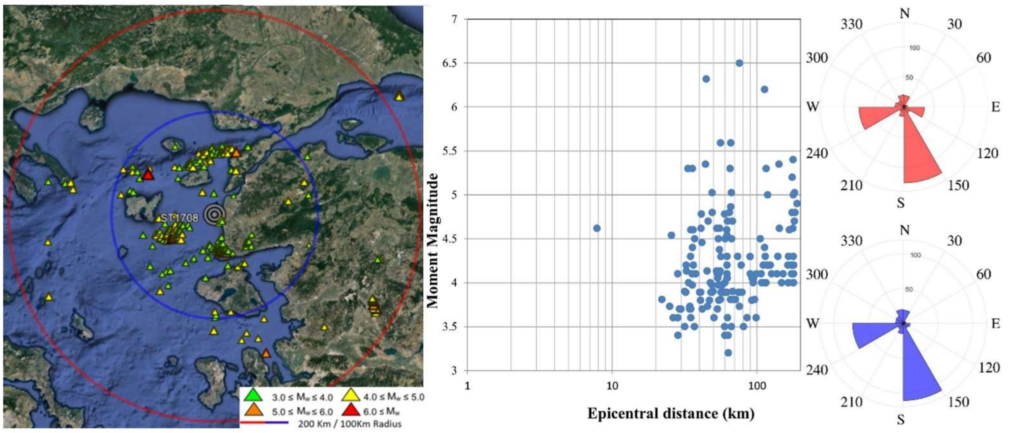

(c)

Figure 3.6. Spatial distribution of the recorded events in the right panel, M_w- R_{epi} distribution of the recordings on the middle panel, and the rose diagrams are representing azimuth for R_{epi}<200km on the top right and R_{epi}<100km on the bottom left for: (a) ST0920, (b) ST1101, (c) ST1708.

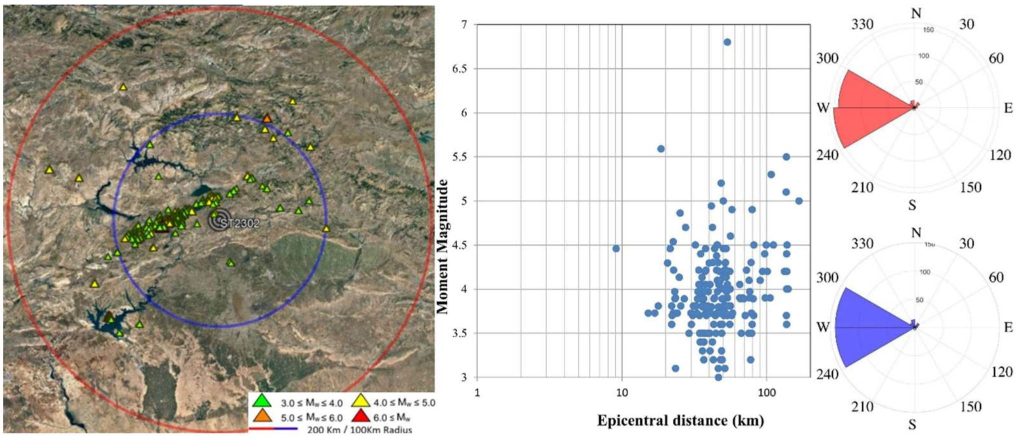

(a)

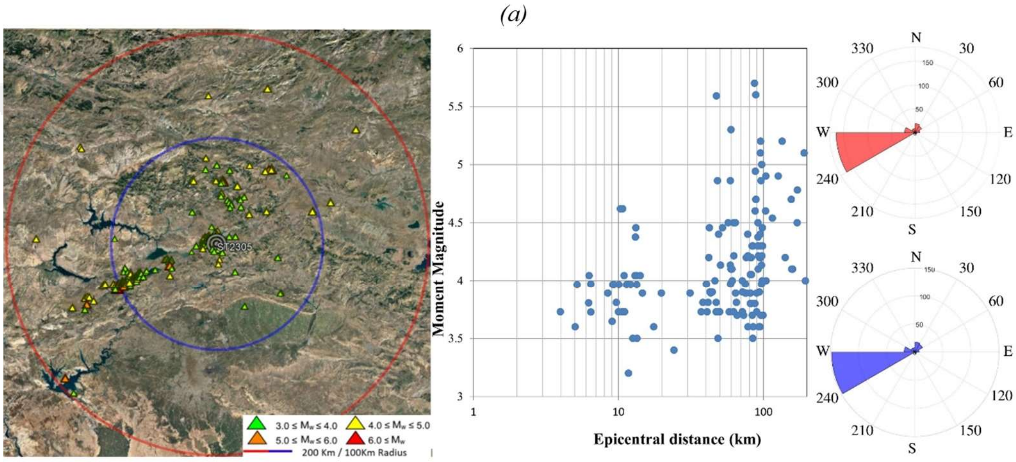

(b)

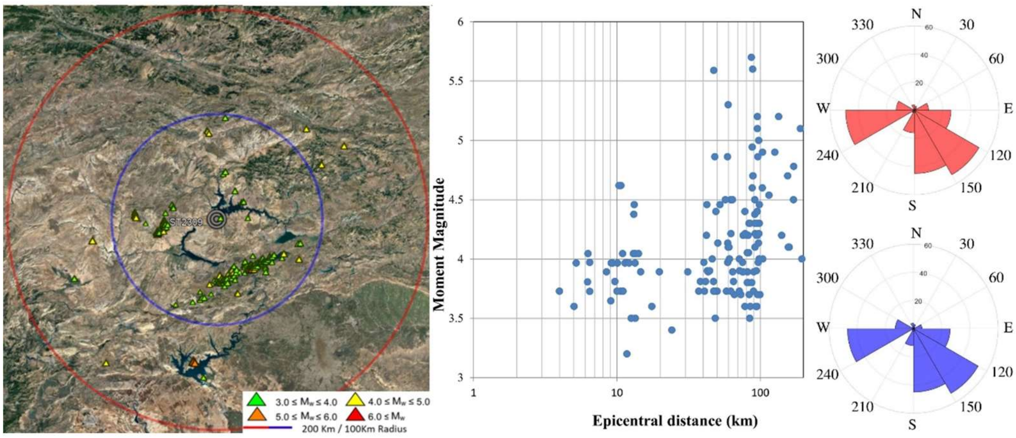

(c)

Figure 3.7. Spatial distribution of the recorded events in the right panel, M_w- R_{epi} distribution of the recordings on the middle panel, and the rose diagrams are representing azimuth for R_{epi}<200km on the top right and R_{epi}<100km on the bottom left for: (a) ST2302, (b) ST2305, (c) ST2309.

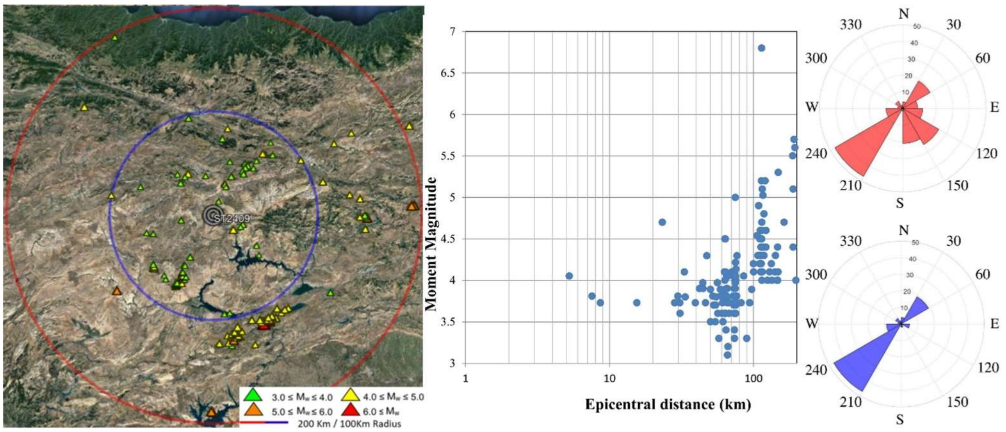

(a)

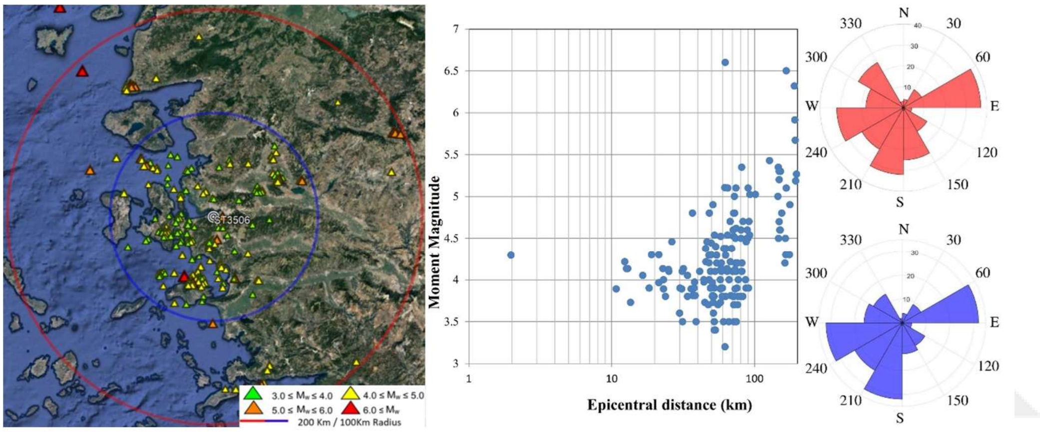

(b)

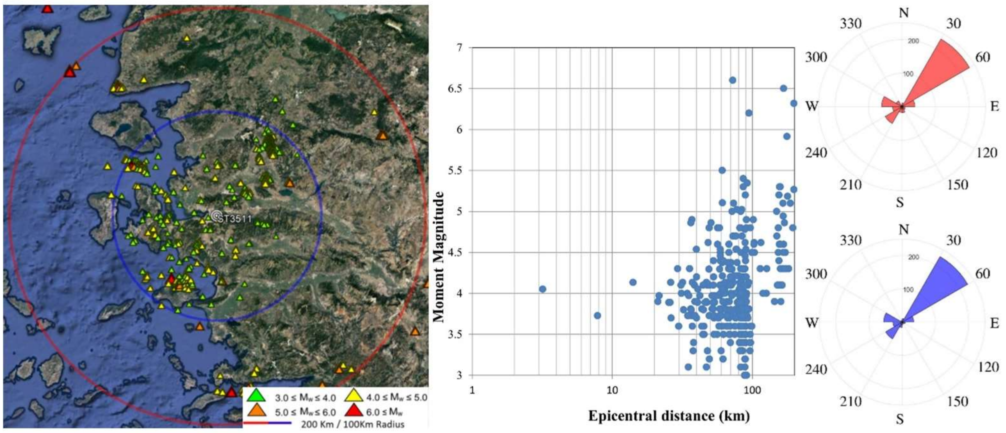

(c)

Figure 3.8. Spatial distribution of the recorded events in the right panel, M_w- R_{epi} distribution of the recordings on the middle panel, and the rose diagrams are representing azimuth for R_{epi}<200km on the top right and R_{epi}<100km on the bottom left for: (a) ST2409, (b) ST3506, (c) ST3511.

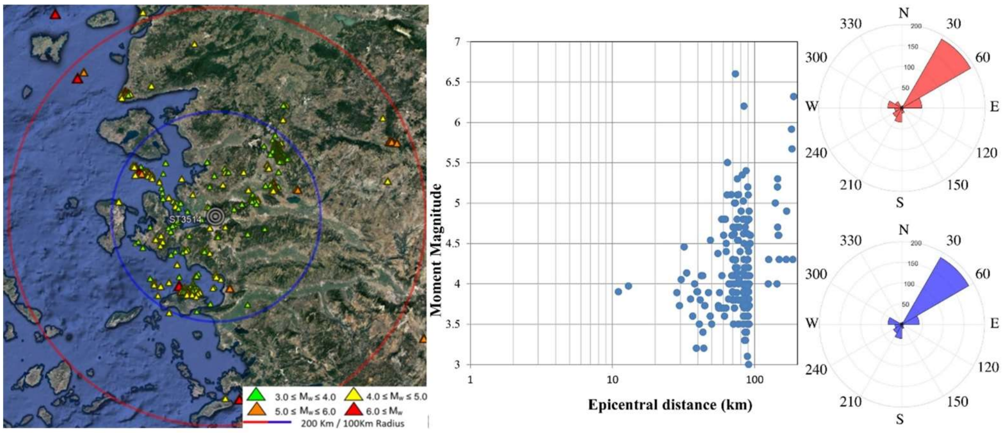

(a)

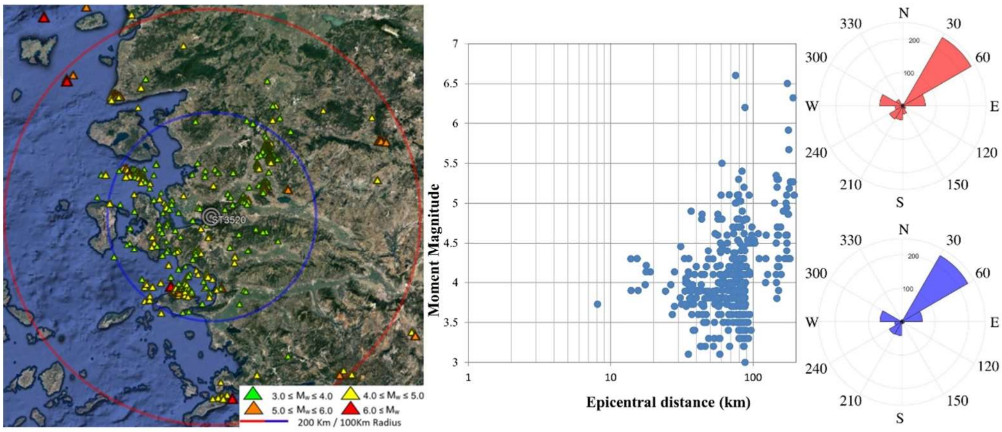

(b)

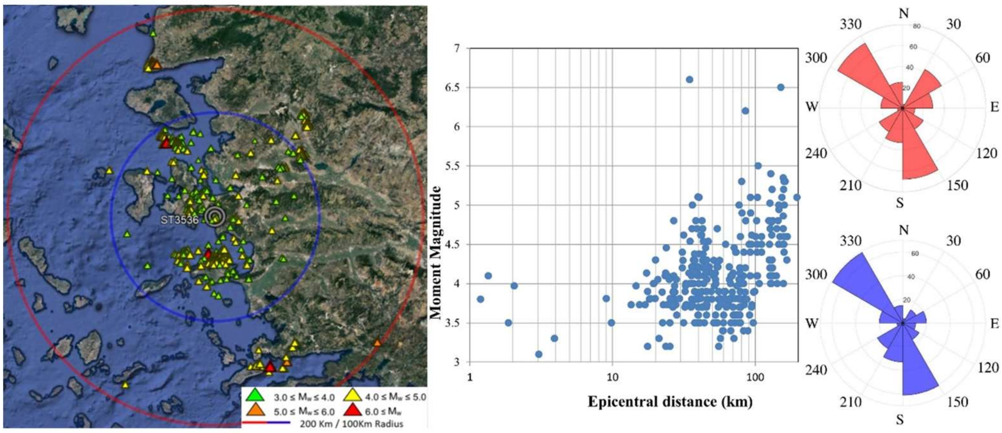

(c)

Figure 3.9. Spatial distribution of the recorded events in the right panel, M_w- R_{epi} distribution of the recordings on the middle panel, and the rose diagrams are representing azimuth for R_{epi}<200km on the top right and R_{epi}<100km on the bottom left for: (a) ST3514, (b) ST3520, (c) ST3536.

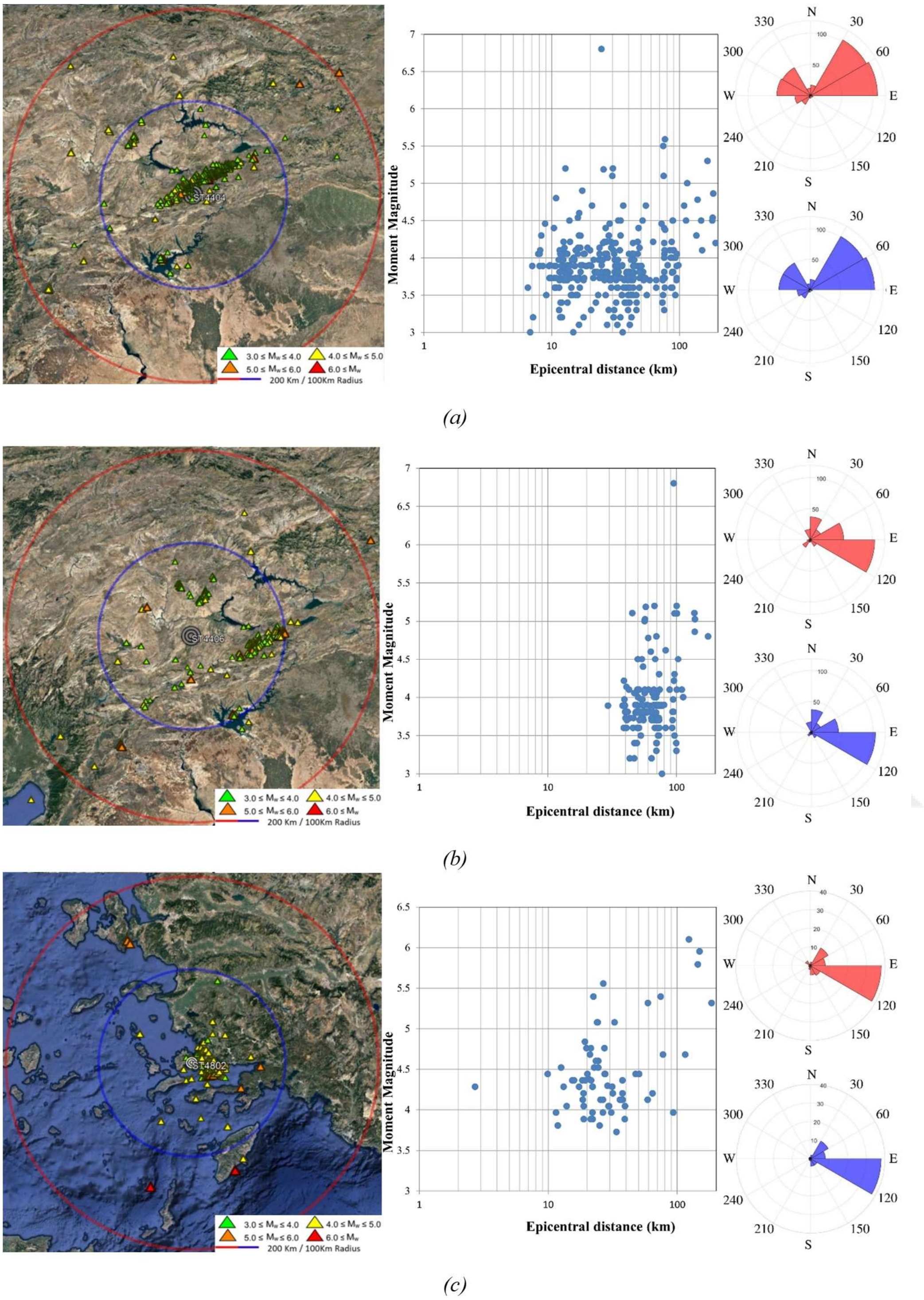

Figure 3.10. Spatial distribution of the recorded events in the right panel, M_w- R_{epi} distribution of the recordings on the middle panel, and the rose diagrams are representing azimuth for R_{epi}<200km on the top right and R_{epi}<100km on the bottom left for: (a) ST4404, (b) ST4406, (c) ST4802.

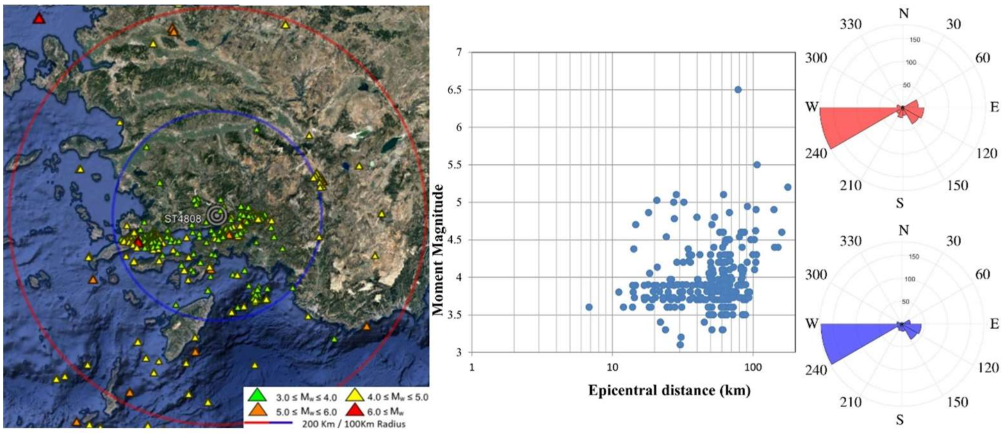

(a)

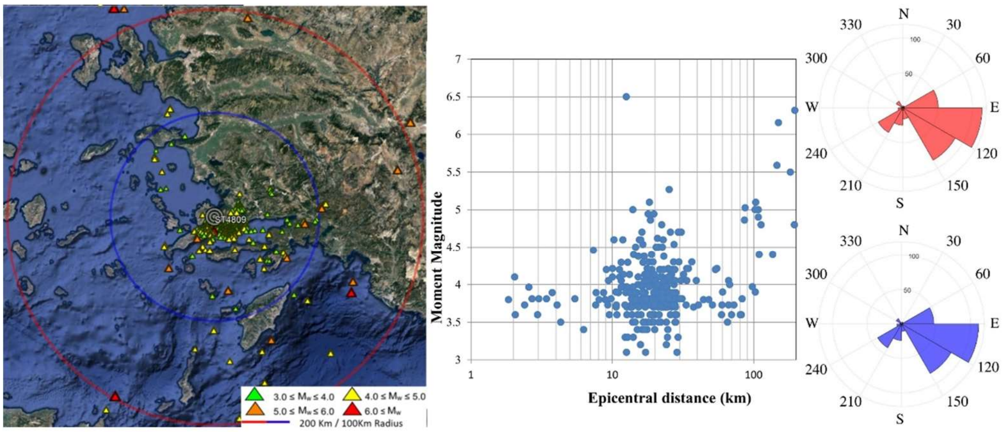

(b)

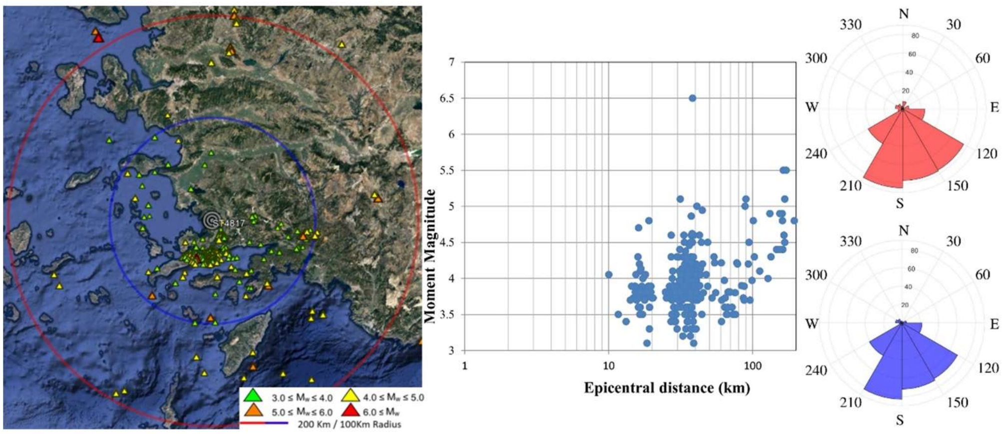

(c)

Figure 3.11. Spatial distribution of the recorded events in the right panel, M_w- R_{epi} distribution of the recordings on the middle panel, and the rose diagrams are representing azimuth for R_{epi}<200km on the top right and R_{epi}<100km on the bottom left for: (a) ST4808, (b) ST4809, (c) ST4817.

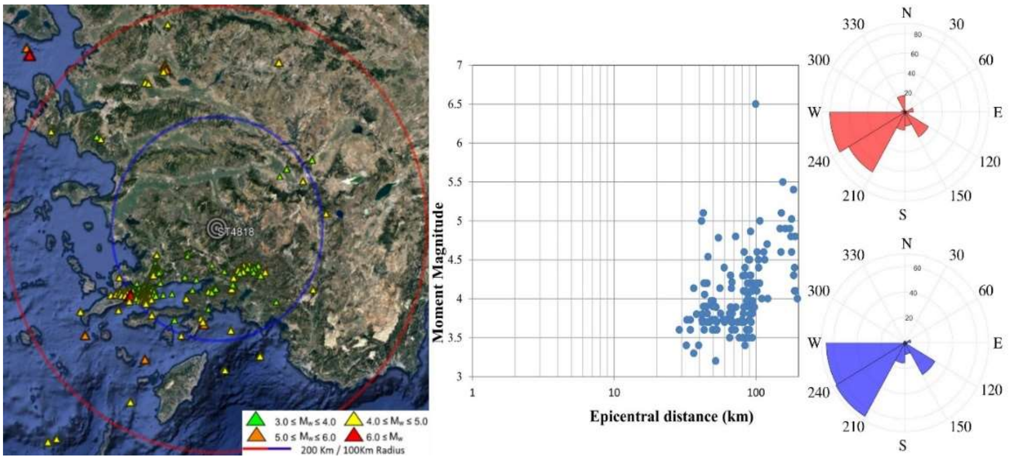

Figure 3.12. Spatial distribution of the recorded events in the right panel, Mw- Repi distribution of the recordings on the middle panel, and the rose diagrams are representing azimuth for Repi<200km on the top right and Repi<100km on the bottom left for ST4818

One of the most important features of the compiled dataset is the V_s profiles of the recording stations. In terms of the estimation of Vs profiles, the recording stations may be classified into three categories:

I. The Vs profiles of ST0705 (Antalya-Kaş), ST0707 (Antalya-Kaş), and ST1718 (Çanakkale) are not available (or not open to the public yet), even if the V_{S30} values of these stations are provided in (https://tadas.afad.gov.tr/).

II. Measurement of shear wave velocity profiles for stations ST1101, ST2302, ST3506, ST4404, ST4802, and ST4809 had done by MASW (Multi-Channel Analysis of Surface Waves Surveys) method by under the cooperation of AFAD and METU Earthquake Engineering Research Center under a Scientific and Technological Research Council of Turkey (TUBITAK) project during 2005-2007.

III. The Vs profiles of ST0919, ST0920, ST1708, ST2305, ST2309, ST2409, ST3536, ST4406, ST4808, ST4817, and ST4818 have been measured using MASW for the first 30 meters and by RE-MI (Reflection

Microtremor) method down to varying depths by the cooperation of AFAD and Kocaeli University Geophysical Department during 2015-2016. For this study, the V_s profiles obtained by the MASW are utilized for consistency with the second group. Additionally, the Vs profiles obtained by RE-MI do not reach 30 meters depth at some of the stations.

It should be noted that there are significant differences in the Vs profiles estimated by MASW and Re-Mi for the third group of stations. Variation of Vs with depth for the stations in the database is shown in Figure 3.13 for Elazığ-Malatya and İzmir stations and given in Figure 3.14 for Muğla, Aydın, and Bilecik stations, respectively. Some of the Vs profiles are quite uniform (e.g., ST3514, ST4808), or the Vs value increases with depth as expected (e.g., ST3511). However, there are significant Vs reversals in the majority of the measured Vs profiles, especially at the top 5 meters. In some of the stations, the Vs variations are quite high (e.g., ST3506, ST4818, ST1101), and the effect of site amplification and damping on the estimated high-frequency attenuation would be significant for these stations.

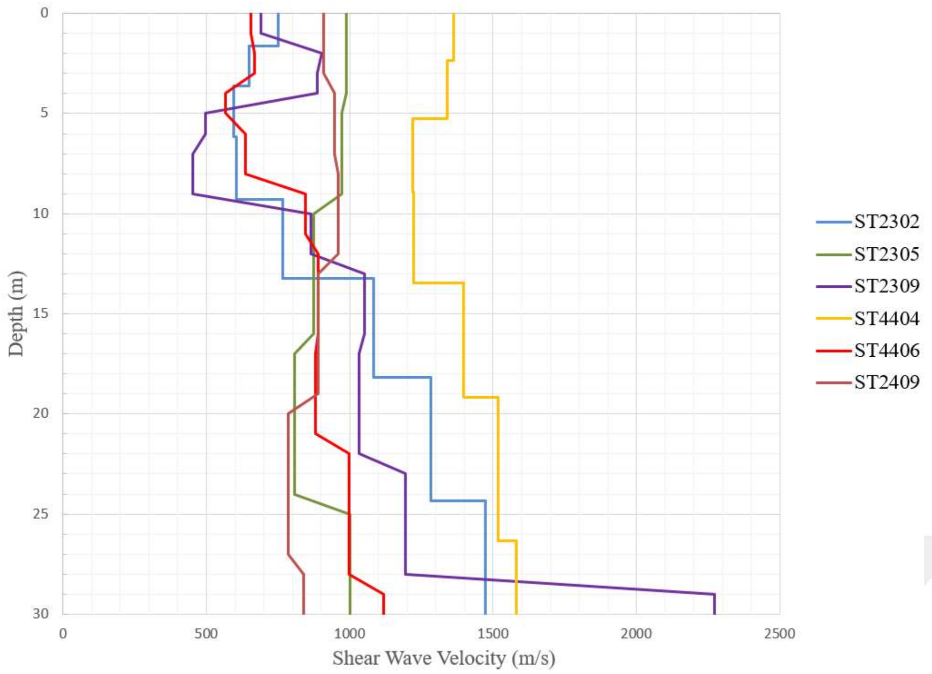

(a)

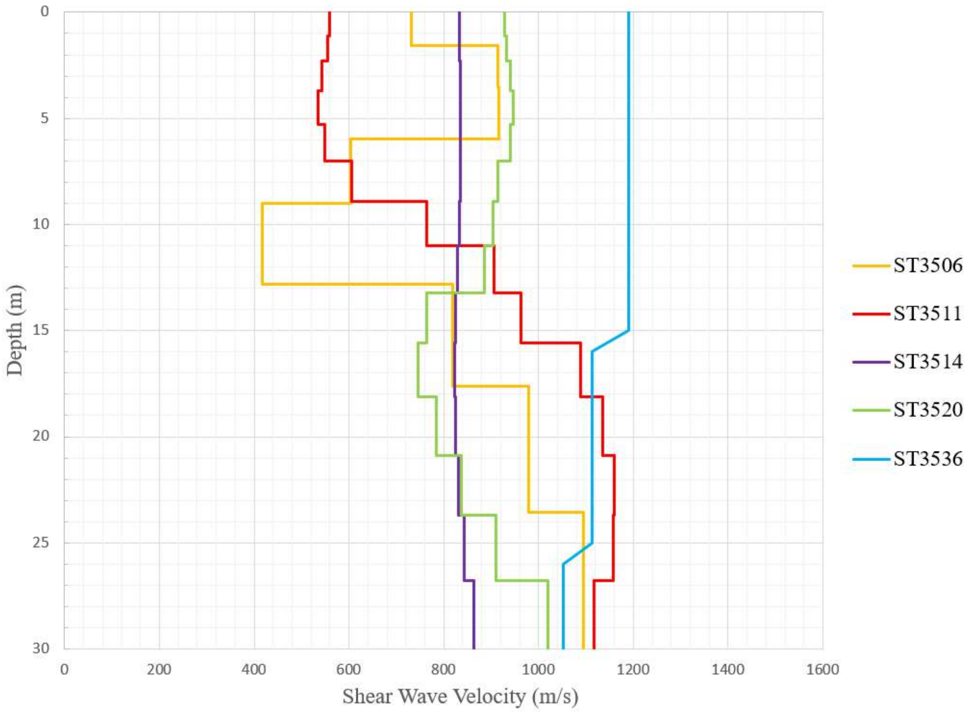

(b)

Figure 3.13. V_S Profiles for: (a) Elazığ-Malatya Stations (b) İzmir Stations.

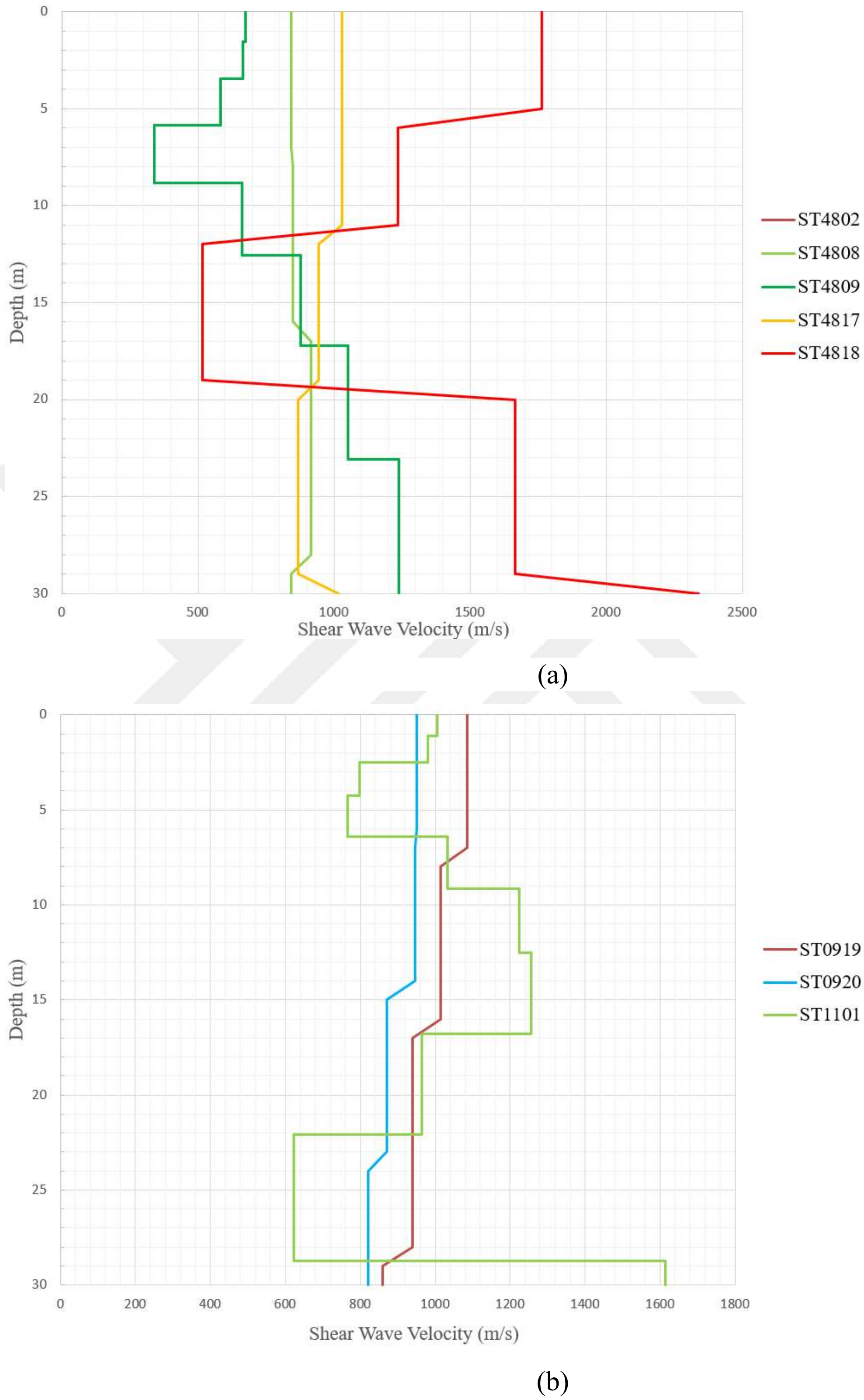

Figure 3.14. V_S Profiles for: (a) Muğla Stations (b) Aydın and Bilecik Stations.

3.2 Methodology for Estimating the High-Frequency Attenuation Parameter

Figure 3.15 provides the flow chart that summarizes the procedure used in this study for the estimation of the high-frequency attenuation parameter.

Step 1 (selecting the strong motion stations, a compilation of the ground motion database by obtaining the unprocessed recordings from https://tadas.afad.gov.tr/ and unification of the magnitude scales) is already explained in Section 3.1. The rest of the procedure is explained step-by-step below.

Step 2: After the unprocessed recordings are obtained, the waveform data is checked for data quality and the non-standard errors (Douglas, 2003) such as spike, insufficient digitizer resolution, multi-event or S-wave trigger problems. Due to the quality of the recording equipment deployed in selected stations, errors such as a spike or insufficient resolution were not observed; however, some of the small magnitude recordings include traces of multiple events, as shown in Figure 3.16. Eight hundred thirty-four recordings are excluded from the database.

After this manual data-quality check, the remaining waveforms (provided in ASCII format by AFAD) were converted to SAC format using a file-type conversion routine. Three components (N-S, E-W, and Z) of each recording was synched and treated with a Butterworth filter to bandpass the accelerograms between 0.1 and 20Hz in Seismic Analysis Code (SAC). The filtering is applied to make the P-wave and S-wave arrival times more visible; however, unfiltered waveforms are used in estimating the kappa values.

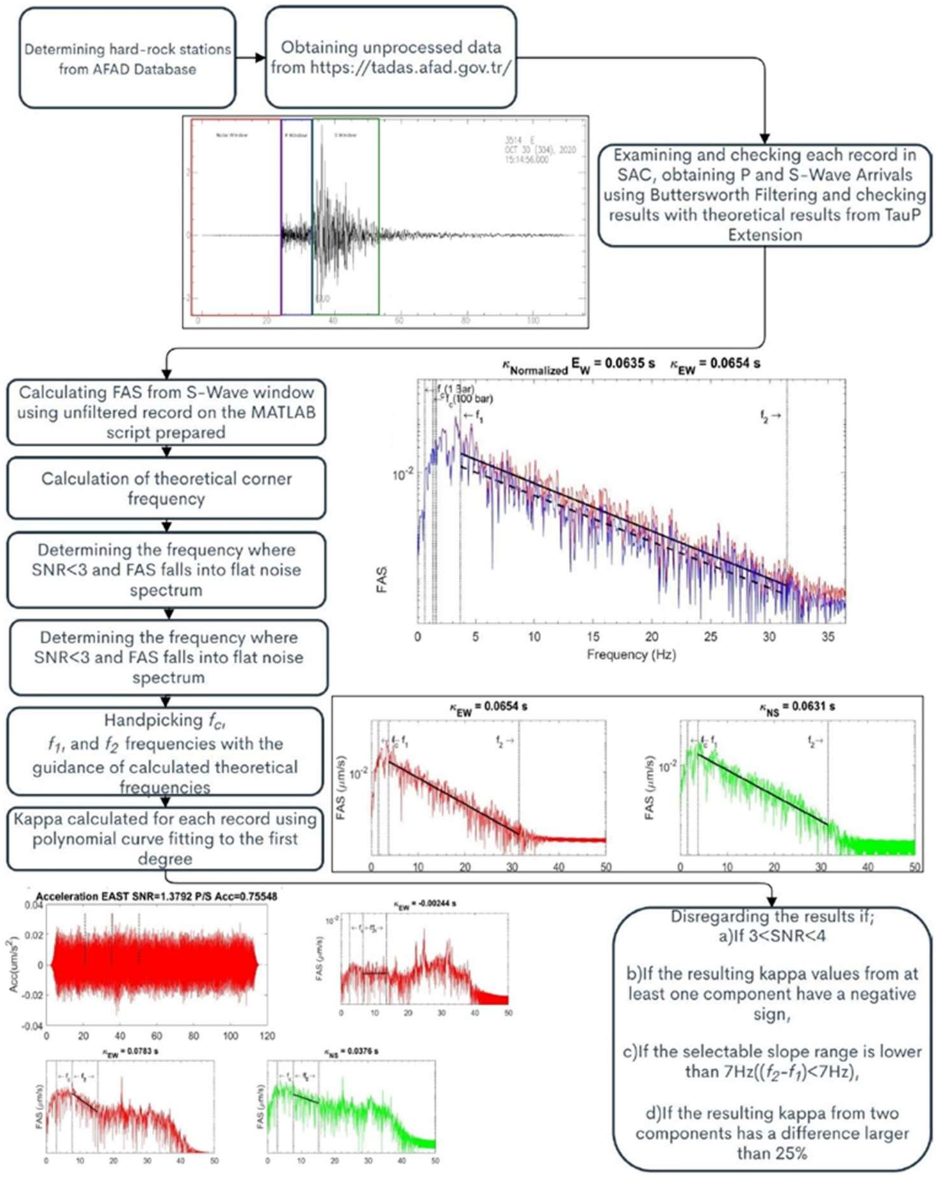

Figure 3.15. Flowchart of the process applied for estimating kappa

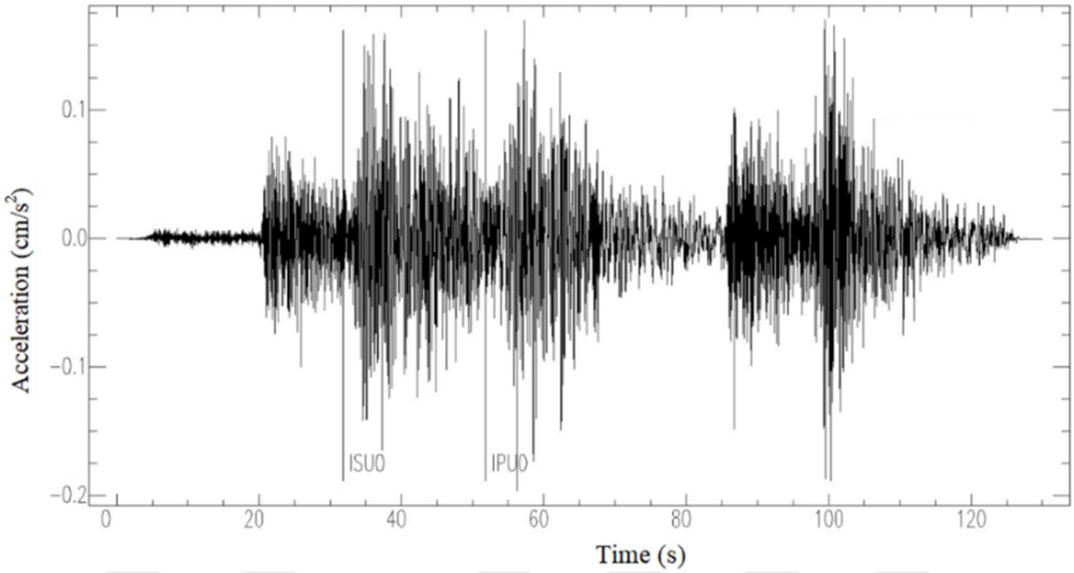

Figure 3.16. An example waveform that contains the traces from multiple events

Step 3: SAC extensions named as "TauP" based on the method proposed by Buland and Chapman (1983) and "*ttimes*" proposed by Kennet and Engdahl (1991) were used to estimate the travel times for specified P and S phases through the crustal model. However, the P-wave arrival time and the S-wave window for each recording are handpicked with the guidance of these estimations.

Selected time windows (as shown in Figure 3.17) were transferred to the flat-file created for each station. Tsai and Chen (2000) claimed that the S-window length has very little impact on the determination of kappa as long as the most energetic part of S-waves is included in it. Therefore, the end of the S-wave window is also selected manually for each recording. After the pre-event, P-wave, and S-wave windows are selected, the signal to noise ratio (SNR) of the recordings are calculated, and a total of 436 recordings with SNR<3 is eliminated from the database.

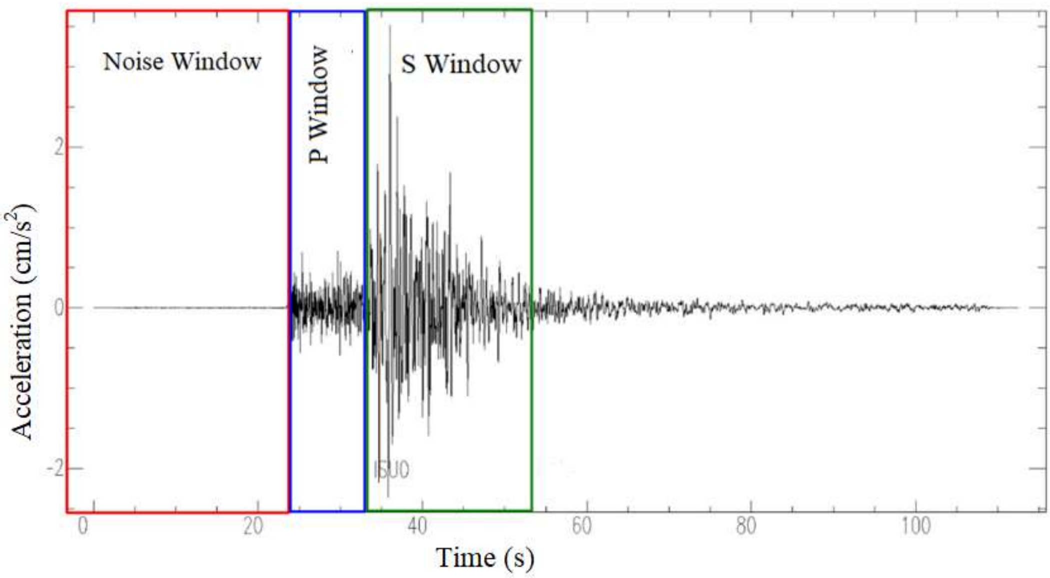

Figure 3.17. Selection of the time windows in SAC

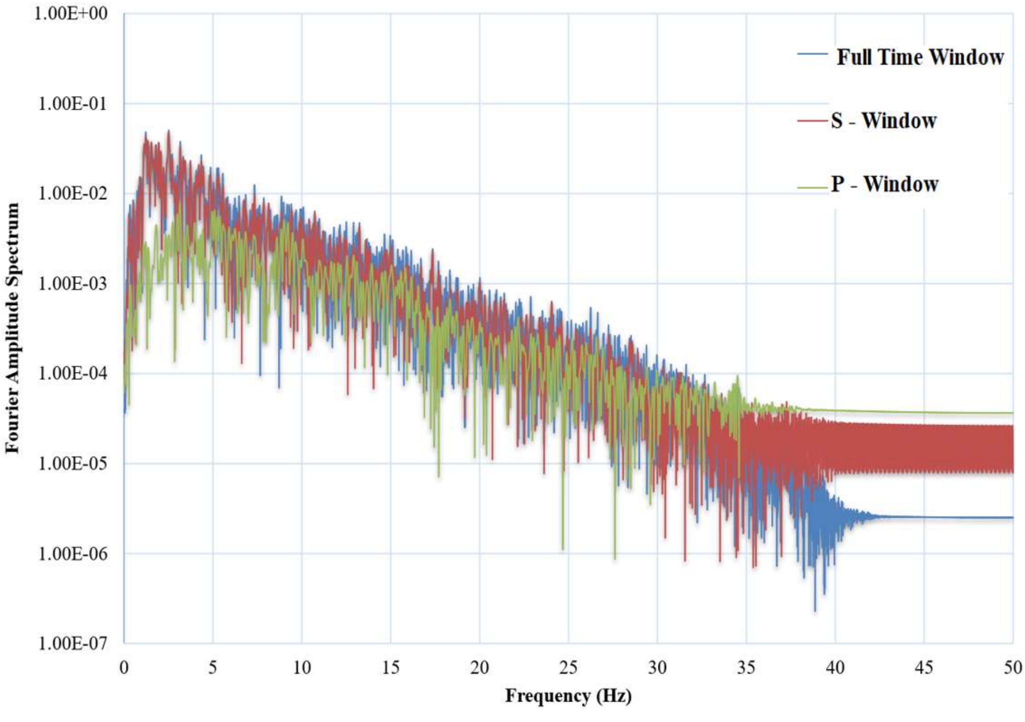

Figure 3.18. A sample of the FAS calculated for the S-window in MATLAB Software Package

Step 4: The MATLAB software package routine developed by Stanko (2017) is used after modifying and improving it to complete the kappa calculation process. The FAS in the P-wave window, S-wave window, and the pre-event window are calculated using the unfiltered recordings (Figure 3.18) using this MATLAB routine. The distribution of the SNR with frequency is plotted for two orthogonal components of each record, as shown in Figure 3.19(a).

Step 5: In this step, the frequency range (f_2-f_1), over which the slope of the high-frequency decay will be calculated, is selected for each recording. Because the high-frequency decay is observed for, the theoretical values of the corner frequency for appropriate stress drop values have been calculated to guide the selection process using the formulas below:

$$M_0 = 10^{(1.5\ x\ M_w + 1\ \ .05)} \tag{3.4}$$

$$f_c = (4.9\ x\ 10^6)x\ \beta\ \mathrm{x}\ (\frac{\Delta\sigma}{M_0^{\frac{1}{3}}}) \tag{3.5}$$

Irmak et al. (2020) calculated an average stress drop of 98 bars for small-moderate earthquakes in the Marmara region of Turkey. For Western Turkey, Tanırcan et al. (2020) calculated the stress drop values for more than 360 small to moderate earthquakes ($3.0<M_w<6.0$) and found that the majority of the earthquakes have stress drops smaller than 50 bars, and a small portion of the calculated stress drop values are between 50 to 570 bars.

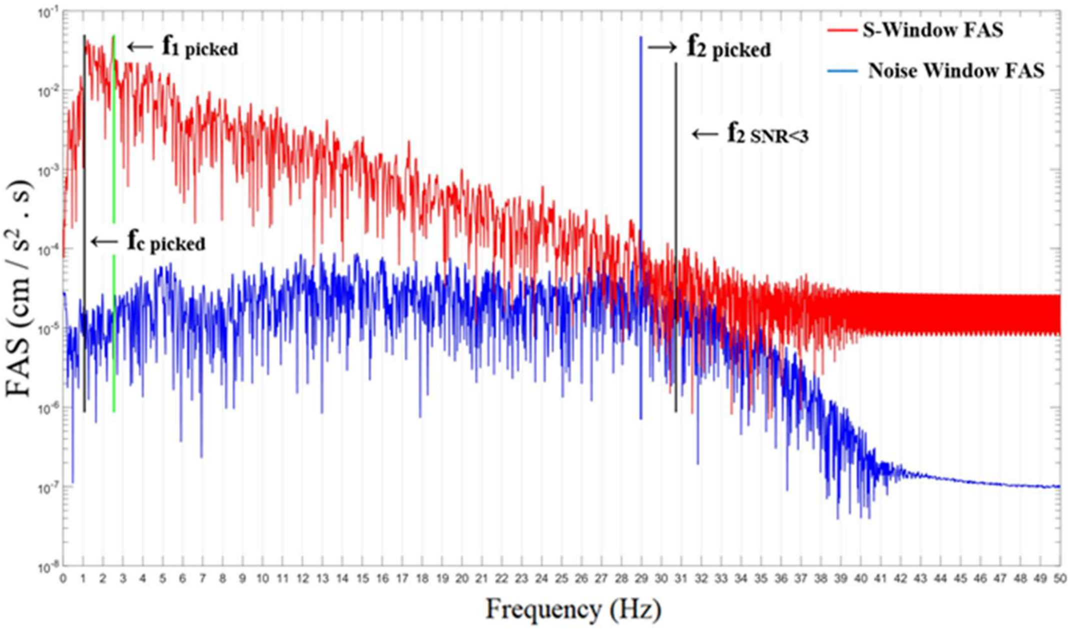

(a)

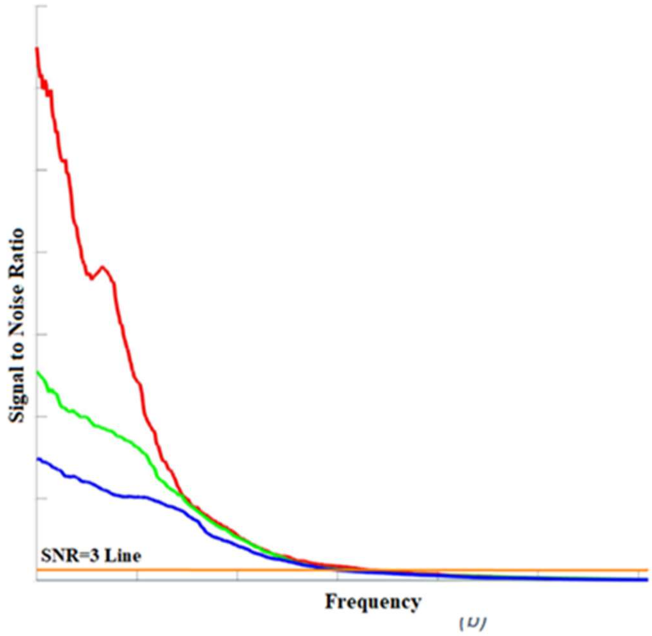

(b)

Figure 3.19. (a) MATLAB window showing the automated based on SNR and handpicked f_2 on FAS, (b) SNR calculated throughout the frequency band for each component

For this study, two different theoretical corner frequencies were calculated for $\Delta\sigma$=10 bars and $\Delta\sigma$=100 bars, while the shear-wave velocity at source (β) is taken as 3.2 km/sec. Then, the corner frequency value for the recording has been handpicked by evaluating both horizontal components for the frequency where FAS reaches a plateau (f_c, blue dots in Figure 3.20).

Selected values are generally in good agreement with the theoretical values of the corner frequency for $\Delta\sigma$=10 bars and $\Delta\sigma$=100 bars (f_{c10} and f_{c100}) as shown in Figure 3.20.

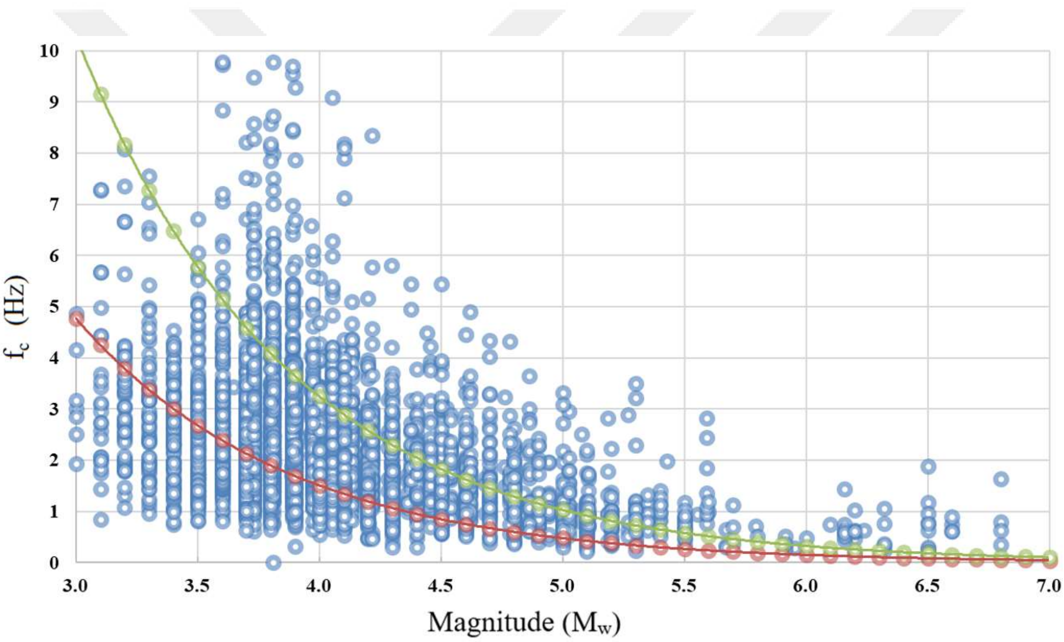

Figure 3.20. The handpicked corner frequencies for the recordings in the dataset in comparison with the theoretical corner frequencies for $\Delta\sigma$=10 bars (red) and $\Delta\sigma$=100 bars (green) (f_{c10} and f_{c100}, respectively)

The frequency value where FAS starts showing a crash syndrome (to be referred to as f_1) was handpicked, considering that. The minimum f1 value has been set to be 3Hz since the amplification on transfer functions start after 3Hz. Two guiding frequencies were calculated to help to choose the f_2 value. The first one was to find where it stops crashing (where its slope changes upwards) and falls into noise (Around 30-32Hz for Figure 3.19). FAS data has been smoothed by calculating the moving average of the data points along the FAS vector with a smoothing factor of 0.5 to obtain this value. A point has been marked as "f2Auto" on FAS windows where the slope lies between the value of 0 and -0.05. The second one was to obtain at which frequency Signal to Noise ratio falls below 3. Another point has been marked as "f2SNR" on the FAS window for this value.

Step 6: At this final step, the slope of the FAS in a semi-log plot for the selected frequency range (f_2-f_1) is estimated (λ) as shown in Figure 3.21, and the high-frequency attenuation parameter κ is estimated by Eq. 3.6. For estimating the slope, a polynomial curve fitting to the first degree has been applied using linearly spaced vectors created around selected f_1 and f_2 values.

$$\kappa = -\frac{\lambda}{\pi} \tag{3.6}$$

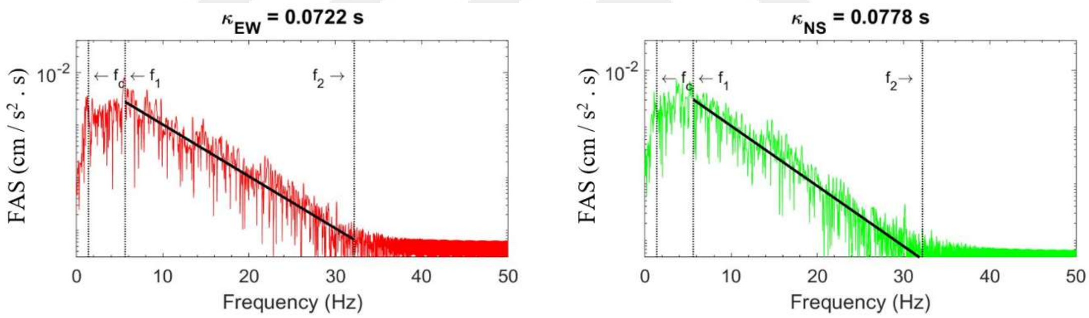

Figure 3.21. Estimation of kappa for the record on all components

For all the remaining recordings in the dataset, the kappa values are calculated for two orthogonal horizontal components using the same frequency range, as shown in Figure 3.21. An average 13.49% difference between estimated kappa values of horizontal components has been observed. After the process in MATLAB, a quality indexing has been applied to clear out data furthermore.

Step 7: Following recordings has been eliminated from the results;

a) If 3<SNR<4

b) If the resulting kappa values from at least one component have a negative sign,
c) If the selectable slope range is lower than 7Hz ((f_2-f_1) <7Hz),
d) If the resulting kappa from two components has a difference larger than a certain percentage (to be discussed in the next chapter).

After the elimination of faulty recordings and the elimination additional 821 recordings with the criteria stated above, the remaining dataset consists of 4372 three-component recordings. In Figure 3.21 and Figure 3.22, it can be seen that the distribution of the data over neither V_{S30} bins nor moment magnitude is not affected by the eliminations.

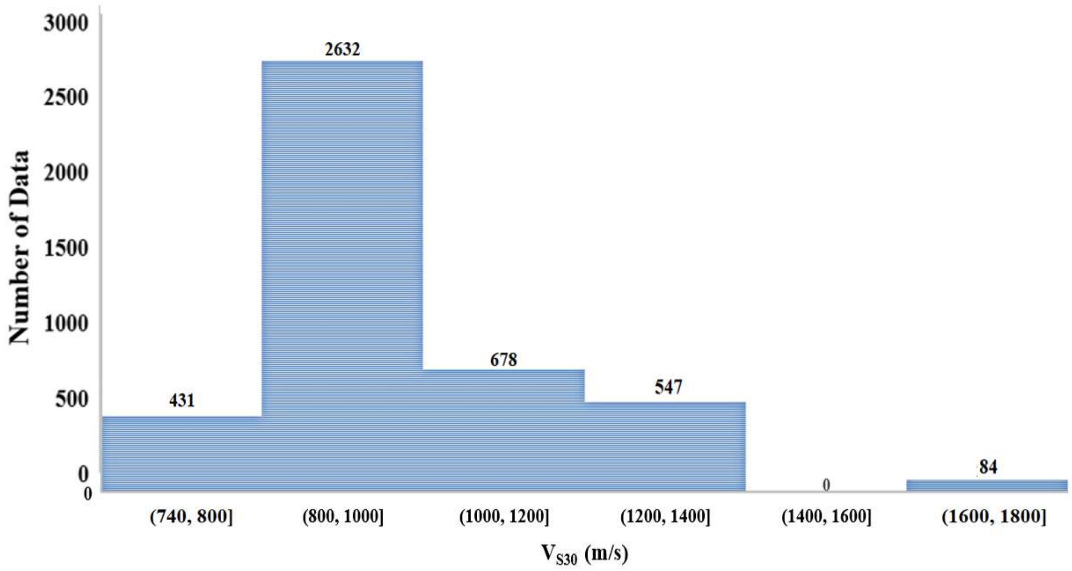

Figure 3.22. The number of recordings in the final dataset in equally spaced V_{S30} bins.

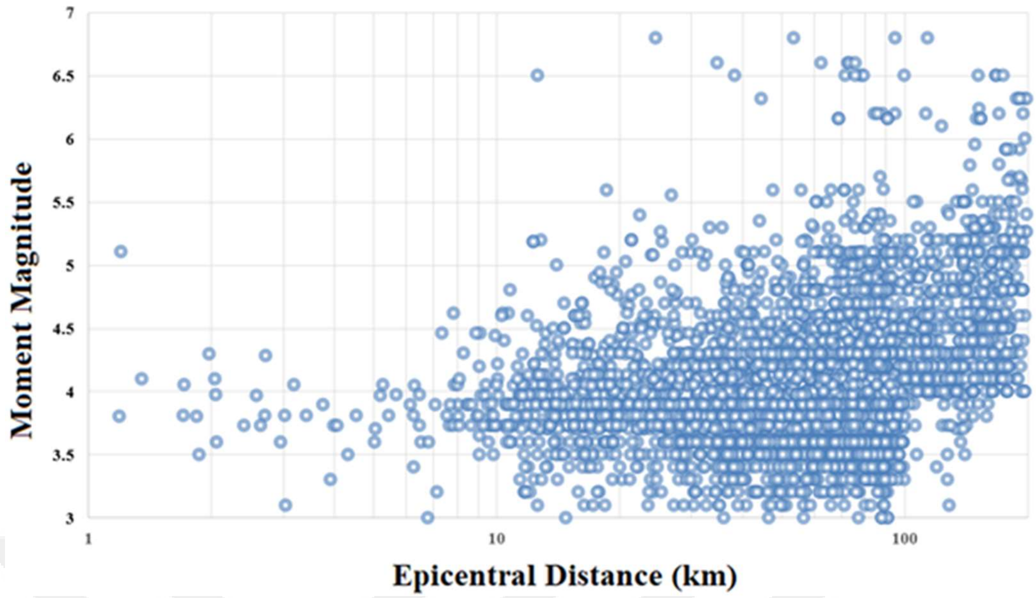

Figure 3.23. Magnitude- V_{S30} distribution of the recordings in the final dataset

Trends for selected f_{max}, f_2, and f_c values have been examined, and the distribution vs. epicentral distance and moment magnitude can be seen in Appendix A: Figures A.1 to A.8.

To avoid any source effects, f_1 values always picked higher than f_c. The distribution of f_{max} and f_2 showed a uniform correlation with magnitude and epicentral distance. However, it should be noted that the inverse relationship between the magnitude and f_{max}, and f_2 can be explained by the lack of high magnitude near-site records in our database. In an evenly distributed database, this inverse relationship is not expected.

78.9% of all f_{max} values lie between 3-10Hz, while f_2 values are nearly evenly distributed between 15-40Hz while the dominant range is 20-25Hz with a small margin. It is expected that the f_2 is related to the noise spectrum of instruments, Nyquist frequency of the most used recorder for the database of this study, Guralp CMG-5T. On the contrary, site effects dominate f_{max} (Hanks, 1982; Boore, 2003).

Figure 3.10 shows that the f_c is correlated with magnitude, where Figure 3.2 shows the correlation with the moment magnitude. Although this trend is expected (Boore, 2003), large scatter in the small magnitude earthquakes up to moderate epicentral distances (R_{epi}<60km) might be caused by the source contribution due to near-source scattering.

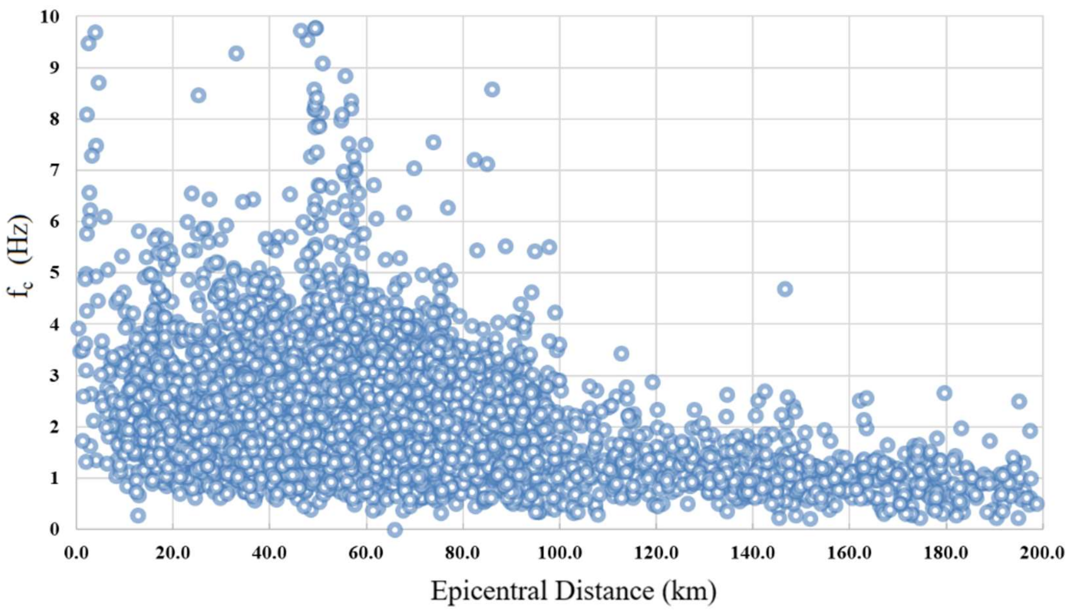

Figure 3.24. f_c vs. Epicentral Distance distribution

CHAPTER 4

DISCUSSION OF THE RESULTS

The kappa values for two orthogonal horizontal components (E-W and N-S) of 4372 recordings in the final database are obtained with the methodology described in Chapter 3. The record-specific kappa is calculated by taking the geometric mean of the kappa values of two horizontal components. Preliminary analysis of the results showed that, for some of the recordings, there are significant differences in the kappa values of two horizontal components. The percent difference between the kappa values for the same recording is calculated and added to the database. The distribution of the record-specific kappa values with epicentral distance for each station is evaluated as shown in Figure 4.1 to understand if that difference affects the results of the regression. Figure 4.1 shows the distribution of record-specific kappa values with epicentral distance for ST1708 using the full dataset (4.1(a)), using the recordings that have the percent difference smaller than 25% (4.1(b)) and 15% (4.1(c)). For most of the stations, the goodness of the fit (represented here by R^2) increases by setting the limit for the difference as 25%, which was also suggested and applied by Ktenidou et al. (2013), Ktenidou et al. (2014), Gentili & Franceschina (2011), Van Houtte et al. (2014), Stanko et al. (2018), and Biro et al. (2020). When the limit is set to 15%, the R^2 values decrease in some stations as the number of data points decreases considerably. Applying a limit smaller than 15% significantly reduces the number of recordings in each station. Based on this observation, the cut-off for the difference is set to 25% for all stations by eliminating the recordings that have a bigger difference than the limiting value.

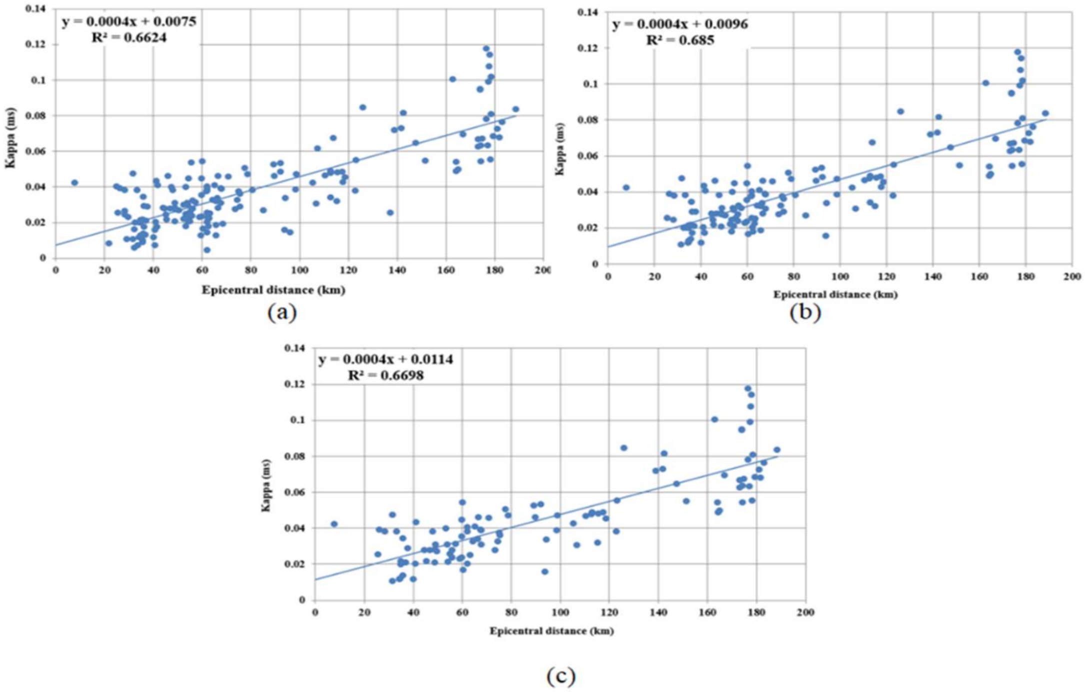

Figure 4.1. Kappa vs. epicentral distance distribution for ST1708 (a) for the full dataset, (b) when 25% difference limit is applied (c) when 15% difference limit is applied.

The distribution of record-specific kappa values with epicentral distance is plotted for

each station and presented in Figures 4.2 to 4.9. The least-square regression method is used to estimate κ_0 (the intercept of the fit or the zero-distance kappa) and κ_R (slope of the fit). In Figures 4.2 to 4.9 (left panels), median predictions are represented with black lines, and 95% confidence intervals of the median are shown with red lines. Outliers are marked with red dots and are disregarded from the regression as suggested by Ktenidou et al. (2013). Figures 4.2 to 4.9 (right panels) present the distribution of the residuals of the model with epicentral distance for each station. Van Houtte et al. (2011), Kilb et al. (2012), and Ktenidou et al. (2013) suggested that the kappa's correlation with the hypocentral distance may be stronger as this parameter represents the propagation path from source to the site better than the epicentral distance. Due to the lack of precision in focal depths of the small magnitude events, epicentral distance is preferred in this study.

Figures 4.2-4.9 shows that the expected trend in record-specific kappa values with distance is present in most of the stations, except for ST2309, ST4406, ST4808, and ST0707. In these stations, the distribution of kappa with distance is almost flat, and the R^2 value of the linear fit is quite small (<0.2). In this respect, the station-specific parameters (κ_0 and κ_R) for these stations are statistically not stable. In some of the stations (e.g., ST1101), the trend in kappa with epicentral distance is quite strong even if the number of data points is limited. On the contrary, kappa shows a weak correlation with distance in some stations (e.g., ST2302) even if the number of recordings is considerable. The residual plots show no significant bias in the model with epicentral distance, except for a couple of stations. For ST3514, ST4817, and ST4818, the residuals are negative at large distances, indicating a change in the slope for R_{epi}>100 km. In ST0920 and ST2409, residuals at short distances (R_{epi}<50 km) show negative or positive trends.

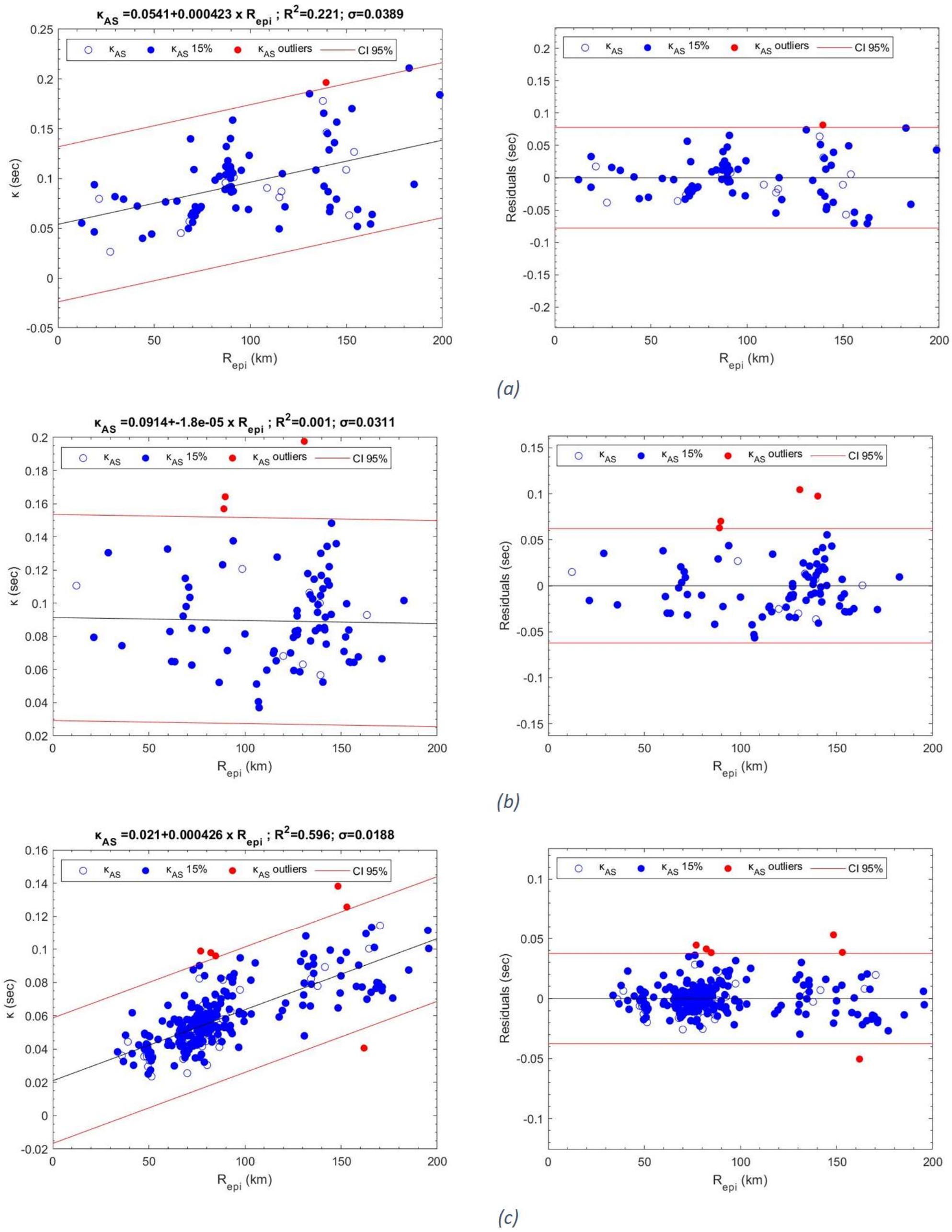

Figure 4.2. Kappa vs. epicentral distance scatter (on the left panel), Residual vs. Epicentral Distance scatter (on the right panel) for: (a) ST0705 (b) ST0707 (c) ST0919

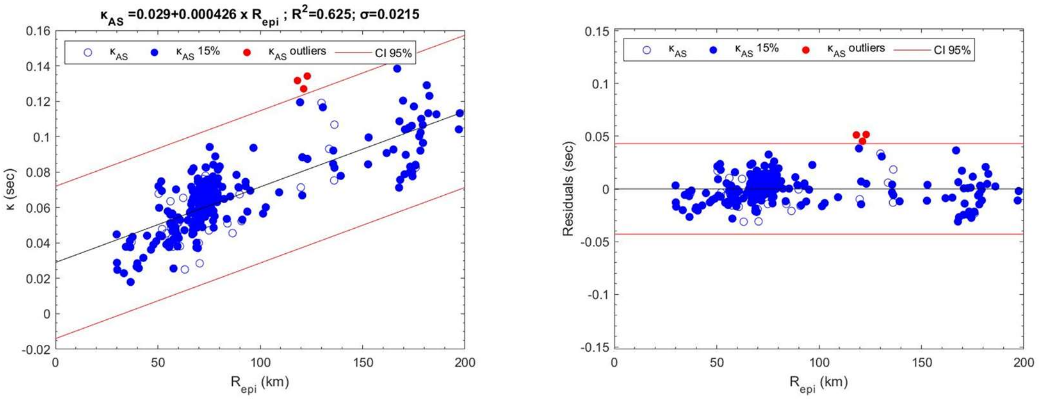

(a)

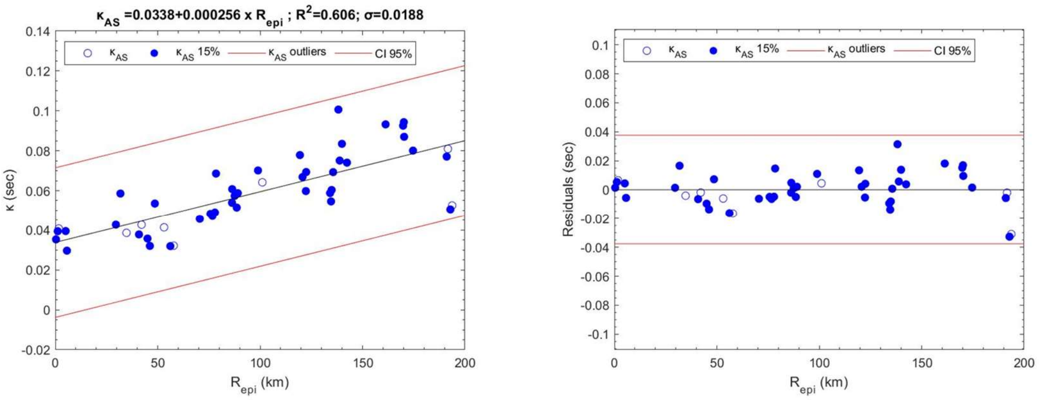

(b)

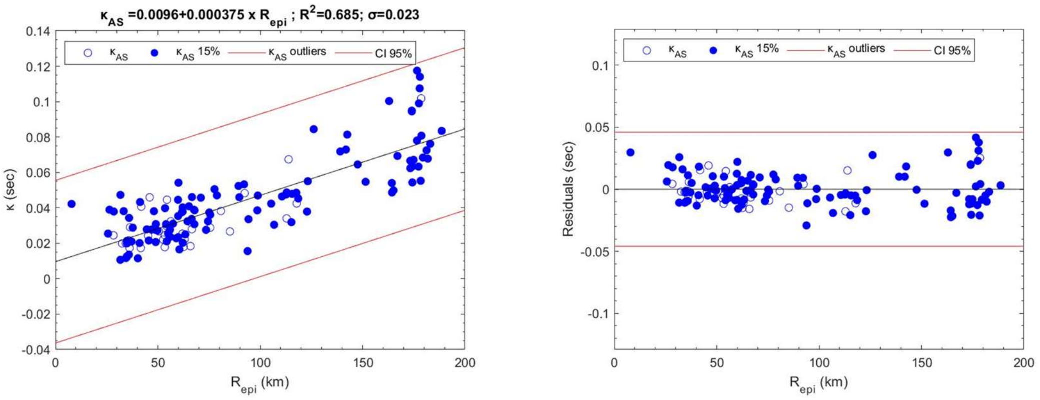

Figure 4.3. Kappa vs. Epicentral Distance scatter (on the left panel), Residual vs. Epicentral Distance scatter (on the right panel) for: (a) ST0920 (b) ST1101 (c) ST1708

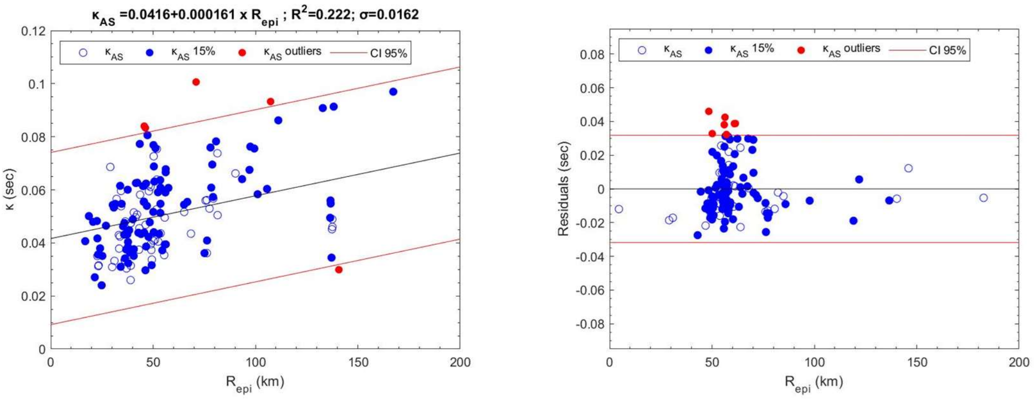

(a)

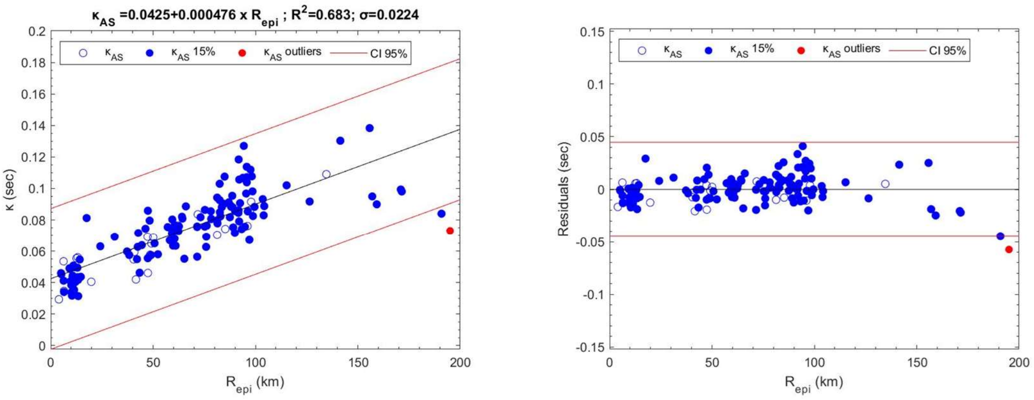

(b)

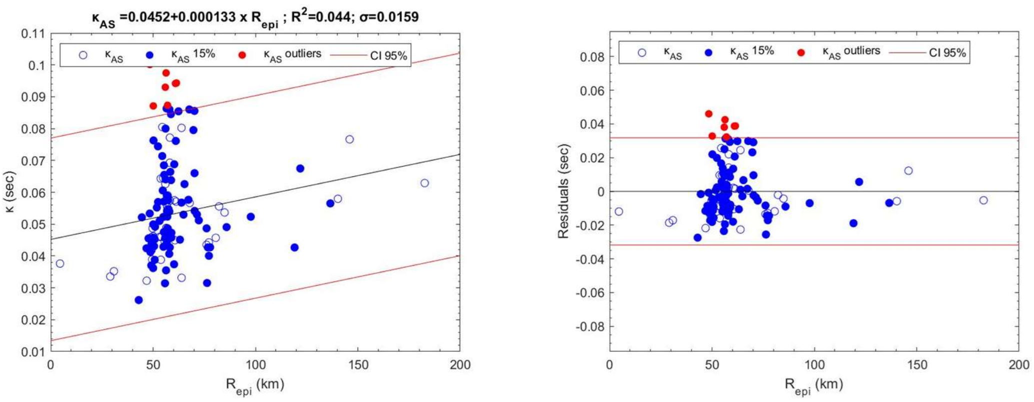

(c)

Figure 4.4. Kappa vs. Epicentral Distance scatter (on the left panel), Residual vs. Epicentral Distance scatter (on the right panel) for: (a) ST2302 (b) ST2305 (c) ST2309

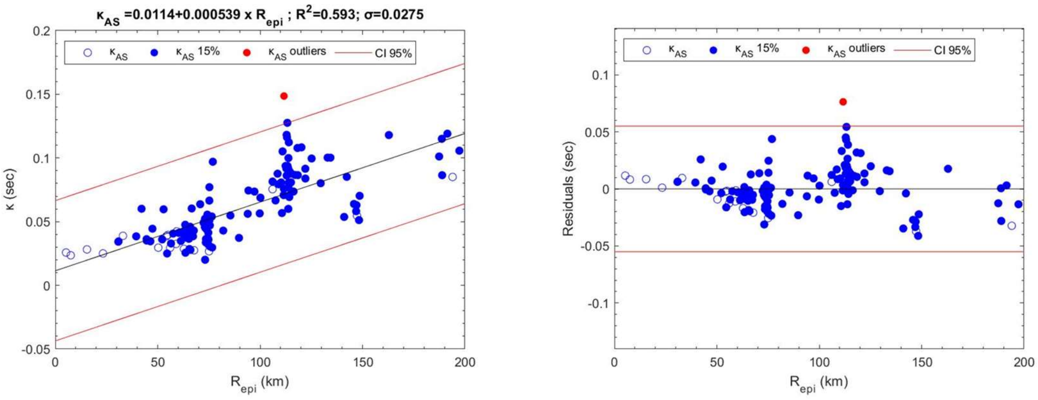

(a)

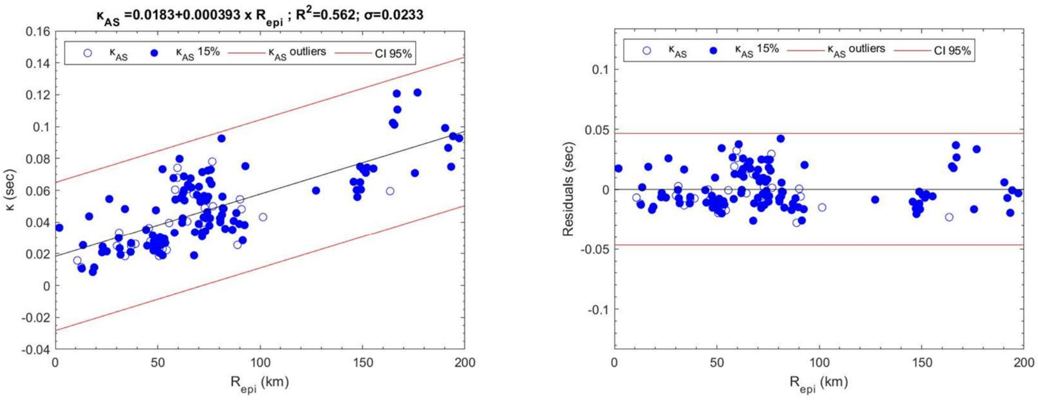

(b)

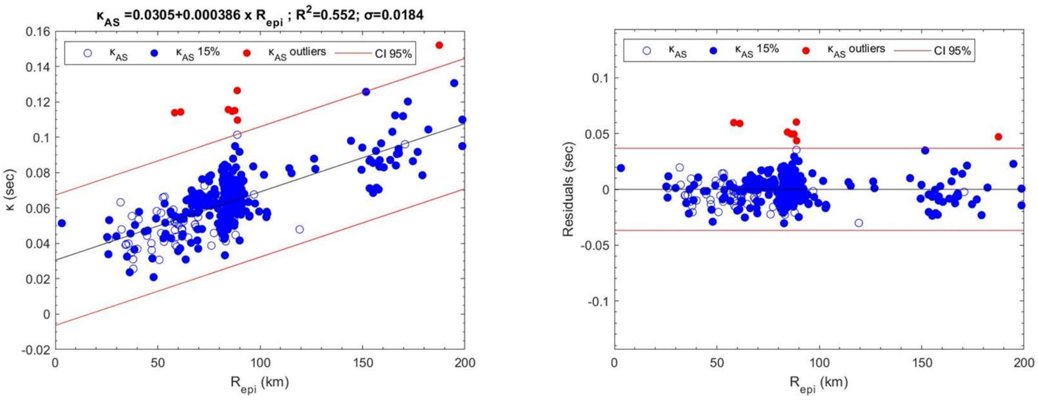

(c)

Figure 4.5. Kappa vs. Epicentral Distance scatter (on the left panel), Residual vs. Epicentral Distance scatter (on the right panel) for: (a) ST2409 (b) ST3506 (c) ST3511

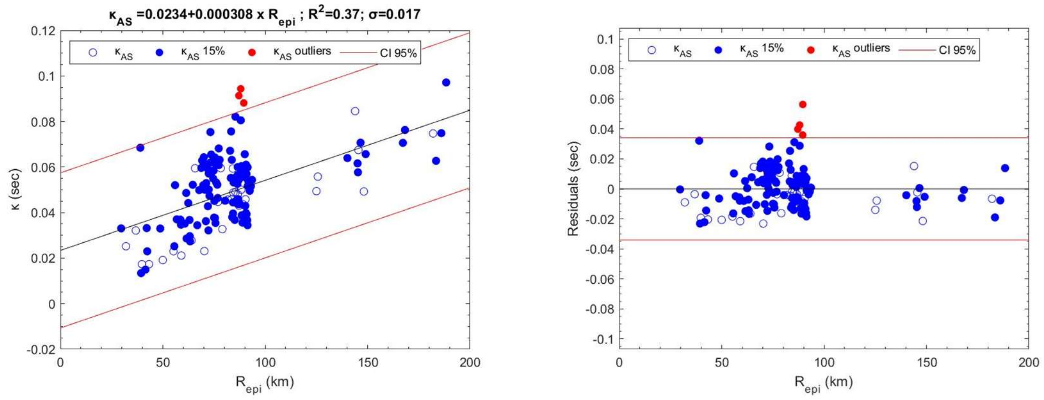

(a)

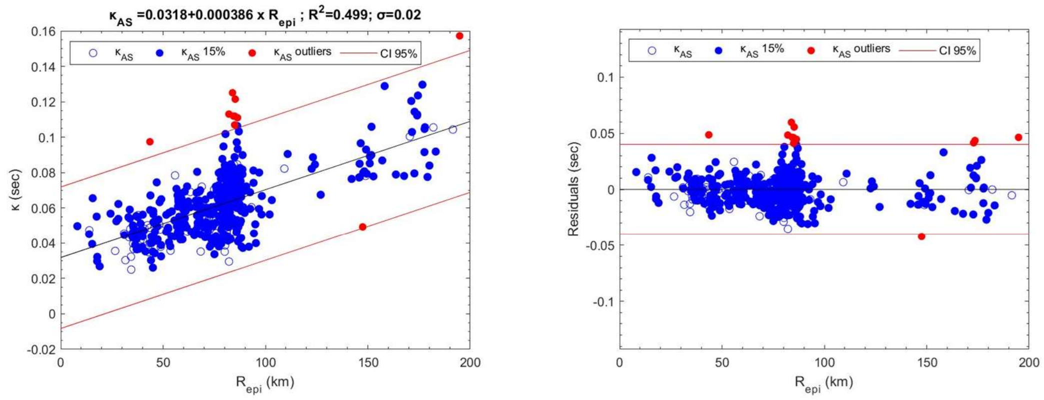

(b)

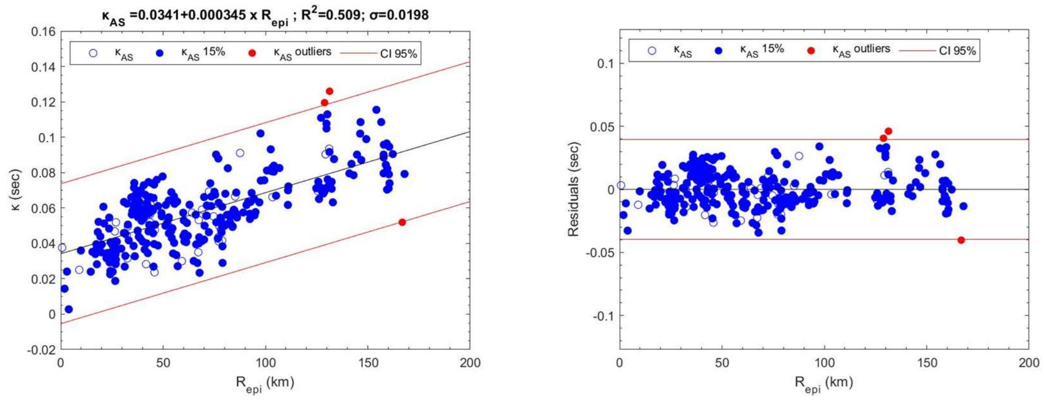

(c)

Figure 4.6. Kappa vs. Epicentral Distance scatter (on the left panel), Residual vs. Epicentral Distance scatter (on the right panel) for: (a) ST3514 (b) ST3520 (c) ST3536

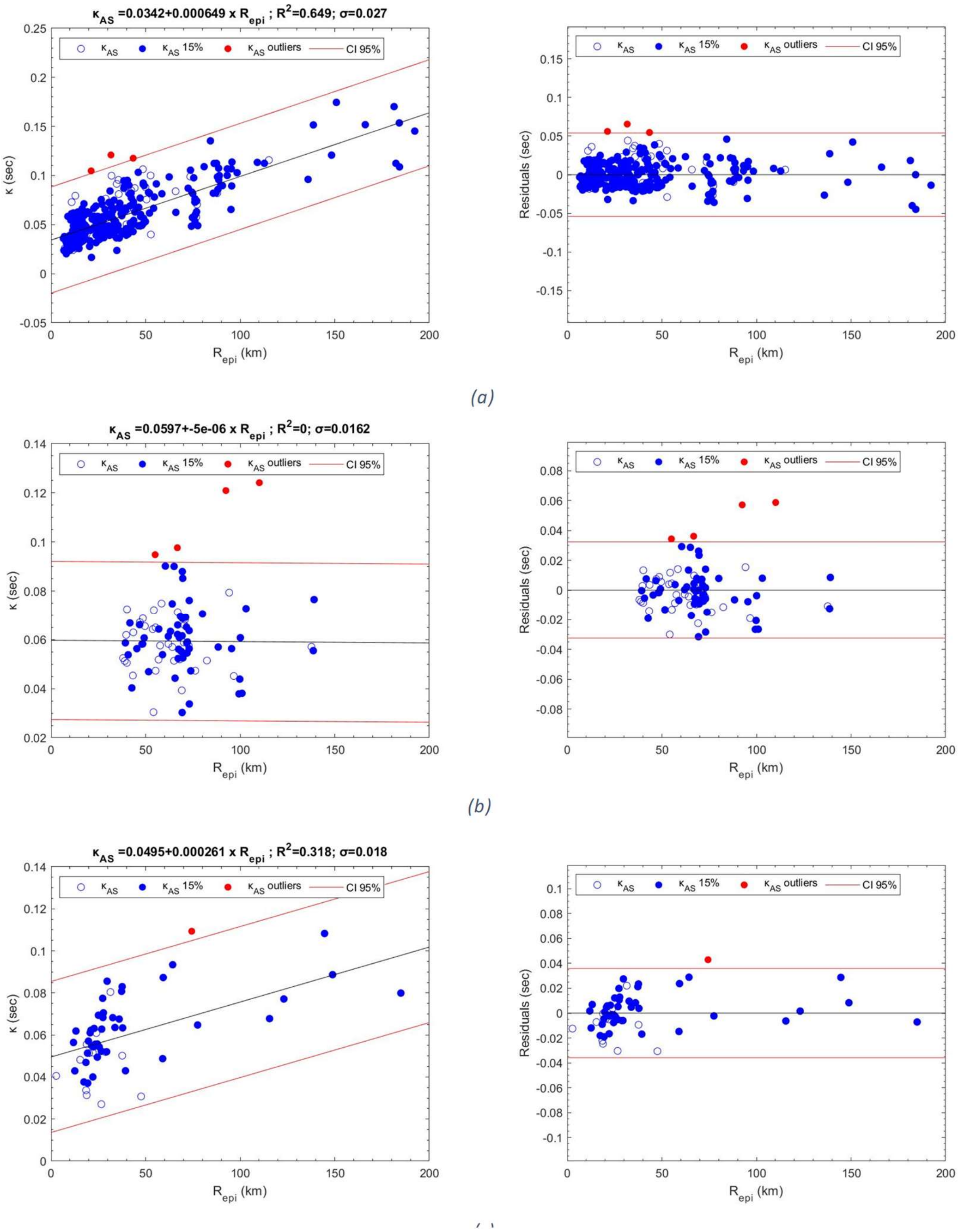

Figure 4.7. Kappa vs. Epicentral Distance scatter (on the left panel), Residual vs. Epicentral Distance scatter (on the right panel) for: (a) ST4404 (b) ST4406 (c) ST4802

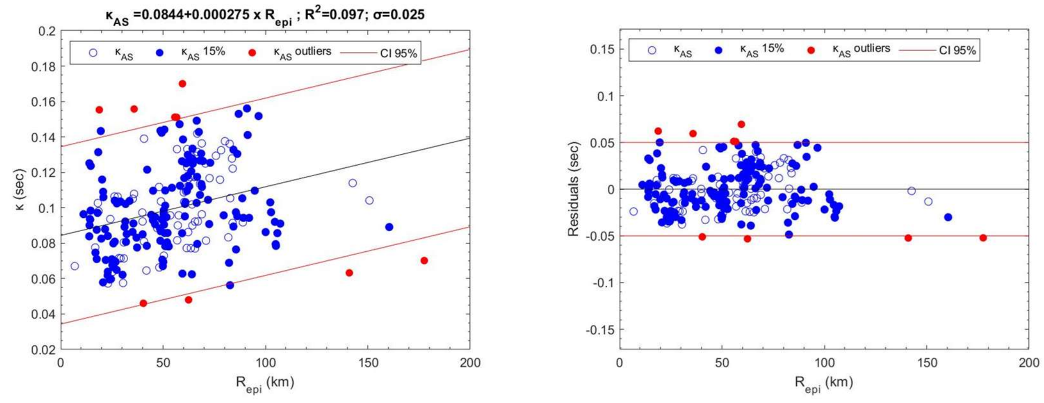

(a)

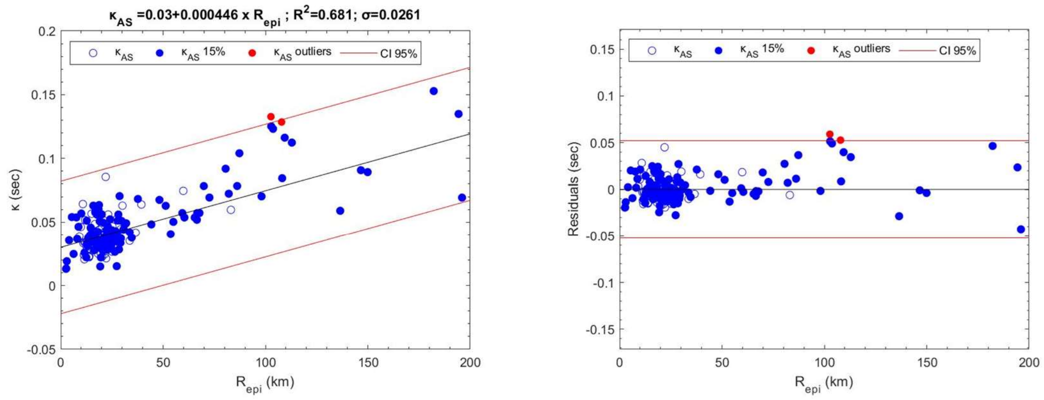

(b)

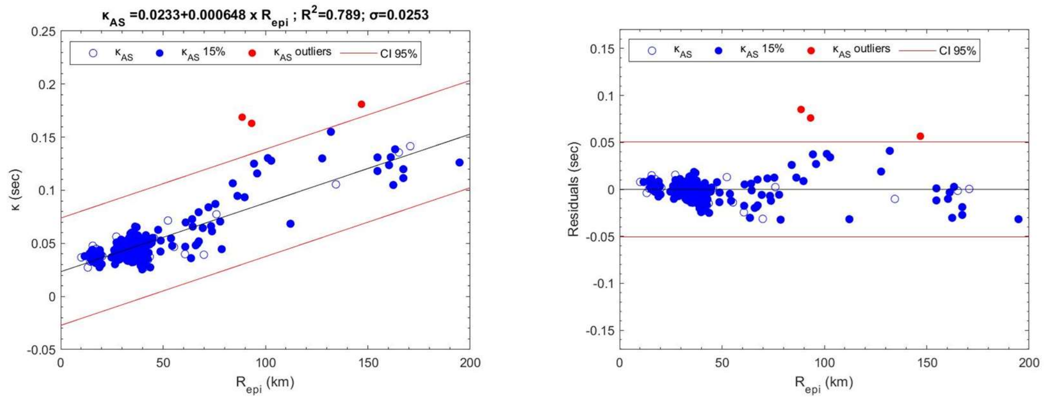

(c)

Figure 4.8. Kappa vs. Epicentral Distance scatter (on the left panel), Residual vs. Epicentral Distance scatter (on the right panel) for: (a) ST4808 (b) ST4809 (c) ST4817.

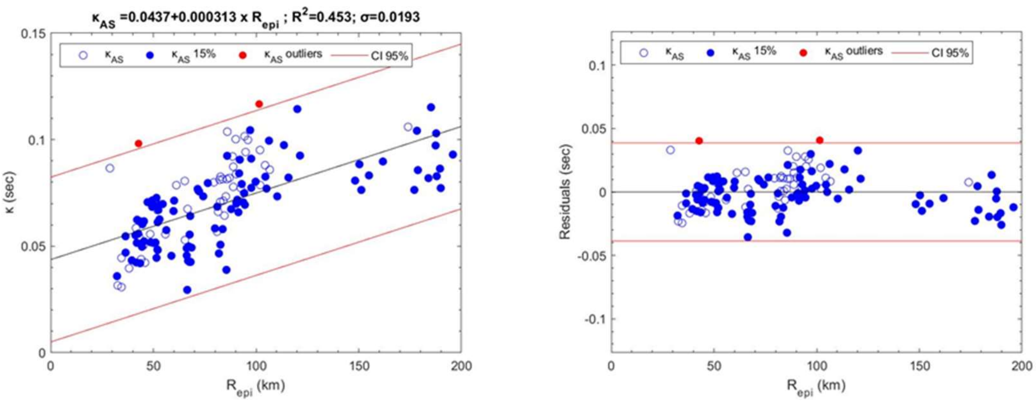

Figure 4.9. Kappa vs. Epicentral Distance scatter (on the left panel), Residual vs. Epicentral Distance scatter (on the right panel) for ST4818

Results of the regression are tabulated in Table 4.1 using the geographical groups defined in Chapter 3. The slope of the distribution with epicentral distance (κ_R) might be common, based on the assumption that the stations from the same group share the same overall frequency-independent regional Q value. Table 4.1 shows that this assumption is valid for the İzmir-Aydın group since the κ_R values for the seven stations are close to each other (κ_R=0.00031-0.00043) with a weighted average κ_R=0.00039. Please note that the goodness of the fit for each individual station is considered for calculating the weights. When three stations with quite small R^2 values (ST2302, ST4406 and ST2309) are ignored, the κ_R values for the stations in Elazıg-Malatya are found to be close to each other (κ_R=0.00048-0.00065) with the weighted average κ_R value of 0.00051. Using the same procedure, the weighted average κ_R value of the Bodrum-Muğla group is found to be 0.00046. Since there are only two stations each in Antalya and Biga groups, the weighted average of the κ_R values is not calculated for these groups. The weighted average of κ_R values are used to estimate the frequency-independent, effective quality factor Q_{eff} at high frequencies with the following equation (Ktenidou et al. 2015):

$$Q_{eff} = 1/\beta x \kappa_R \quad (4.1)$$

where the crustal shear wave velocity (β) is assumed as 3.2 km/s. Calculated regional Q values for three geographical groups from the weighted average of κ_r values are provided in Table 4.1.

Calculated Q values for İzmir-Aydın, Bodrum-Muğla, and Elazıg-Malatya groups are compared with the regional Q estimations from at high frequencies (10-25Hz) for similar regions in Table 4.1. Estimated Q values by from Eq. 4.1 is generally in good agreement with the Q values from previous studies for Erzincan, Western Anatolia, Southwestern Anatolia, and Northwestern Anatolia (Akinci et al., 1996; Akyol et al., 2015; Sahin et al., 2014; Akinci et al., 1994). It should be noted that these comparisons include several ambiguities: for example, the data range used in the attenuation studies mentioned above is different and the assumed crustal shear wave velocity has a significant effect on the results. However, estimated Q values for İzmir-Aydın, Bodrum-Muğla, and Elazıg-Malatya groups are in good agreement with the κ_R values given by Kishida et al. (2016) for California (Q=560-790). Differences for intra-region κ_R values can be explained by large regional differences due to the variability of the underlying Q structures and V_S profiles exhibited by similar sites.

Kishida et al. (2016) proposed a method for estimating the κ_0 value using the regional Q estimates with a "hockey-stick" dependence on distance. This approach is applied in this study to estimate the uncertainty of κ_0 value for each station, as shown in Figure 4.10. The κ_0 value for each station is re-estimated by least-squares linear regression with fixed slopes (fixed slopes set to minimum, mean, and maximum κ_R of the group), and the difference in κ_0 values are estimated from maximum, and minimum κ_R values are used as the error bars for κ_0 values (Table 4.1).

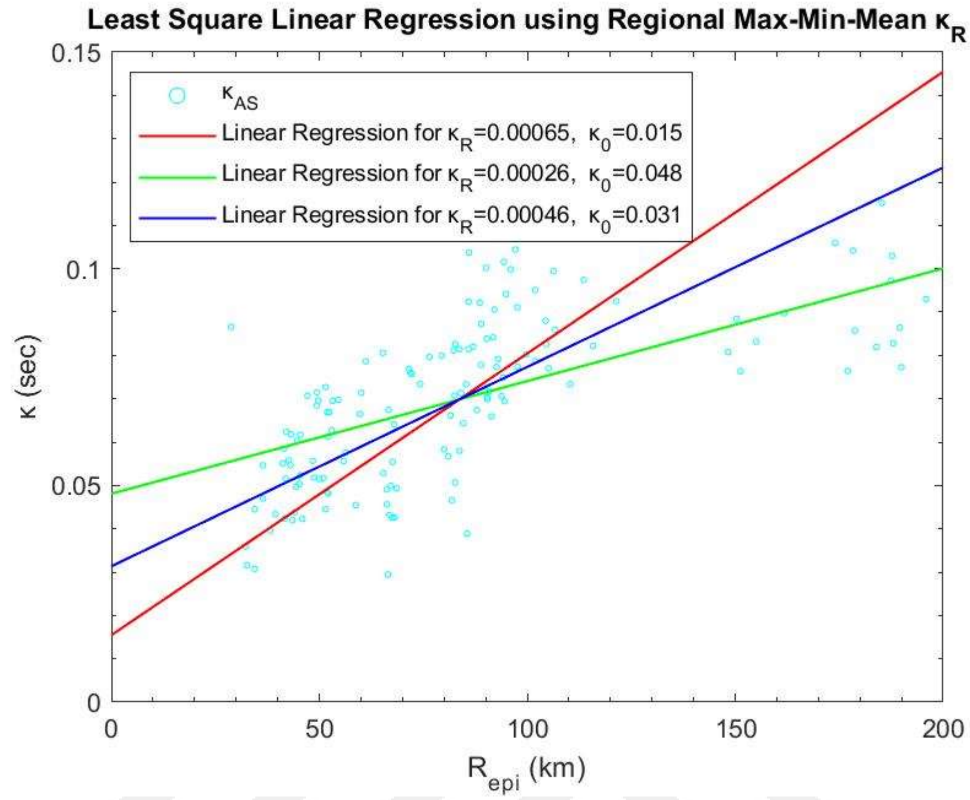

Figure 4.10. Least-squares regression lines with fixed slopes fitted to κ-R_{epi} distribution with minimum, mean, and maximum regional $κ_r$ values for the Bodrum-Muğla Group.

Table 4.1 Results obtained from the analysis, κ_0, κ_r, R^2, and used data

Group	Station ID	Vs30 (m/s)	Used Data (R_{epi}<200km)	κ_0 (s) (R_{epi}<200km)	κ_R (s/km) (R_{epi}<200km)	R^2 (R_{epi}<200km)	Weighted κ_R (s/km)	Estimated Q from κ_R (s/km)	Estimated Q from studies (10-25Hz, respectively)		Set Used	Estimated κ_0 (s)	error -	error +
Elazıg-Malatya Group	2302	907	156	**0.042**	0.00016	0.222	0.00051	616	310 - 798	Akinci et al. (1996) for Erzincan	Repi<200km	0.04163	0.0162	0.0162
	2305	907	149	**0.042**	0.00048	0.683						0.042	0.0115	0.0000
	2309	860	135	**0.045**	0.00013	0.044						0.045		
	2409	875	144	**0.011**	0.00054	0.593						0.011	0.0095	0.0056
	4404	1380	324	**0.034**	0.00065	0.649						0.034	0.0002	0.0068
	4406	815	89	**0.060**	0	0.001						0.060		
Mugla Group	4802	747	57	**0.050**	0.00026	0.318	0.00046	684	375-832	Akyol (2015) for Western Anatolia	Repi<100km	0.050	0.0145	0.0005
	4808	1323	223	**0.084**	0.00027	0.097						0.084		
	4809	747	231	**0.030**	0.00045	0.681						0.030	0.0070	0.0070
	4817	948	296	**0.023**	0.00065	0.789						0.023	0.0003	0.0167
	4818	1080	143	**0.044**	0.00031	0.453						0.044	0.0287	0.0043
İzmir-Aydın Group	919	986	296	**0.021**	0.00043	0.596	0.00039	802	375-832	Akyol (2015) for Western Anatolia	Repi<200km	0.021	0.0000	0.0100
	920	894	289	**0.029**	0.00043	0.625						0.029	0.0000	0.0100
	3506	771	143	**0.018**	0.00039	0.562						0.018	0.0033	0.0067
	3511	827	431	**0.030**	0.00039	0.552						0.030	0.0035	0.0055
	3514	836	143	**0.023**	0.00031	0.37						0.023	0.0104	0.0000
	3520	875	455	**0.032**	0.00039	0.499						0.032	0.0038	0.0062
	3536	1141	312	**0.034**	0.00035	0.509						0.034	0.0071	0.0019
Antalya Group	705	1113	83	**0.054**	0.00042	0.221	0.00059				Repi<100km	0.054	0.0389	0.0389
	707	1822	84	**0.091**	-2E-05	0.001						0.091		
Biga Group	1101	901	49	**0.034**	0.00026	0.606	0.00032				Repi<200km	0.034	0.0188	0.0188
	1708	1005	140	**0.010**	0.00037	0.685						0.010	0.0230	0.0230
		∑ =	**4372**											

Because a possible change in the slope of the linear correlation of kappa with R_{epi} is suggested by the residual plots of five stations, the regression analysis is repeated for the data with R_{epi}<100 km and R_{epi}<200 km, and the results are provided in Table 4.2. Figure 4.11 compares the κ_0 values estimated by changing the limit on the epicentral distance. According to Table 4.2 and Figure 4.10, κ_0 values obtained by using the data within R_{epi}<200km and R_{epi}<100km are not significantly different for most of the stations as expected, and the general trend in κ_0 vs. V_{S30} distribution does not change with this constrain. The κ_0 values obtained by using the data within R_{epi}<200km are 10% higher in average when compared to the κ_0 values obtained by using the data within R_{epi}<100km. The largest difference of κ_0 is observed in ST0920 and ST2409, consistent with the trends observed in residual plots for R_{epi}<50km. This large difference underlines the importance of the data at short distances on the stable κ_0 estimates. In three stations that showed bias at large distances (ST3514, ST4817, and ST4818), the difference in κ_0 values is also notable. The goodness of the fit (represented by the R^2) is reduced in the majority of the stations when the data within R_{epi}<100km is used, even if the number of data points is decreased by only 16.8% with this distance constraint. Alternative linear fits applied to the kappa-R_{epi} distributions for all stations are provided in Appendix B.

A good agreement in κ_R values of the stations in the Bodrum-Muğla group is observed when the distance-constrain is applied. For the data within R_{epi}<100km, κ_R values for the stations in Bodrum-Muğla are found to be close to each other (κ_R=0.00051-0.00064) and higher than the weighted average (κ_R=0.00046) calculated for this group. The azimuthal distribution of the events recorded by these stations (Figures 3.5-3.12) showed that the majority of the events within R_{epi}<100km have similar azimuths (and probably similar and repeatable path contributions) while the events with 100km<R_{epi}<200km are quite scattered in terms of azimuth. A similar phenomenon was observed by Kishida et al. (2016) for data within R_{epi}<50km for Arizona. Unfortunately, other stations do not display unbalanced azimuthal distributions; thus are not suitable for interpretation in terms of repeatable path effects.

Table 4.2 The kappa parameters estimated obtained by R_{epi}<200km and R_{epi}<100km datasets.

			R_{epi}<200km				R_{epi}<100km					
Group	Station ID	Vs30 (m/s)	Used Data	κ_0 (s)	κ_R (s/km)	R^2	Used Data	κ_0 (s)	κ_R (s/km)	R^2	κ0 difference between datasets (%)	R^2 difference between datasets (%)
Elazıg-Malatya Group	2302	907	156	**0.042**	0.00016	0.222	139	**0.032**	0.00036	0.236	23.16%	6.31%
	2305	907	149	**0.042**	0.00048	0.683	135	**0.037**	0.00058	0.741	12.61%	8.49%
	2309	860	135	**0.045**	0.00013	0.044	129	**0.039**	0.00024	0.038	12.82%	
	2409	875	144	**0.011**	0.00054	0.593	87	**0.022**	0.00031	0.235	-88.56%	-60.37%
	4404	1380	324	**0.034**	0.00065	0.649	311	**0.033**	0.00068	0.51	3.09%	-21.42%
	4406	815	89	**0.06**	0	0.001	82	**0.063**	-5E-05	0.005	-6.31%	
Mugla Group	4802	747	57	**0.05**	0.00026	0.318	51	**0.04**	0.00064	0.349	18.78%	9.75%
	4808	1323	223	**0.084**	0.00027	0.097	210	**0.084**	0.00051	0.206	0.71%	
	4809	747	231	**0.03**	0.00045	0.681	210	**0.028**	0.00051	0.385	7.97%	-43.47%
	4817	948	296	**0.023**	0.00065	0.789	278	**0.024**	0.00062	0.514	-4.14%	-34.85%
	4818	1080	143	**0.044**	0.00031	0.453	**113**	**0.025**	0.00059	0.515	42.01%	13.69%
İzmir-Aydın Group	919	986	296	**0.021**	0.00043	0.596	246	**0.015**	0.0005	0.363	28.20%	-39.09%
	920	894	289	**0.029**	0.00043	0.625	235	**0.007**	0.00076	0.472	75.96%	-24.48%
	3506	771	143	**0.018**	0.00039	0.562	118	**0.015**	0.00044	0.298	15.72%	-46.98%
	3511	827	431	**0.03**	0.00039	0.552	312	**0.025**	0.00043	0.582	16.82%	5.43%
	3514	836	143	**0.023**	0.00031	0.37	127	**0.007**	0.00053	0.297	69.05%	-19.73%
	3520	875	455	**0.032**	0.00039	0.499	406	**0.032**	0.00037	0.268	-1.81%	-46.29%
	3536	1141	312	**0.034**	0.00035	0.509	251	**0.039**	0.00023	0.151	-15.37%	-70.33%
Antalya Group	705	1113	83	**0.054**	0.00042	0.221	51	**0.041**	0.00063	0.32	24.93%	44.80%
	707	1822	84	**0.091**	-2E-05	0.001	23	**0.074**	0.00025	0.035	18.82%	
Biga Group	1101	901	49	**0.034**	0.00026	0.606	27	**0.034**	0.00024	0.439	0.93%	-27.56%
	1708	1005	140	**0.01**	0.00037	0.685	94	**0.012**	0.00032	0.304	-25.88%	-55.62%
		∑ =	**4372**				**3635**			Avg.=	**10.43%**	-22.32%

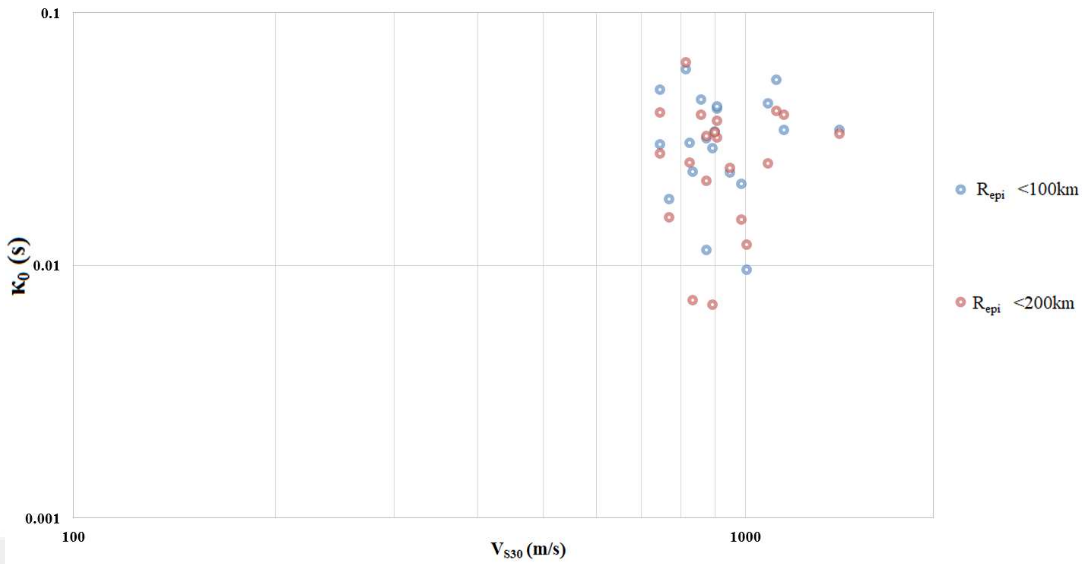

Figure 4.11. Comparison of the κ_0 values obtained from data within R_{epi}<200km and R_{epi}<100km and the general trends in the κ_0-V_{S30} distribution based on distance constraint.

In Figures 4.12 and 4.13, the magnitude dependence of the record-specific kappa values is evaluated for each station. Similar to previous studies before (Castro et al. 2015, Stanko et al. 2018), magnitude dependency of kappa is observed for all stations with a low correlation coefficient (R^2<0.4), indicating an increase in kappa within the available magnitude range.

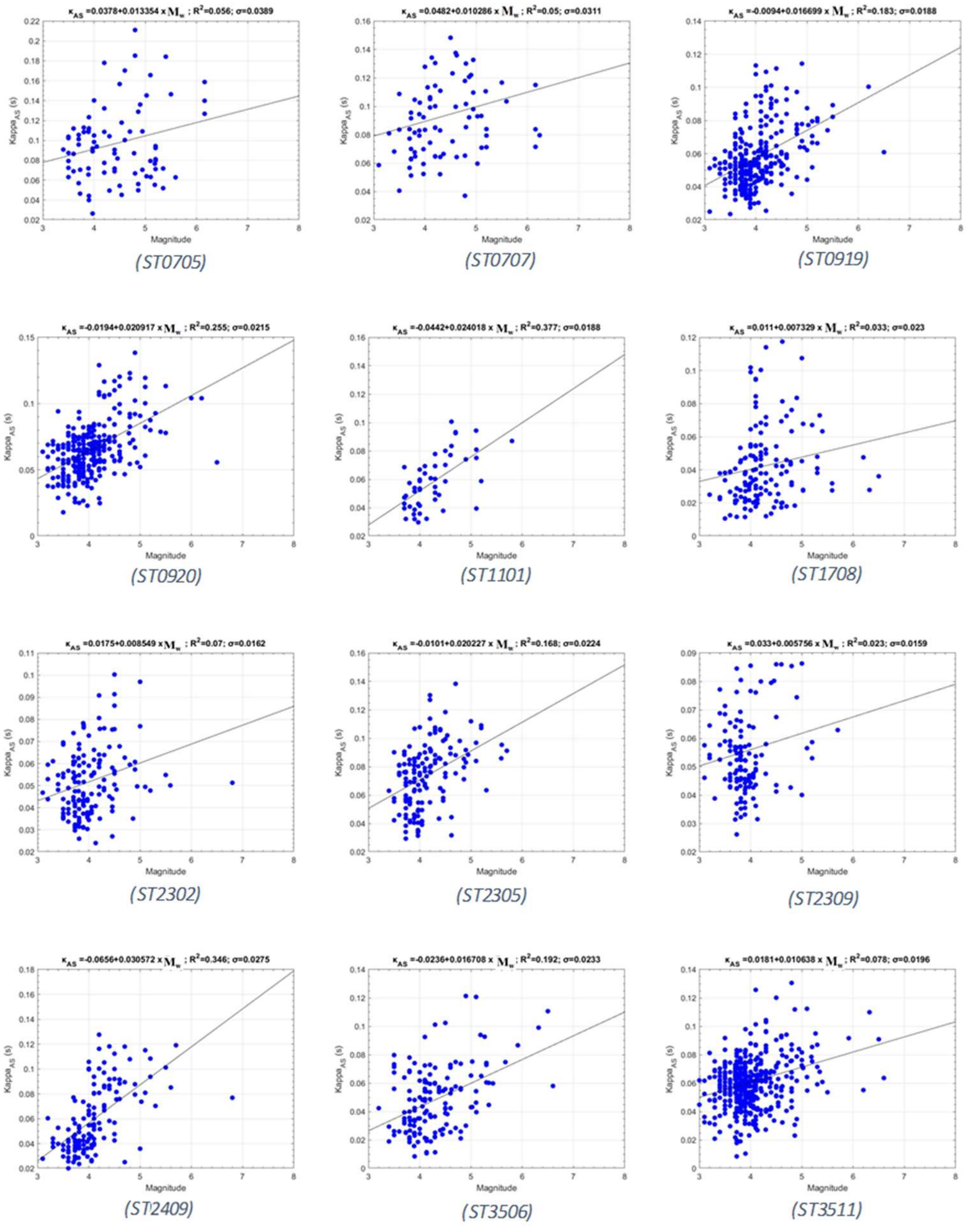

Figure 4.12. Correlation of record specific kappa values with magnitude at different stations.

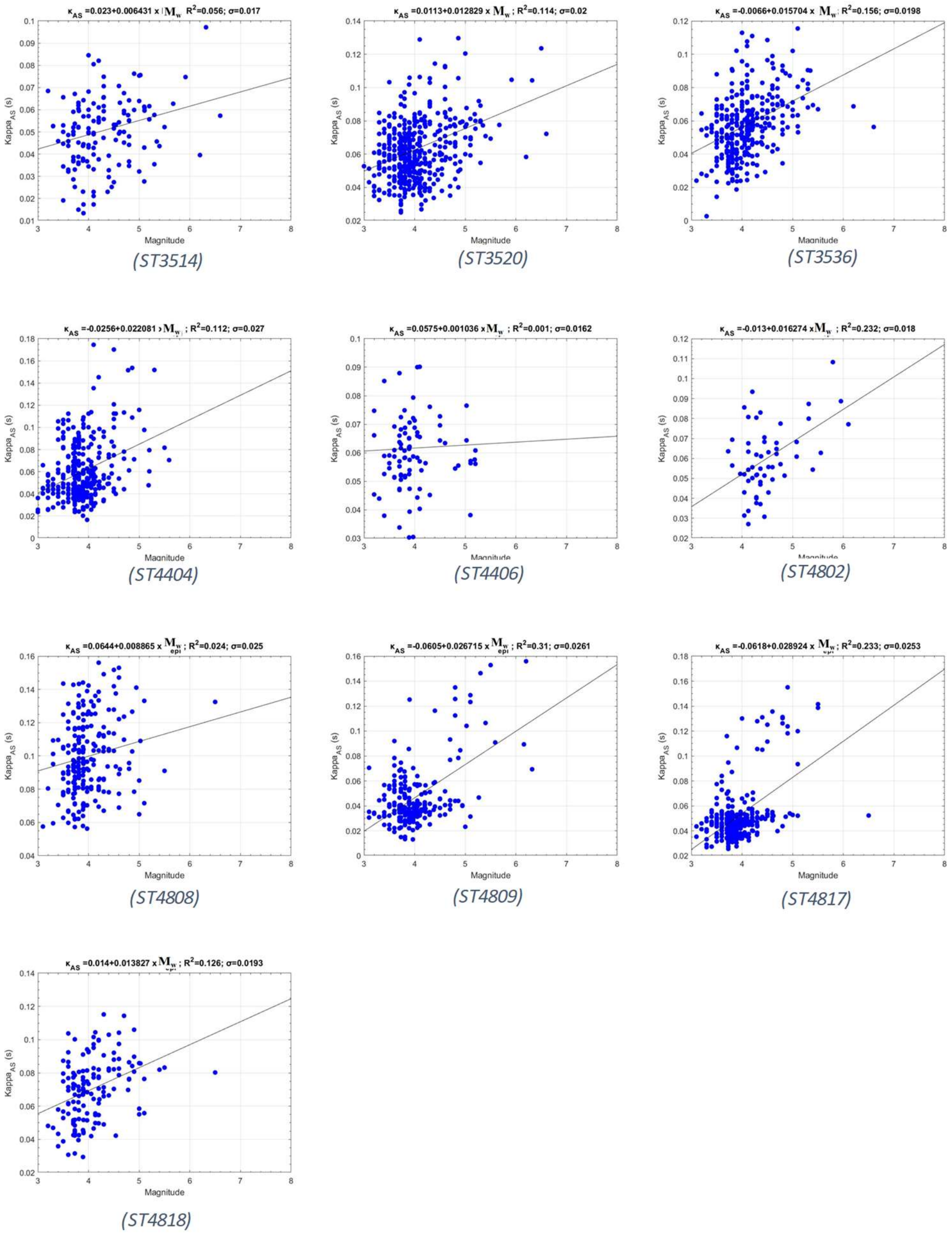

Figure 4.13. Correlation of record specific kappa values with magnitude at different stations (continued).

Figure 4.14 presents the distribution of zero-distance kappa values for each station with V_{S30}. Four out of 22 stations (ST0707, ST2309, ST4406, and ST4808) are not included in this plot because a stable estimate of κ_0 was not retrieved from these stations. The V_{S30} values for the remaining (and more reliable) stations vary between 747-1380m/s. However, it is expected that the κ_0 value decreases as the site stiffness increases (Ktenidou et al. 2014), a very clear trend in κ_0 with V_{S30} is not detected in Figure 4.14. Ktenidou et al. (2015) claimed that the decrease in κ_0 is mostly applicable for Site Classes B and C (Eurocode 8), and there is hardly a decrease observed beyond V_{S30}=550m/s where κ_0 stabilizes above V_{S30}=1600m/s. In Figure 4.14, a rather large scatter in κ_0 for the same V_{S30} values is observed. Previous studies explained this large scatter with the insufficiency of V_{S30} parameter: V_{S30} represents only a part of the V_S profile that contributes to the local site amplification, while κ_0 is controlled by the first few kilometers of the profile (Campbell, 2009). Also, the depth to the bedrock correlates with κ_0 to a similar degree as V_{S30} (Ktenidou et al., 2012). Additionally, the uncertainty in V_{S30} values resulting from different geophysical measurement techniques goes up to 30-50%, as Moss (2008) and Boore (2006) explained. In a large percentage of the Vs profiles of the stations (Figures 3.13-3.14), unusual Vs reversals are observed, especially at the surficial soil layers, which may have a significant effect on the κ_0 estimates.

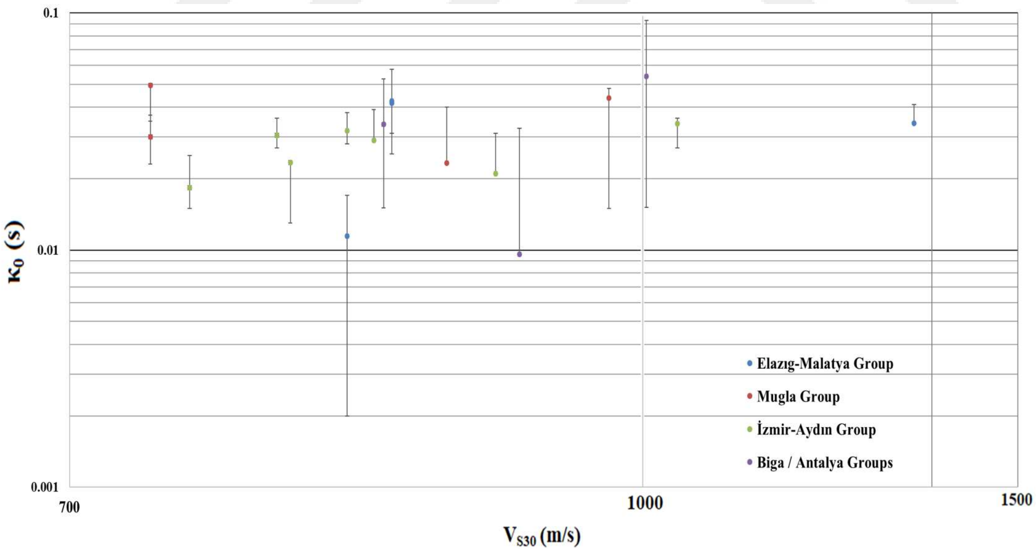

Figure 4.14. κ_0 vs. V_{S30} distribution (log-log) and error bars for Elazıg-Malatya, Mugla, and İzmir-Aydın groups

CHAPTER 5

SUMMARY AND CONCLUSIONS

In this study, the record-specific and station-specific high-frequency attenuation parameters are estimated for more than five thousand two-component strong-motion recordings from 22 seismological stations in Turkey. The findings of this study significantly contribute to the current literature because each station represents the "hard-rock conditions" with measured V_{S30} values being higher than 740m/s and are well-recorded stations that include a minimum of 100 recordings from M_W>3 events. Recording stations may be divided into five geographical groups based on their locations, and each group has unique characteristics. The group with the largest number of stations, the İzmir-Aydın Group, contains 2746 recordings, including the recordings from October 30^{th,} 2020, Samos Earthquake and its aftershocks. The dataset for the Elazığ-Malatya Group is dominated by the events occurring on the East Anatolian Fault, while the dataset of Biga Group mostly consists of events from the North Anatolian Fault. The majority of the events recorded by the stations in the Bodrum-Muğla Group were occurred in the Aegean Sea, including deeper events that were later excluded from the dataset.

A total of 6463 two-component recordings were examined manually, and 1270 of them were excluded because they contain signals from multiple events or have a signal-to-noise ratio lower than 3. The remaining recordings were processed with the Seismic Analysis Code (SAC) to obtain the time for P and S wave arrivals, and the FAS for the S-wave window was calculated and transferred to the Mathlab routine. Record-specific kappa values were estimated from the acceleration FAS of each record for a carefully-selected and record-specific frequency band using the AH84 method. Throughout this process, cases where the record-specific kappa depends on a narrow frequency band (f_2-f_1<7Hz), recordings with kappa from at least one component is negative, and the recordings that have a difference in kappa from two-horizontal components more than 25% were eliminated. In this respect, applied methodology is consistent with the state-of-the-art followed in the global engineering practice for calculating the high-frequency attenuation parameter.

The least-square linear regression method was utilized on record specific kappa – R_{epi} distribution in order to obtain the zero-distance kappa value for each station. Analysis results showed that stable estimates of κ_0 are not retrieved from four stations, even if these stations include more than 500 recordings in total. The general increasing trend in record-specific kappa was captured in 4 of the remaining 18 stations, but the goodness of the fit is quite low (R^2<0.35). For 14 stations, statistically stable κ_0 values were estimated. To capture the variability of the estimates, the weighted average values for the slopes of the linear kappa – R_{epi} relation were calculated for each geographical group, and the error bars for κ_0 values were determined. A possible correlation between the record-specific kappa and magnitude was evaluated for each station. Even if the scatter was considerably high, an increase in kappa with magnitude was observed.

Figure 5.1 and 5.2 compares the κ_0 values estimated in this study with the previous global values that were calculated by the AH84 method and the limited number of κ_0 values that were estimated using the data recorded in Turkey. Scatter observed in the distribution of κ_0 with V_{S30} is obvious, and the possible underlining reasons for this scatter elaborated in Chapter 4. It should be underlined here that the stability of the κ_0-V_{S30} correlation depends on the accuracy of the measured V_S profiles. The accuracy of the V_S profiles of these stations was questionable as the results from MASW/RE-MI differ significantly, and the several V_S reversals in the first few meters observed in almost every station were hard to explain. On the other hand, estimated κ_0 values in this study have a reasonably good agreement with the rest of κ_0 estimations worldwide, and the number of κ_0 estimates for very stiff sites (V_{S30}>1000 m/s) increased significantly with the added data points. Therefore, the results presented in this study are significant for extending the knowledge on the attenuation of near-surface layers in Turkey and provides valuable information on the local source parameters to be used in the host-to-target adjustment of GMPEs.

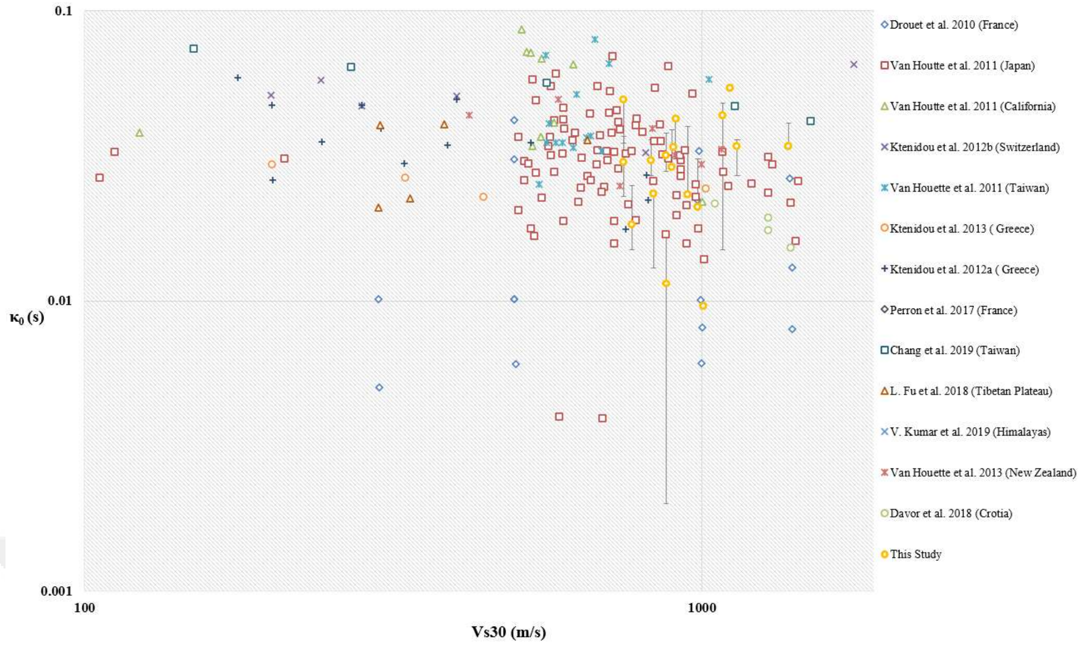

Figure 5.1. Comparison of results from other studies using Anderson and Hough (1984) method

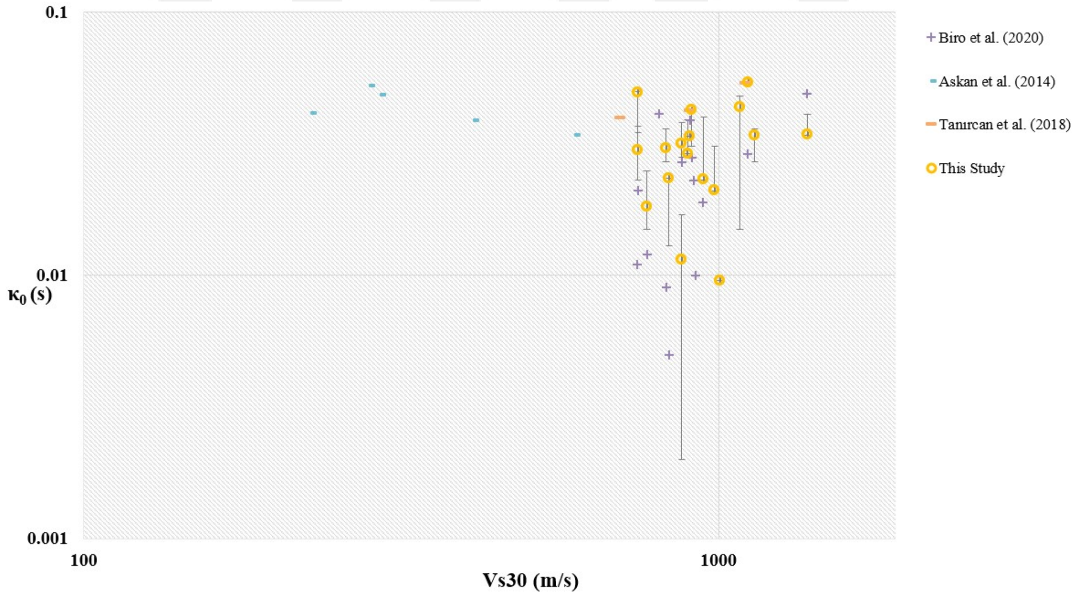

Figure 5.2. Comparison of results with other studies in Turkey

REFERENCES

Anderson, J.G., Hough, S.E., 1984. A model for the shape of the Fourier amplitude spectrum of acceleration at high frequencies. Bulletin of the Seismological Society of America 74, 1969–1993.

Biro, Y., and P. Renault. 2012. Importance and impact of host-to-target conversions for ground-motion prediction equations in PSHA, in 15th World Conference on Earthquake Engineering, Lisbon, Portugal, 24–28 September 2012.

Douglas, J., Gehl, P., Bonilla, L.F., Ǵlis, C., 2010. A κ model for mainland France. Pure and Applied Geophysics 167, 1303–1315. doi:10.1007/s00024-010-0146-5

Fernández, A. I., Castro, R. R., & Huerta, C. I. (2010). The spectral decay parameter kappa in Northeastern Sonora, Mexico. Bulletin of the Seismological Society of America, 100(1), 196–206. https://doi.org/10.1785/0120090049

Zafarani, H., Hassani, B., & Ansari, A. (2012). Estimation of earthquake parameters in the Alborz seismic zone, Iran using the generalized inversion method. Soil Dynamics and Earthquake Engineering, 42, 197–218. https://doi.org/10.1016/j.soildyn.2012.05.019

Ktenidou, O. J., Gélis, C., & Bonilla, L. F. (2013). A study on the variability of kappa (κ) in a Borehole: Implications of the computation process. Bulletin of the Seismological Society of America, 103(2 A), 1048–1068. https://doi.org/10.1785/0120120093

Ktenidou, O. J., Van Houtte, C., Cotton, F., & Abrahamson, N. A. (2013). Kappa0 (κ0) estimates for hard rock SED stations in Switzerland using a high-frequency approach. AGU Fall Meeting Abstracts. Retrieved from https://www.mendeley.com/catalogue/8c547123-bf06-3664-81fc-6d50116cdcb4/

Van Houtte, C., Ktenidou, O. J., Larkin, T., & Holden, C. (2014). Hard-site κ0 (kappa) calculations for Christchurch, New Zealand, and comparison with local ground-motion prediction models. Bulletin of the Seismological Society of America, 104(4), 1899–1913. https://doi.org/10.1785/0120130271

Castro, R. R., & Ávila-Barrientos, L. (2015). Estimation of the spectral parameter kappa in the region of the Gulf of California, Mexico. Journal of Seismology, 19(4), 809–829. https://doi.org/10.1007/s10950-015-9496-x

Pavel, F., & Vacareanu, R. (2015). Kappa and regional attenuation for Vrancea (Romania) earthquakes. Journal of Seismology, 19(3), 791–799. https://doi.org/10.1007/s10950-015-9490-3

Neighbors, C., Liao, E. J., Cochran, E. S., Funning, G. J., Chung, A. I., Lawrence, J. F., … Andrés Sepulveda, H. H. (2015). Investigation of the high-frequency attenuation parameter, κ (kappa), from aftershocks of the 2010 Mw 8.8 Maule, Chile earthquake. Geophysical Journal International, 200(1), 200–215. https://doi.org/10.1093/gji/ggu390

Edwards, B., Ktenidou, O. J., Cotton, F., Abrahamson, N., Van Houtte, C., & Fäh, D. (2015). Epistemic uncertainty and limitations of the κ<inf>0</inf> model for near-surface attenuation at hard rock sites. Geophysical Journal International, 202(3), 1627–1645. https://doi.org/10.1093/gji/ggv222

Ktenidou, O. J., Abrahamson, N. A., Drouet, S., & Cotton, F. (2015). Understanding the physics of kappa (κ): Insights from a downhole array. Geophysical Journal International, 203(1), 678–691. https://doi.org/10.1093/gji/ggv315

Fu, L., Li, X., Fang, W., & Chen, S. (2019). A study of site response and regional attenuation in the Longmen Shan region, eastern Tibetan Plateau, SW China, from seismic recordings using the generalized inversion method. Journal of Asian Earth Sciences, 181(December 2018), 103887. https://doi.org/10.1016/j.jseaes.2019.103887

Alibazi, A., & Saffari, H. (2019). Spectral Decay Parameter (k) of Western Iran Using Accelerograms Recorded up to 2018. Pure and Applied Geophysics, 176(11), 4847–4860. https://doi.org/10.1007/s00024-019-02238-9

Ji, C., Cabas, A., Cotton, F., Pilz, M., & Bindi, D. (2020). Within-station variability in Kappa: Evidence of directionality effects. Bulletin of the Seismological Society of America, 110(3), 1247–1259. https://doi.org/10.1785/0120190253

Tsurugi, M., Tanaka, R., Kagawa, T., & Irikura, K. (2020). High-frequency spectral decay characteristics of seismic records of inland crustal earthquakes in japan: Evaluation of the fmax and κ models. Bulletin of the Seismological Society of America, 110(2), 452–470. https://doi.org/10.1785/0120180342

Kumar, V., Chopra, S., Choudhury, P., & Kumar, D. (2020). Estimation of near-surface attenuation parameter kappa (κ) in Northwest and Northeast Himalaya region. Soil Dynamics and Earthquake Engineering, 136(September 2019), 106237. https://doi.org/10.1016/j.soildyn.2020.106237

Davor, S., & Mario, G. (n.d.). Estimation of high-frequency attenuation parameter kappa (κ) in the Central and Southern Dalmatia (Croatia) Region. 1–28.

Pavlenko, O. V. (2020). Regional characteristics of radiation and propagation of seismic waves in the North-Eastern Caucasus. Russian Journal of Earth Sciences, 20(5), 1–16. https://doi.org/10.2205/2020ES000705

Ktenidou O.-J., S. Drouet, N. Theodulidis, M. Chaljub, S. Arnaouti, & F. Cotton. (2012). Estimation of kappa (κ) for a sedimentary basin in Greece (EUROSEISTEST) - Correlation to site characterization parameters. 15th World Conference of Earthquake Engineering, 24-28 Sep. Retrieved from http://peer.berkeley.edu/~aschell/15WCEE/pdf/WCEE2012_4079.pdf

Campbell, K. W., Hashash, Y., Kim, B., Kottke, A. R., Rathje, E. M., Silva, W. J., … Earthquake, P. (2014). Reference-Rock Site Conditions for Central and Eastern North America : Part II – Attenuation (Kappa) Definition. Peer Report 2014-12, (August 2014).

Chang, S. C., Wen, K. L., Huang, M. W., Kuo, C. H., Lin, C. M., Chen, C. Te, & Huang, J. Y. (2019). The High-Frequency Decay Parameter (Kappa) in Taiwan. Pure and Applied Geophysics, 176(11), 4861–4879. https://doi.org/10.1007/s00024-019-02219-y

Kishida, T., Kayen, R. E., Ktenidou, O.-J., Silva, W. J., Darragh, R. B., & Watson-Lamprey, J. (2014). PEER Arizona strong-motion database and GMPEs evaluation. (June 2014), 170.

Kumar, S., Kumar, D., Rastogi, B. K., & Singh, A. P. (2018). Kappa (K) model for the Kachchi region of western India. Geomatics, Natural Hazards, and Risk, 9(1), 442–455. https://doi.org/10.1080/19475705.2018.1447025

Kilb, D., Biasi, G., Anderson, J., Brune, J., Peng, Z., & Vernon, F. L. (2012). A comparison of spectral parameter kappa from small and moderate earthquakes using southern California ANZA seismic network data. Bulletin of the Seismological Society of America, 102(1), 284–300. https://doi.org/10.1785/0120100309

van Houtte, C., Drouet, S., & Cotton, F. (2011). Analysis of the origins of κ (kappa) to compute hard rock to rock adjustment factors for GMPEs. Bulletin of the Seismological Society of America, 101(6), 2926–2941. https://doi.org/10.1785/0120100345

Kurtulmuş, T. Ö., & Akyol, N. (2015). Separation of source, site, and near-surface attenuation effects in western Turkey. Natural Hazards, 77(3), 1515–1532. https://doi.org/10.1007/s11069-015-1660-7

Drouet, S., Cotton, F., & Guéguen, P. (2010). VS30, κ, regional attenuation and Mw from accelerograms: Application to magnitude 3-5 French earthquakes. Geophysical Journal International, 182(2), 880–898. https://doi.org/10.1111/j.1365-246X.2010.04626.x

Askan, A., Sisman, F. N., & Pekcan, O. (2014). A regional near-surface high-frequency spectral attenuation (kappa) model for northwestern Turkey. Soil

Dynamics and Earthquake Engineering, 65, 113–125. https://doi.org/10.1016/j.soildyn.2014.06.007

Tanırcan, G., & Dikmen, S. Ü. (2018). Variation of high-frequency spectral attenuation (Kappa) in vertical arrays. Soil Dynamics and Earthquake Engineering, 113, 406–414. https://doi.org/10.1016/j.soildyn.2018.06.016

Perron, V., Hollender, F., Bard, P. Y., Gélis, C., Guyonnet-Benaize, C., Hernandez, B., & Ktenidou, O. J. (2017). Robustness of kappa (κ) measurement in low-to-moderate seismicity areas: Insight from a site-specific study in Provence, France. Bulletin of the Seismological Society of America, 107(5), 2272–2292. https://doi.org/10.1785/0120160374

Dikmen, S. U., Pinar, A., & Edincliler, A. (2016). Near-surface attenuation using traffic-induced seismic noise at a downhole array. Journal of Seismology, 20(1), 375–384. https://doi.org/10.1007/s10950-015-9533-9

Ktenidou, O.-J., Abrahamson, N. A., Darragh, R. B., & Silva, W. J. (2016). A Methodology for the Estimation of Kappa from Large Datasets : Example Application to Rock Sites in the NGA-East Database and Implications on Design Motions. PEER Report No. 2016/01, (April 2016).

Biro, Y., Siyahi, B., & Akbas, B. (2020). The Spectral Decay Parameter K (Kappa) For Hard Rock Strong Ground Motıon Statıons In Turkey.

Ktenidou, O., Cotton, F., Abrahamson, N. A., & Anderson, J. G. (2017). Erratum to Taxonomy of κ : A Review of Definitions and Estimation Approaches Targeted to Applications. Seismological Research Letters, 88(3), 875–876. https://doi.org/10.1785/0220170058

Mittal, H., Sharma, B., Chao, W. an, Wu, Y. M., Lin, T. L., & Chingtham, P. (2020). A Comprehensive Analysis of Attenuation Characteristics Using Strong Ground Motion Records for the Central Seismic Gap Himalayan Region, India. Journal of Earthquake Engineering, 00(00), 1–26. https://doi.org/10.1080/13632469.2020.1768969

Palmer, S. M., & Atkinson, G. M. (2020). The high-frequency decay slope of spectra (Kappa) for M ≥ 3:5 earthquakes on rock sites in eastern and western Canada. Bulletin of the Seismological Society of America, 110(2), 471–488. https://doi.org/10.1785/0120190206

Hanks, T.C., 1982. Fmax. Bulletin of the Seismological Society of America 72, 1867–1879.

Hanks, T.C., McGuire, R.K., 1981. The character of high-frequency strong ground motion. Bulletin of the Seismological Society of America 71, 2071–2095.

Boore, D., 2003. Simulation of ground motion using the stochastic method. Pure and Applied Geophysics 160, 635–676. doi:10.1007/PL00012553 Boore, DM, 1983. Stochastic simulation of high-frequency ground motions based on seismological

models of the radiated spectra. Bulletin of the Seismological Society of America 73, 1865–1894. Brune, J.N., 1970. Tectonic stress and the spectra of seismic shear waves from earthquakes. Journal of Geophysical Research 75, 4997–5009. doi:10.1029/JB075i026p04997

Castro, R. R., L. Trojani, G. Monachesi, M. Mucciarelli, and M. Cattaneo (2000). The spectral decay parameter κ in the region of Umbria-Marche, Italy. J. Geophys. Res. 105(B10), 23811–23823, doi:10.1029/2000JB900236. Campbell, K.W. et al., 2014. Reference-Rock Site Conditions for Central and Eastern North America: Part II - Attenuation (Kappa) Definition. Peer Report 2014/11, (August 2014).

Irmak, T. S., Yavuz, E., Livaoğlu, H., Şentürk, E., & Sahin, E. Y. (2020). Source parameters for small-moderate earthquakes in Marmara Region (Turkey). Geosciences Journal, 24(5), 541–555. https://doi.org/10.1007/s12303-019-0039-2

Chandler, a. M., Lam, N.T.K., Tsang, H.H., Sheikh, M.N., 2005. Estimation of near-surface attenuation in bedrock for analysis of intraplate seismic hazard. Journal of Seismology and Earthquake Engineering 7, 159–173. Cormier, V.F., 1982. The Effect of Attenuation on Seismic Body Waves. Bulletin of the Seismological Society of America 72, 169–200.

Tsurugi, M., Tanaka, R., Kagawa, T., & Irikura, K. (2020). High-frequency spectral decay characteristics of seismic records of inland crustal earthquakes in japan: Evaluation of the fmax and κ models. Bulletin of the Seismological Society of America, 110(2), 452–470. https://doi.org/10.1785/0120180342

Actions and Material Strength Requirements, Earthquakes. (n.d.). The Overseas Coastal Area Development Institute of Japan. Retrieved January 16, 2021, from http://ocdi.or.jp/tec_st/tec_pdf/tech_235_270.pdf

Trifunac, M. D. (1994). Fourier amplitude spectra of strong-motion acceleration: Extension to high and low frequencies. Earthquake Engineering & Structural Dynamics, 23(4), 389–411. https://doi.org/10.1002/eqe.4290230404

Irmak, T. S., Yavuz, E., Livaoğlu, H., Şentürk, E., & Sahin, E. Y. (2020). Source parameters for small-moderate earthquakes in Marmara Region (Turkey). Geosciences Journal, 24(5), 541–555. https://doi.org/10.1007/s12303-019-0039-2

Irmak, T. S., Yavuz, E., Livaoğlu, H., Şentürk, E., & Sahin, E. Y. (2020). Source parameters for small-moderate earthquakes in Marmara Region (Turkey). Geosciences Journal, 24(5), 541–555. https://doi.org/10.1007/s12303-019-0039-2

Gündüz, H., Ayşe, K. Ö., Boztepe Güney, A., & Niyazi, T. (1998). S-wave attenuation in the Marmara region, northwestern Turkey. Geophysical Research Letters, 25(14), 2733–2736. https://doi.org/10.1029/98GL02042

KALKAR, B., & GÖK, E. (2020). İzmir ve Çevresinde Kaydedilen Deprem Dalgalarının Frekans Bağımlı Soğurulması. Türk Deprem Araştırma Dergisi, 2(1), 92–100. https://doi.org/10.46464/tdad.737107

Akyol, N. (2015). Lapse time dependence of coda wave attenuation in Central West Turkey. Tectonophysics, 659, 53–62. https://doi.org/10.1016/j.tecto.2015.07.027

Sertcelik, F., & Guleroglu, M. (2017). Coda Wave Attenuation Characteristics for North Anatolian Fault Zone, Turkey. Open Geosciences, 9(1), 480–490. https://doi.org/10.1515/geo-2017-0037

Tanırcan, G., Miyake, H., Yamanaka, H., & Özel, O. (2020). Large Stress Release During Normal-Faulting Earthquakes in Western Turkey Supported by Broadband Ground Motion Simulations. Pure and Applied Geophysics, 177(5), 1969–1981. https://doi.org/10.1007/s00024-019-02357-3

Irmak, T. S., Yavuz, E., Livaoğlu, H., Şentürk, E., & Sahin, E. Y. (2020). Source parameters for small-moderate earthquakes in Marmara Region (Turkey). Geosciences Journal, 24(5), 541–555. https://doi.org/10.1007/s12303-019-0039-2

Şahin, Ş., & Çinar, M. (2014). Frequency-Dependent Attenuation of Coda Waves in the Crust in Southwest Anatolia (Turkey). Pure and Applied Geophysics, 171(7), 1203–1217. https://doi.org/10.1007/s00024-013-0690-x

Akinci, A., Taktak, A. G., & Ergintav, S. (1994). Attenuation of coda waves in Western Anatolia. Physics of the Earth and Planetary Interiors, 87(1–2), 155–165. https://doi.org/10.1016/0031-9201(94)90028-0

Akinci, A., & Eyidoğan, H. (1996). Frequency-dependent attenuation of S and coda waves in Erzincan region (Turkey). Physics of the Earth and Planetary Interiors, 97(1–4), 109–119. https://doi.org/10.1016/0031-9201(96)03155-X

APPENDICES

A. Frequency Distribution with Magnitude and Epicentral Distance

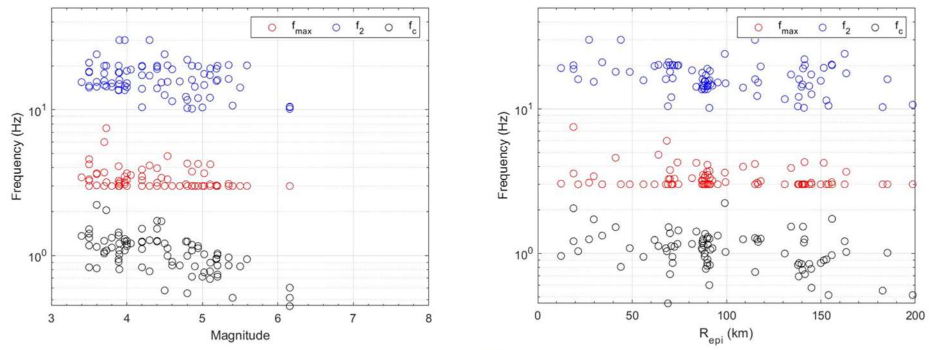

(a)

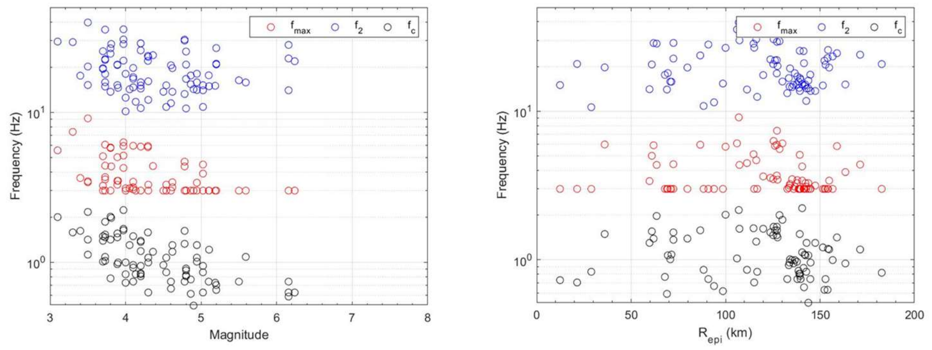

(b)

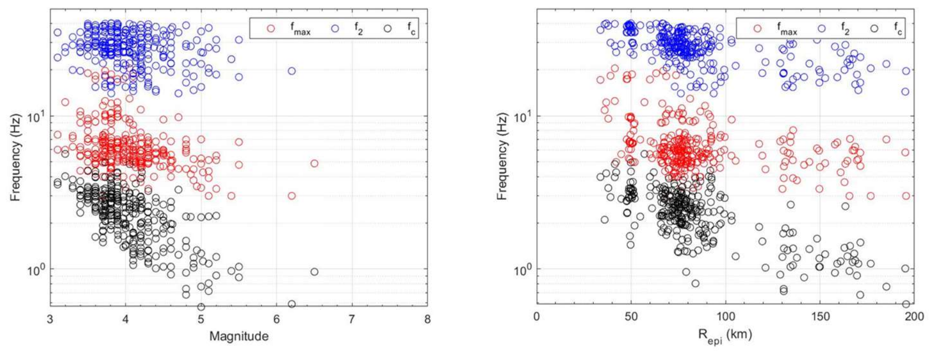

(c)

Figure A.1. f_c, f_{max}, and f_2 vs. magnitude distribution (on the left panel), f_c, f_{max}, and f_2 vs. epicentral distance distribution (on the right panel) for: (a) ST0705, (b) ST0707, (c) ST0919.

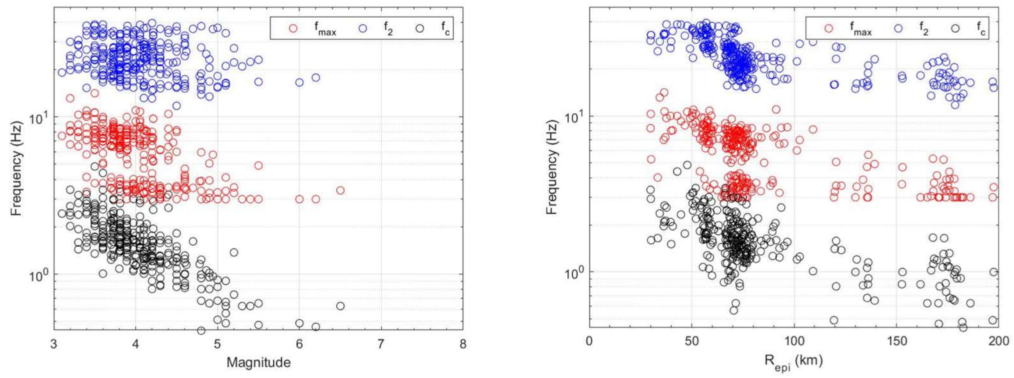

(a)

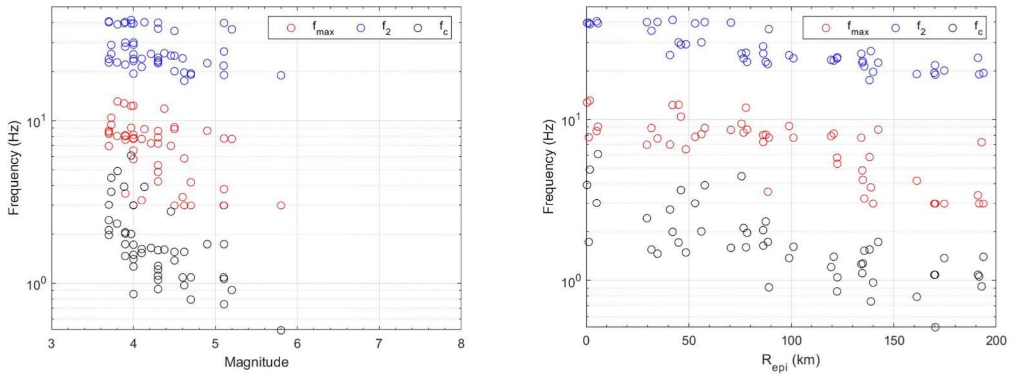

(b)

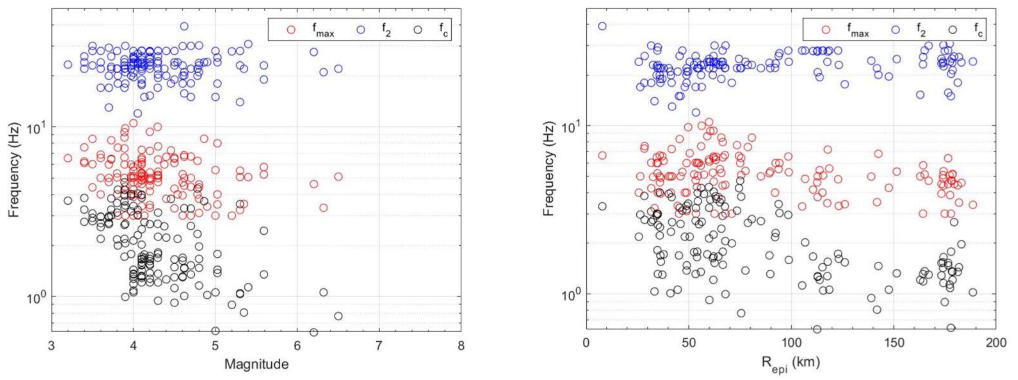

(c)

Figure A.2. f_c, f_{max}, and f_2 vs. magnitude distribution (on the left panel), f_c, f_{max}, and f_2 vs. epicentral distance distribution (on the right panel) for: (a) ST0920, (b) ST1101, (c) ST1708.

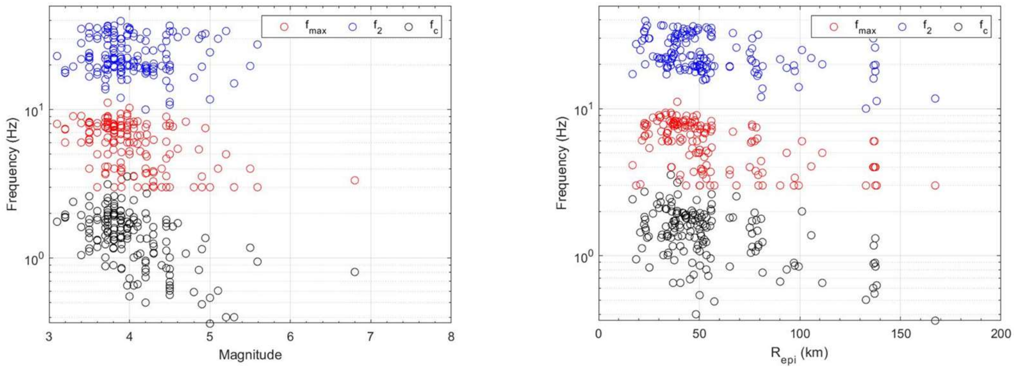

(a)

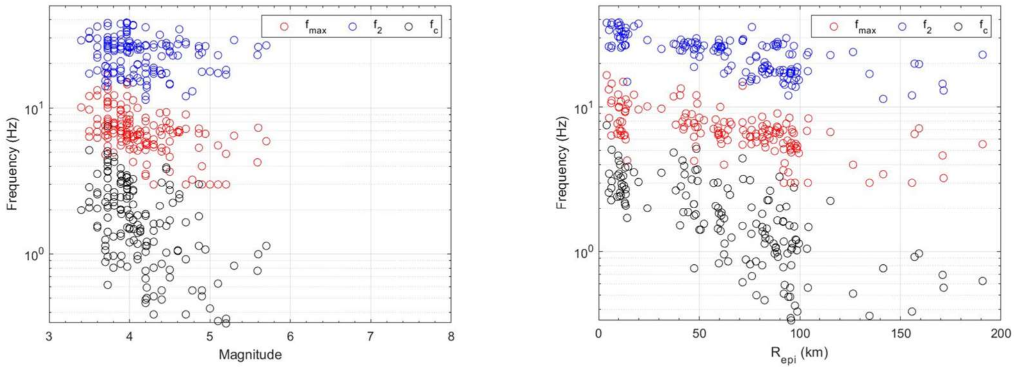

(b)

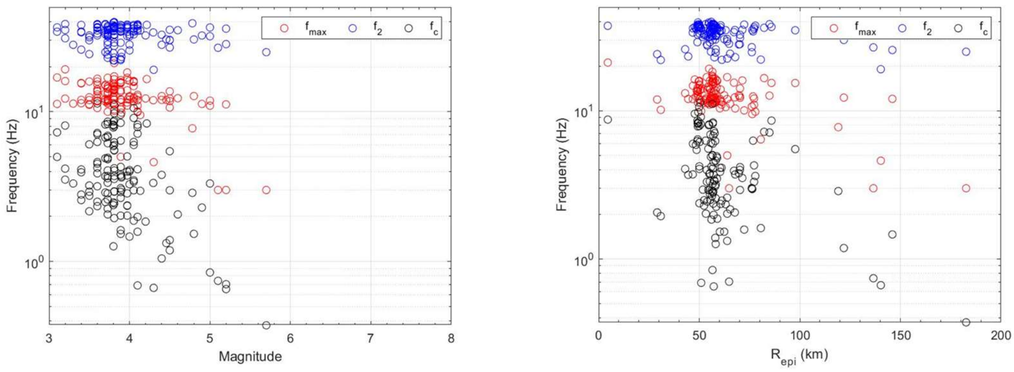

(c)

Figure A.3. f_c, f_{max}, and f_2 vs. magnitude distribution (on the left panel), f_c, f_{max}, and f_2 vs. epicentral distance distribution (on the right panel) for: (a) ST2302, (b) ST2305, (c) ST2309.

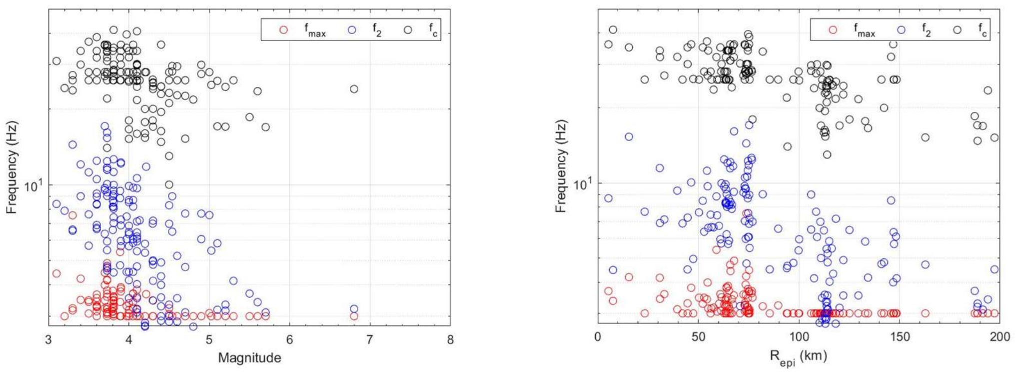

(a)

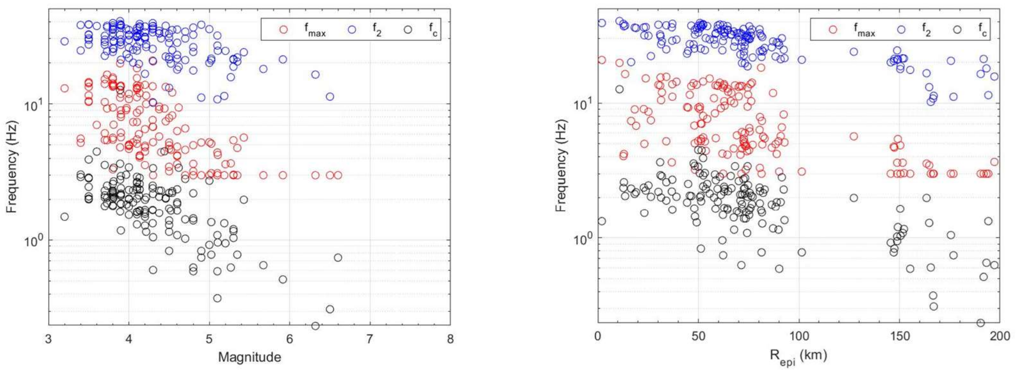

(b)

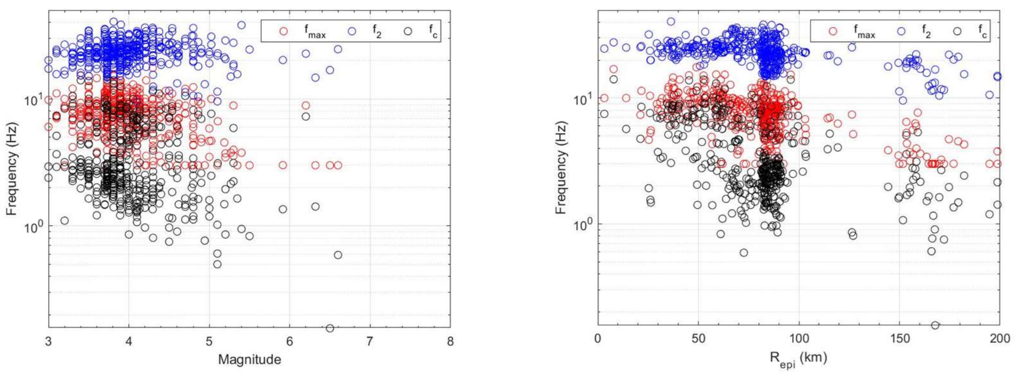

(c)

Figure A.4. f_c, f_{max}, and f_2 vs. magnitude distribution (on the left panel), f_c, f_{max}, and f_2 vs. epicentral distance distribution (on the right panel) for: (a) ST2409, (b) ST3506, (c) ST3511.

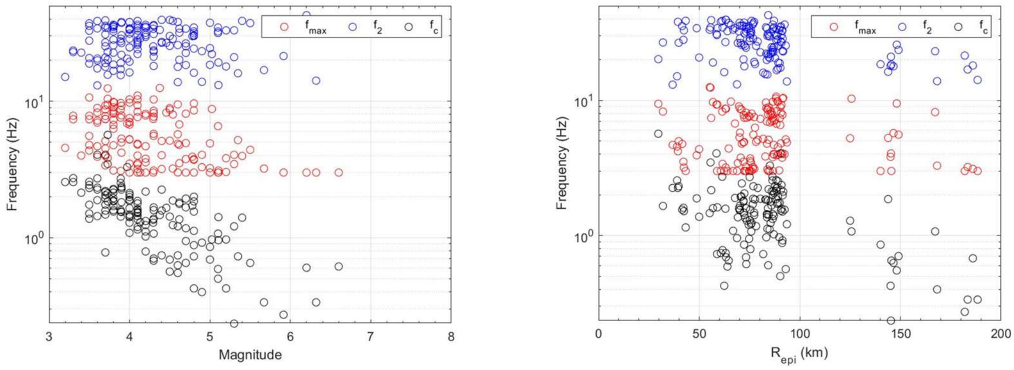

(a)

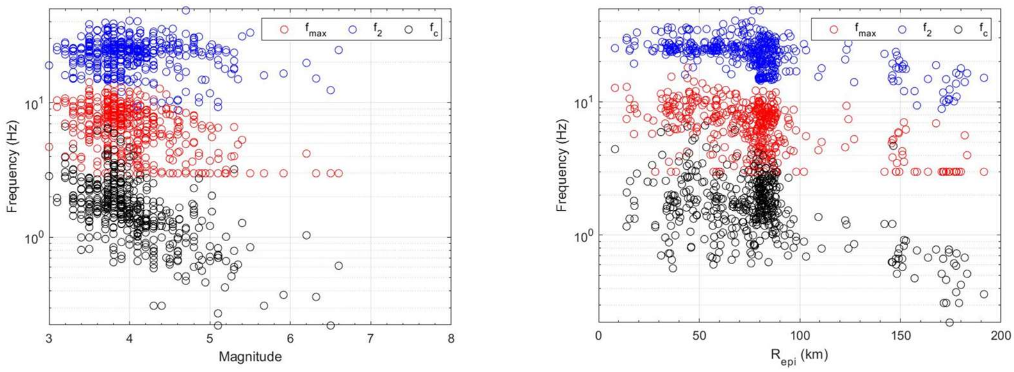

(b)

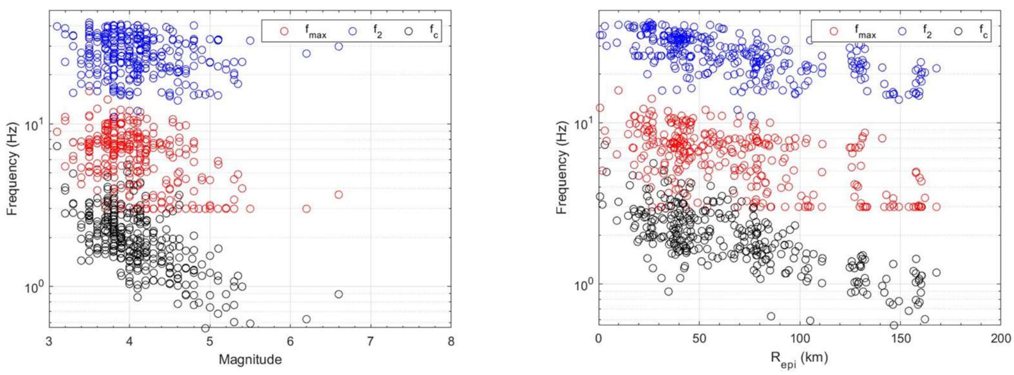

(c)

Figure A.5. f_c, f_{max}, and f_2 vs. magnitude distribution (on the left panel), f_c, f_{max}, and f_2 vs. epicentral distance distribution (on the right panel) for: (a) ST3514, (b) ST3520, (c) ST3536.

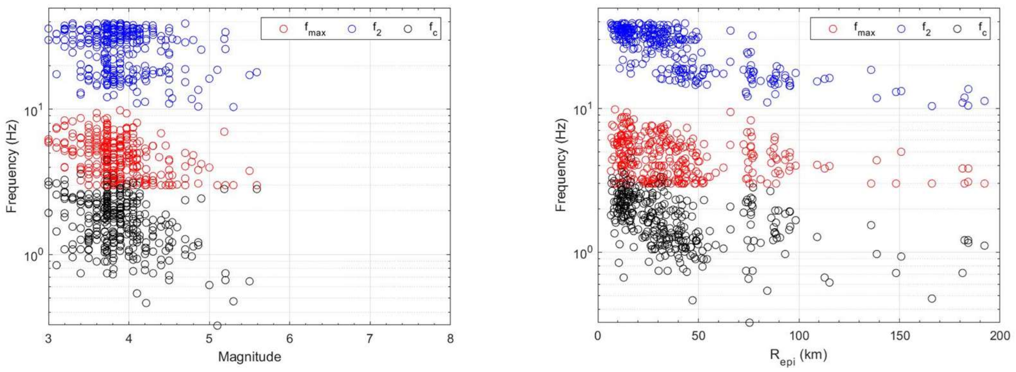

(a)

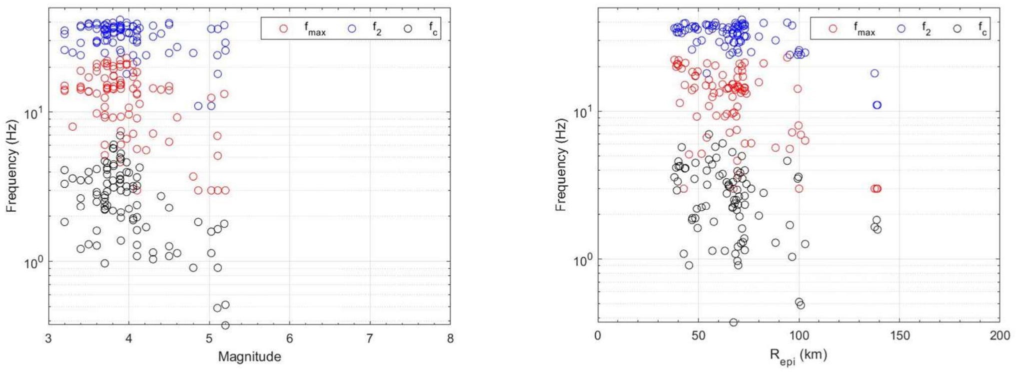

(b)

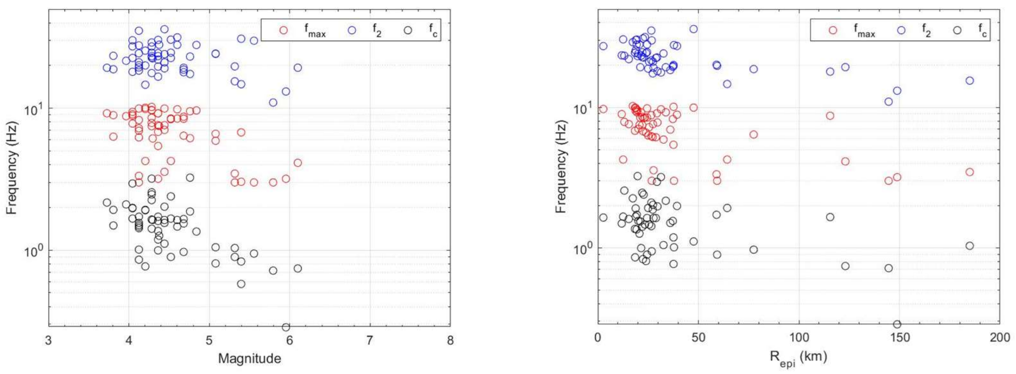

(c)

Figure A.6. f_c, f_{max}, and f_2 vs. magnitude distribution (on the left panel), f_c, f_{max}, and f_2 vs. epicentral distance distribution (on the right panel) for: (a) ST4404, (b) ST4406, (c) ST4802.

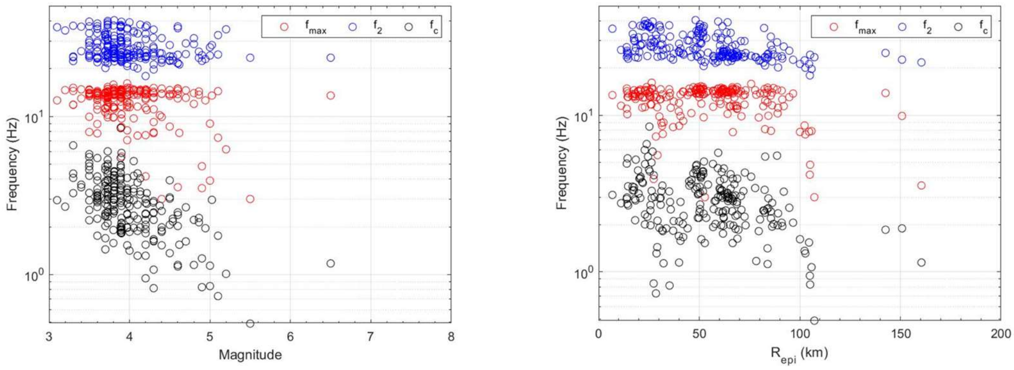

(a)

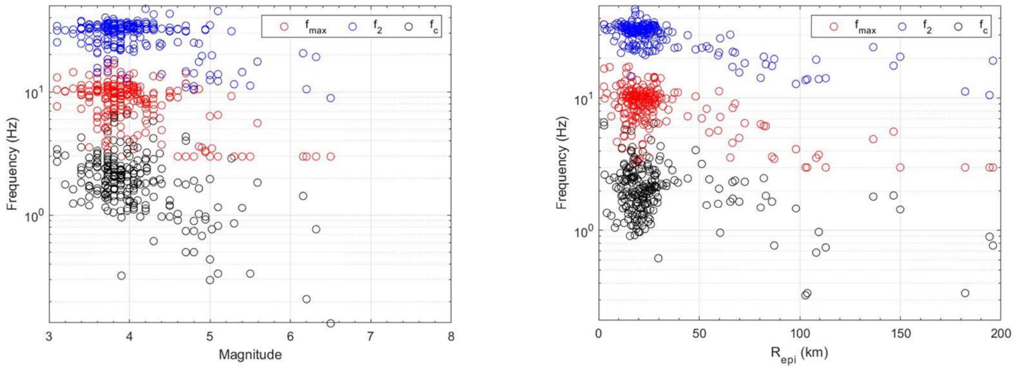

(b)

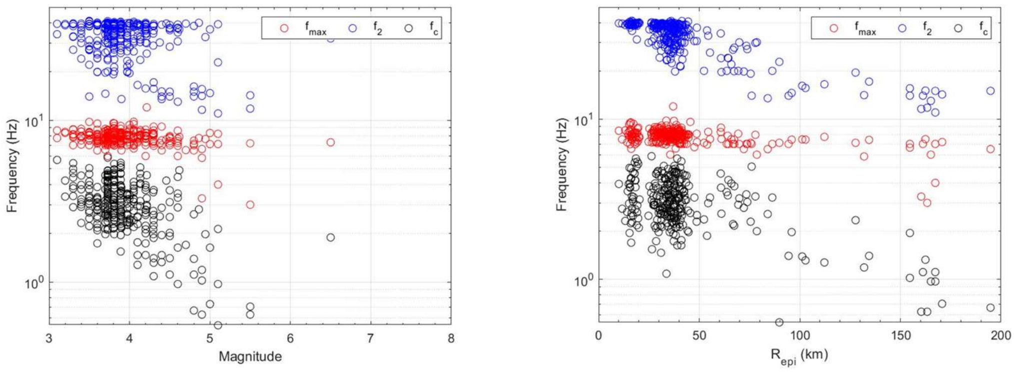

(c)

Figure A.7. f_c, f_{max}, and f_2 vs. magnitude distribution (on the left panel), f_c, f_{max}, and f_2 vs. epicentral distance distribution (on the right panel) for: (a) ST4808, (b) ST4809, (c) ST4817.

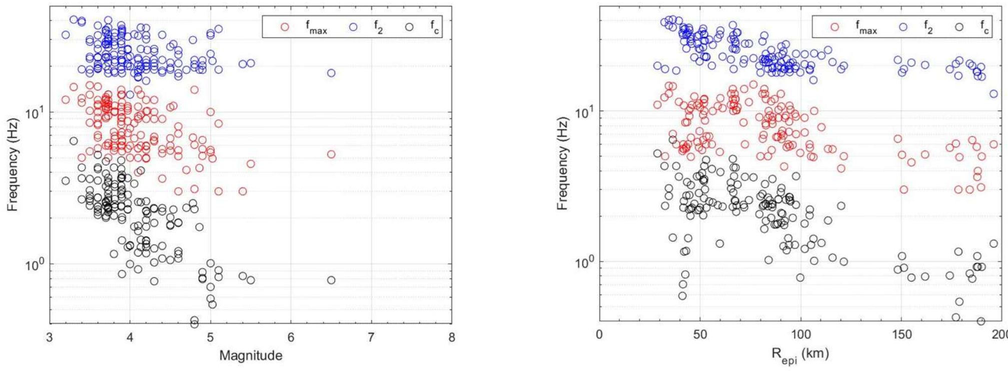

Figure A.8. f_c, f_{max}, and f_2 vs. magnitude distribution (on the left panel), f_c, f_{max}, and f_2 vs. epicentral distance distribution (on the right panel) for ST4818

B. Zero-Distance Kappa Error Estimation with Least Squares Linear Regression on Fixed Slopes

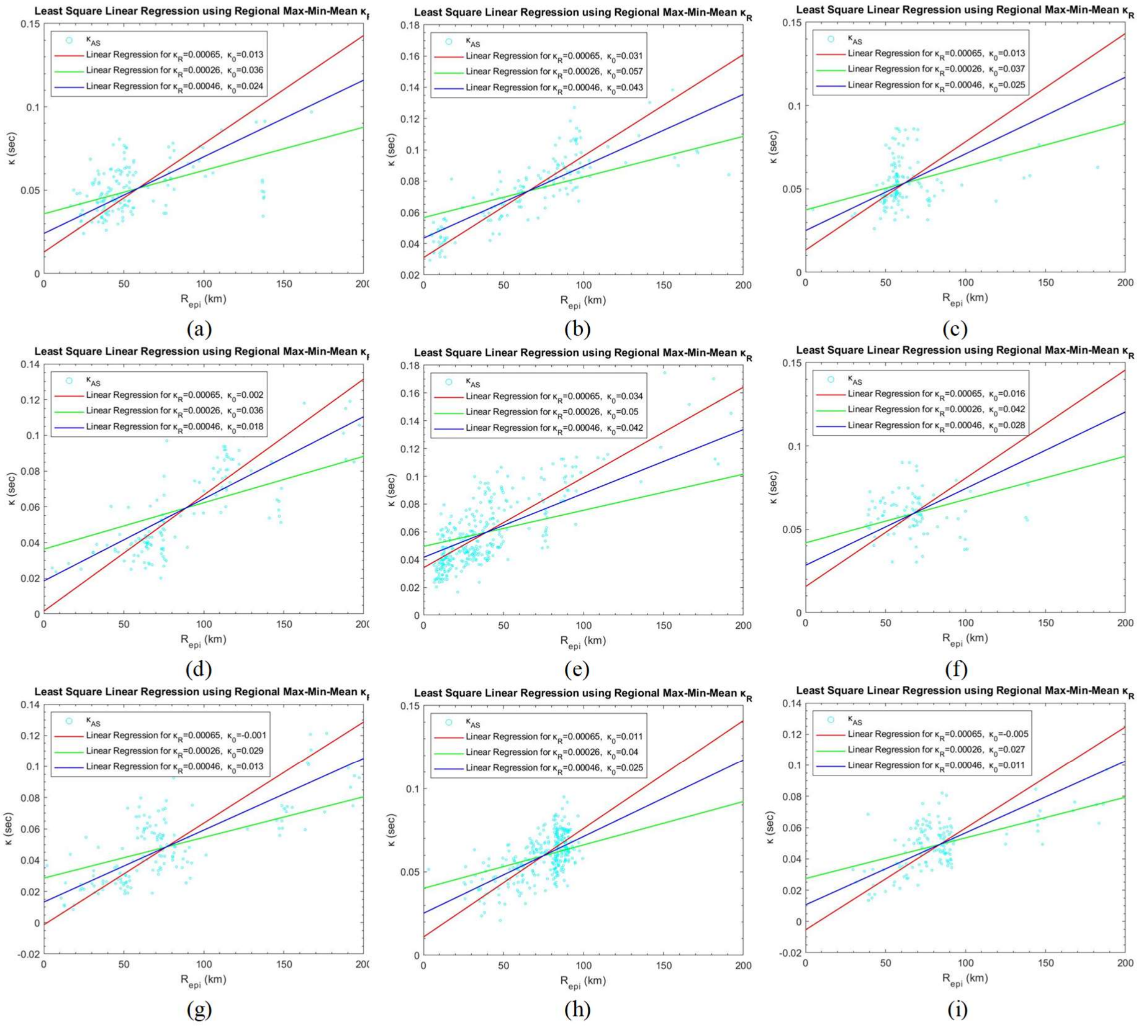

Figure B.1. Zero-distance kappa error estimation with least squares linear regression on fixed slopes (minimum, mean, and maximum κ_R) for: (a) ST2302 (b) ST2305 (c) ST2309 (d) ST2409 (e) ST4404 (f) ST4406 (g) ST3506 (h) ST3511 (i) ST3514

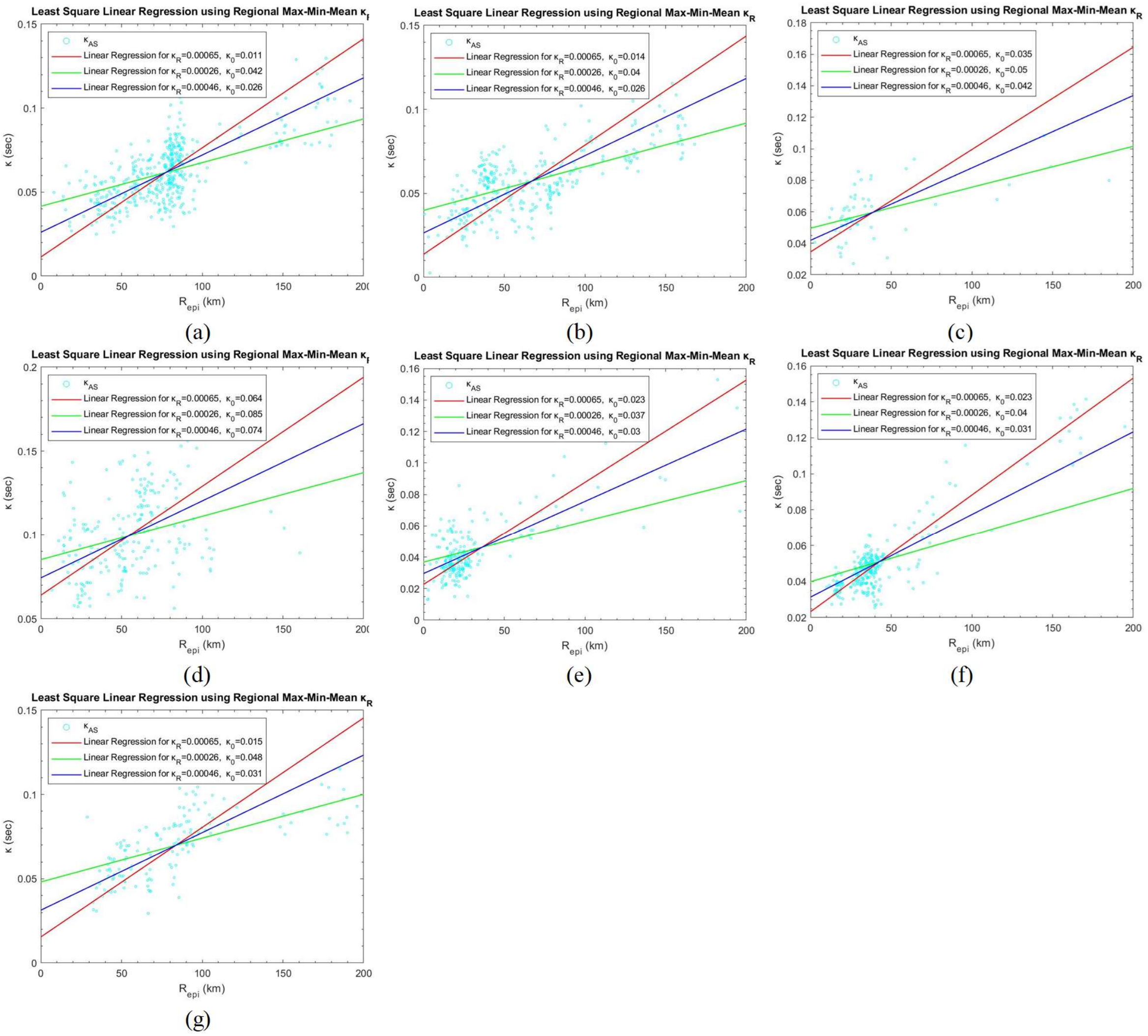

Figure B.2. Zero-distance kappa error estimation with least squares linear regression on fixed slopes (minimum, mean, and maximum κ_R) for: (a) ST3520 (b) ST3536 (c) ST4802 (d) ST4808 (e) ST4809 (f) ST4817 (g) ST4818